DIRECT AND INDIRECT SEARCHES FOR NEW PHYSICS AT THE ELECTROWEAK SCALE

by

Xinyu Miao

A Dissertation Submitted to the Faculty of the

DEPARTMENT OF PHYSICS

In Partial Fulfillment of the Requirements
For the Degree of

DOCTOR OF PHILOSOPHY

In the Graduate College

THE UNIVERSITY OF ARIZONA

2011

THE UNIVERSITY OF ARIZONA
GRADUATE COLLEGE

As members of the Dissertation Committee, we certify that we have read the dissertation

prepared by Xinyu Miao

entitled Direct and Indirect Searches for New Physics at the Electroweak Scale

and recommend that it be accepted as fulfilling the dissertation requirement for the

Degree of Doctor of Philosophy.

____ Date: 14 October 2010
Shufang Su

____ Date: 14 October 2010
Bira van Kolck

____ Date: 14 October 2010
Douglas Toussaint

____ Date: 14 October 2010
Erich Varnes

Final approval and acceptance of this dissertation is contingent upon the candidate's submission of the final copies of the dissertation to the Graduate College.

I hereby certify that I have read this dissertation prepared under my direction and recommend that it be accepted as fulfilling the dissertation requirement.

____ Date: 14 October 2010
Dissertation Director: Shufang Su

STATEMENT BY AUTHOR

This dissertation has been submitted in partial fulfillment of requirements for an advanced degree at The University of Arizona and is deposited in the University Library to be made available to borrowers under rules of the Library.

Brief quotations from this dissertation are allowable without special permission, provided that accurate acknowledgment of source is made. Requests for permission for extended quotation from or reproduction of this manuscript in whole or in part may be granted by the head of the major department or the Dean of the Graduate College when in his or her judgment the proposed use of the material is in the interests of scholarship. In all other instances, however, permission must be obtained from the author.

SIGNED: Xinyu Miao

ACKNOWLEDGEMENTS

This dissertation would have never been possible without the help from so many people. I am extremely lucky and deeply grateful that I had them around.

I owe my deepest gratitude to my advisor Dr. Shufang Su, for her guidance in physics and in life, for her continuing support and encouragement, for her patience over my repeating episodes. I have been over and over again living a troubled life, but she always saw the potential in me and never gave up on me. I am grateful to all the time and effort she spent in carefully reading and tirelessly commenting on countless revisions of this dissertation.

I would also like to thank professors, peer colleagues and staffs at the Department of the Physics, especially Dr. Bira Van Kolck, Dr. Douglas Toussaint and Dr. Erich Varnes, who kindly accepted to serve on my committee. Though extremely busy, they graciously took the time to read my dissertation and participate in the defense. Their comments and suggestions shaped and polished this dissertation to a much better form. I enjoyed working with Dr. Brooks Thomas on a couple of projects, casual conversation on shared interest made late-night work so pleasant.

I am grateful to have Si Wu and Ziran Wu as friends during the years at Tucson. It was always surprisingly fun and comfortable with them, talking, walking, idling, hiking, cooking, studying... I feel luck to have bumped into Shiyan Zhang, my two-and-half-year-long roommate. The family-like bond gave me peace during times of hesitation and depression.

I owe my parents and my brother everything for their unconditional love, support and understanding.

DEDICATION

To My Family.

TABLE OF CONTENTS

TABLE OF CONTENTS – *Continued*

LIST OF FIGURES

LIST OF FIGURES – *Continued*

LIST OF TABLES

ABSTRACT

The Standard Model (SM) of particle physics is widely taken as an elegant effective theory of nature at the electroweak scale, with new physics expected at higher energy. Collider searches and other experimental inputs play a vital role in our hunt for the unknown physics, offering great insights along the way and eventually establishing the extension to the SM. Here we present our studies on prospects of direct and indirect searches for three types of models beyond the SM.

The Inert Doublet Model (IDM) extends the SM electroweak sector by an extra Higgs doublet with a Z_2-symmetry. We first examine the IDM dilepton signal at the LHC with a center-of-mass energy of 14 TeV and find it exceeding SM backgrounds at 3σ–12σ significance level, with 100 fb^{-1} integrated luminosity. We further show that it is possible to obtain the IDM trilepton signal at the 5σ significance level, with an integrated luminosity of 300 fb^{-1}.

The Left-Right Twin Higgs (LRTH) model solves the little Hierarchy problem by taking the SM Higgs as a pseudo-Goldstone boson from the spontaneous breaking of a global symmetry. We focus on the discovery potential of the heavy top quark partner in the LRTH model at the LHC. With a luminosity of 30 fb^{-1} at the early stage of the LHC operation, we conclude that the heavy top partner could be observed at a significance level above 5σ.

Supersymmetric extensions of the SM enable cancellations among loop corrections to the Higgs mass from bosonic and fermionic degrees of freedom, leading to a solution to the well-known Hierarchy problem. However, the supersymmetry has to be broken by certain mechanism. We present an exploration of the B-physics observables and electroweak precision data in three distinct soft supersymmetry-breaking scenarios. Projection for future sensitivities of the precision data is also explored.

CHAPTER 1

THE STANDARD MODEL AND BEYOND

The Standard Model (SM) of particle physics emerged almost half a century ago and has ever since evolved into a spectacularly successful theoretical framework. Armed with the $SU(3)_C \times SU(2)_L \times SU(1)_Y$ gauge structure and a symmetry breaking mechanism along with other essential ingredients, the SM describes the the strong, the weak and the electromagnetic (EM) interactions of all the elementary particles observed so far (Table 1.1), with astonishing precision as demonstrated by numerous experimental tests. Despite the legacy, the SM is not complete. It is now widely argued that the SM is a low energy effective description of nature, with the more fundamental physics yet to be found. A variety of interesting extensions to the SM have been proposed, awaiting experimental verification.

In this chapter, we first briefly review the key ingredients of the SM framework relevant to later discussion: symmetry and symmetry breaking. Next, the issues with the scalar nature of the Higgs boson and the dark matter issue are discussed. In the following section, we introduce several interesting extensions to the SM relevant to our study: the supersymmetric extension of the SM along with several possible supersymmetry breaking scenarios, the Left-Right Twin Higgs (LRTH) model and the Inert Doublet Model (IDM). In the very last sections, we give an outline of the rest of the dissertation.

1.1 The Standard Model

1.1.1 Gauge Structure and Symmetry Breaking

The history of the SM is a journey of seeking symmetry. Attempts to extend the SM almost exclusively follow the trend with efforts to expand the symmetry embedded in the SM. Here we only briefly review the gauge structure and the Higgs mechanism as

Names	Notation	$SU(3)_C, SU(2)_L, U(1)_Y$
quarks	$Q = (u_L, d_L)$	$(3, 2, \frac{1}{3})$
(× 3 families)	u_R/d_R	$(\bar{3}, 2, +\frac{4}{3}/-\frac{2}{3})$
leptons	$L = (\nu_{e_L}, e_L)$	$(1, 2, -1)$
(× 3 families)	e_R	$(1, 1, 2)$
gluons	G	$(8, 1, 0)$
W bosons	$W^{\pm}$, W^0	$(1, 3, 0)$
B boson	B	$(1, 1, 0)$
Higgs	Φ	$(1, 2, 1)$

Table 1.1: Field content of the SM. Right-handed neutrino is not relevant in this work, thus not listed.

means of spontaneous symmetry breaking. We refer to Ref. [1] for a comprehensive review of the SM.

The SM Lagrangian

The gauge principle in the SM serves as the basis to construct theories of interacting fields [2, 3]. The electroweak (EW) part of the Standard Model is gauged by the $SU(2)_L$ weak-isospin symmetry and the $U(1)_Y$ hypercharge symmetry, while the QCD Lagrangian bears the $SU(3)_C$ gauge structure [4, 5, 6]. The gauge invariant SM Lagrangian can be written down concisely as

$$\mathcal{L}_{SU(3)\times SU(2)\times SU(1)} = \mathcal{L}_{gauge} + \mathcal{L}_{leptons} + \mathcal{L}_{quarks}. \tag{1.1}$$

Four vector bosons are involved in the EW interaction: three weak bosons W_μ's of $SU(2)_L$ and the hypercharge boson B_μ of $U(1)_Y$, while eight Yang-Mills gluon fields G_μ's of $SU(3)_C$ participate in the QCD interaction. For each of the group, we have field strength tensors $F^a_{\mu\nu} = \partial_\mu A^a_\nu - \partial_\nu A^a_\mu - g f^{abc} A^b_\mu A^c_\nu$ for gauge fields A^a_ν, where f^{abc}'s are the structure constants of the group and g is the corresponding coupling constant. For the special case of $U(1)$, $f^{abc} = 0$. The kinetic term for each gauge group can now be specified as [1]

$$\mathcal{L}_{gauge} = -\frac{1}{4} F^a_{\mu\nu} F^{a\mu\nu}. \tag{1.2}$$

Following the notation and the choice of representation in Table 1.1, the SM leptonic and quark terms are

$$\mathcal{L}_{leptons} = \bar{e}_R i\gamma^\mu \mathcal{D}_\mu e_R + \bar{L} i\gamma^\mu \mathcal{D}_\mu L, \tag{1.3}$$

$$\mathcal{L}_{quarks} = \bar{u}_R i\gamma^\mu \mathcal{D}_\mu u_R + \bar{d}_R i\gamma^\mu \mathcal{D}_\mu d_R + \bar{Q} i\gamma^\mu \mathcal{D}_\mu Q, \tag{1.4}$$

where the covariant derivative is defined generally as $\mathcal{D}_\mu = \partial_\mu + i g_s T^a G^a_\mu/2 + i g \tau^a W^a_\mu/2 + i g' Y B_\mu/2$. [2] Here $g_s/g/g'$ are the coupling constants of $SU(3)_C$, $SU(2)_L$ and $U(1)_Y$ respectively. $T^a/2$ and $\tau^a/2$ stand for the generators of $SU(3)_C$ and $SU(2)_L$.

The introduction of the gauge symmetry brings new fields along with interactions into the Lagrangian. The gauge fields couple with the matter content of the SM, as well as with the gauge fields themselves due to the local feature of the gauge symmetry, leading to fascinating phenomenology as confirmed and tested by various experiments.

Spontaneous Symmetry Breaking and the Higgs Mechanism

Gauge invariance guarantees gauge bosons to be massless, contrary to the short range feature of the weak interaction, which requires the intermediate bosons to be massive. The idea of spontaneous symmetry breaking (SSB) [7, 8, 9, 10] adapted in the SM framework resolves the issue by preserving the symmetry of the Lagrangian but not for the vacuum.

The starting point is an additional scalar field Φ with gauge invariant Lagrangian

$$\mathcal{L}_{scalar} = (\mathcal{D}^\mu \Phi)^+ (\mathcal{D}_\mu \Phi) - V(\Phi^+ \Phi). \tag{1.5}$$

---

[1] For brevity, summation over repeated indices and families are always understood unless explicitly stated.

[2] This is only true for left-handed quarks. For right-handed particles, the $SU(2)$ term is dropped; for leptons, the $SU(3)$ term is dropped.

This scalar field can live in any representation of $SU(2)_L \times U(1)_Y$. The simplest choice, as in the minimal Higgs mechanism [11, 12], is one complex doublet

$$\Phi = \begin{pmatrix} \phi^+ \\ \phi^0 \end{pmatrix}, \tag{1.6}$$

with hypercharge $Y = +1$. The potential term V is chosen to be

$$V(\Phi^+\Phi) = \mu^2(\Phi^+\Phi) + \lambda(\Phi^+\Phi)^2, \tag{1.7}$$

such that with $\mu^2 < 0$ and $\lambda > 0$, ϕ^0 ends up with non-zero vacuum expectation (vev) $v = \sqrt{-\mu^2/\lambda}$.

As the original $SU(2)_L \times SU(1)_Y$ symmetry breaks down to $U(1)_{EM}$, three "would-be" massless Goldstone bosons associated with three broken generators become the longitudinal degrees of freedom of the gauge bosons, making physical bosons massive. During the process, gauge eigenstates W^1 and W^2 mix together to form mass eigenstates $W^\pm$, whereas W^3 mixs with B field to form neutral boson Z and photon γ. In addition, one physical Higgs boson emerges once the symmetry breaking is done.

To generate masses for leptons and quarks, a Yukawa interaction part is added:

$$\begin{aligned} \mathcal{L}_{Yukawa} =& - y_e \bar{L}\Phi e_R + h.c. \\ & - y_d \bar{Q}\Phi d_R - y_u \bar{Q}\Phi^c u_R + h.c., \end{aligned} \tag{1.8}$$

where $\Phi^c = -i\tau_2\Phi^*$ is the charge conjugate of the Higgs field. The leptons and quarks acquire masses during the SSB, proportional to the individual coupling y to the Higgs scalar. [3]

Experimental supports for the EW sector are concrete and solid (see Sect. 1.1.2), yet arguments could be made against its elegance. In short, the Higgs boson receives quadratic loop corrections from other field content in the SM due to its scalar nature, which requires an un-natural cancellation set by hand. This is the well known

---

[3] Neutrino masses are generated quite differently. See Ref. [1] for a review of various mechanisms.

Hierarchy problem (see Sect. 1.1.3). Another related issue is the little Hierarchy problem (also see Sect. 1.1.3).

In the minimal SM, only one Higgs doublet is presented which manages to render masses for all gauge and matter particles. The minimal setting in the Higgs sector presents an opportunity when it comes to extending the SM. Intentionally placing the Higgs in a triplet or duplicating an extra doublet (see Sect. 1.2.2) have been proposed in phenomenologically viable models beyond the SM (BSM). Moreover, the introduction of another set of Higgs field might be consequence of an addition symmetry, as in the case of supersymmetry (see Sect. 1.2.1).

1.1.2 Precision Tests

Precision experiments have been essential in establishing the SM, starting from the discovery of the weak neutral current and the intermediate vector bosons. The results in the following decades confirmed the gauge structure and the representation, tested the loop structure and the renormalization principle. By combining experimental inputs and the EW theory, the existence of the top quark was predicted and later confirmed [13]. As these tests march towards higher and higher precision, the power of the SM in correlating experimental observables starts to be appreciated. However, as people now firmly believe that the SM is simply not the end of the story, it is reasonable to expect hints of new physics from precision observables.

The precision on the chosen experimental observables has been improved a great deal beyond the predicting power of tree-level calculations [1]. In order for a sensible comparison, high order radiative corrections must be included when computing these observables within the SM framework. Of particular interest are the radiative correction to the W boson mass, the effective leptonic weak mixing angle $\sin^2\theta_{eff}$ and the anomalous magnetic moment of the muon $a_\mu = (g_\mu - 2)/2$, which are relatively more sensitive to possible new physics corrections. In connection to later discussion, current status of M_W, $\sin^2\theta_{eff}$ and a_μ is briefly reviewed here [1]. Later in Chapter 3, we will discuss about these quantities evaluated in the supersymmetric framework.

The W boson mass can be conveniently written down in terms of the fine structure constant α and the Fermi constant G_F as

$$M_W^2\left(1-\frac{M_W^2}{M_Z^2}\right)=\frac{\pi\alpha}{\sqrt{2}G_F}(1+\Delta r), \tag{1.9}$$

where Δr summarizes radiative corrections from higher order loops. M_W is now best measured to be 80.420 ± 0.031 GeV, compared with SM prediction 80.384 ± 0.014 GeV with QED, QCD and EW corrections up to three-loop order [14, 1]. The effective leptonic weak mixing at the Z-pole can be written as

$$\sin^2\theta_{eff}=\frac{1}{4}\left(1-Re\frac{g_V}{g_A}\right), \tag{1.10}$$

where g_V and g_A are the effective vector and axial couplings of the Z boson to quarks and leptons once the vertex correction to $Z\bar{f}f$ is included [15]. SM predicts a mixing of 0.23146 ± 0.00012, compared with Z-pole extracted mixing of 0.2316 ± 0.0018 [15, 1].

Leptonic anomalous magnetic moments, especially a_e of electron, have traditionally provided precision test of the SM. Compared with a_e, the muon anomalous magnetic moment a_μ is measured experimentally a few hundreds time less precisely. However, the fact that loop corrections are mostly proportional to m_μ together with the ratio $m_\mu^2/m_e^2 \approx 40000$, makes a_μ a much better test of SM and probe of new physics. a_μ receives QED contributions, electroweak correction, hadronic vacuum polarization, etc.:

$$a_\mu = a_\mu^{QED} + a_\mu^{EW} + a_\mu^{had}. \tag{1.11}$$

The QED and EW contributions have been computed (estimated) to 5-loop and 3-loop level respectively [1]. The hadronic corrections are not calculable from first principle, but can be evaluated from corresponding hadronic cross sections via a dispersion integral [16]. As in Chapter 3, we make use of $a_\mu^{SM} = (11659180.5 \pm 4.4 \pm 3.5 \pm 0.2) \times 10^{-10}$ (with a_μ^{had} estimated from e^+e^- data) and the final result of Brookhaven experiment $a_\mu^{exp} = (11659208.0 \pm 6.3) \times 10^{-10}$.

The excellent consistency between the SM values and the precision measurements, as demonstrated above in the example of M_W, $\sin^2\theta_{eff}$ and a_μ, leaves little margin for possible new physics. Thus no matter how interesting and beautiful the proposed extensions to the SM are, contributions to precision observables must not violate current or future experimental bounds. The precision variables can thus be used to constrain proposed extensions to the SM.

In Chapter 2, we will show how the application of current bounds onto the parameter space of BSM models facilitate collider searches. In Chapter 3, we will take into account additional supersymmetric loop corrections when comparing theoretical predictions with experimental observables. We present there an exploration of electroweak precision observables (EWPO) together with B-Physics observables in various soft supersymmetry-breaking scenarios.

1.1.3 Problems with the SM

The Standard Model is by far the greatest achievement of particle physics, which explains three distinct forces with different strengths/ranges and passes impressively the most rigorous experimental tests. Though the experimental energy frontier has advanced into TeV scale, there has been no convincing evidence of new physics.

However the SM still can not be regarded as complete: there are (more than) 27 arbitrary parameters that have to be manually set; the choice of the somewhat complicated group structure and the charge quantization is not explained; the family structure and mixing among families are not understood fundamentally; gravity is not incorporated, etc. We focus in this section on issues concerning the EW sector as well as the absence of the dark matter candidate.

Hierarchy Problem

The Standard Model requires a non-vanishing vev v for the scalar field introduced in the spontaneous symmetry breaking of $SU(2)_L \times U(1)_Y$ down to the observed $U(1)_{EM}$ at low energy. The mass of the physical Higgs boson H is related to the vev by $m_H^2 = 2\lambda v^2 = -2\mu^2$, given that $\lambda > 0$ and $\mu^2 < 0$. Through the precision measurement in the weak sector, particularly the Fermi constant G_F, we know that

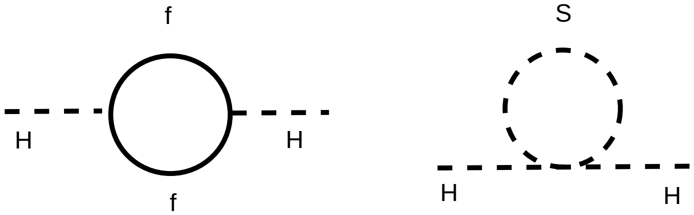

Figure 1.1: One-loop quantum correction to the Higgs mass from fermion (left panel) and scalar (right panel).

$v = (\sqrt{2}G_F)^{-\frac{1}{2}} \sim 246$ GeV. Provided $\lambda \sim O(1)$, m_H^2 is roughly of order (100 GeV)^2.

The problem now is that any scalar mass parameter receives quantum corrections from loops of higher order. For the Higgs boson, m_H^2 gets contributions from all the SM particles, no matter whether they couple directly or indirectly. For example, fermions in the SM give rise to loop correction depicted in Fig. 1.1, with a mass of m_f and a coupling strength of y_f.

The fermionic diagram in Fig. 1.1 can be easily evaluated and yields a correction to m_H^2 of

$$\Delta m_H^2 = -\frac{|y_f|^2}{8\pi^2}\Lambda_{UV}^2 + \cdots , \tag{1.12}$$

where Λ_{UV} is an ultraviolet cutoff in momentum space [4] to regulate the integral. Λ_{UV} should be understood as the energy scale where new physics comes in and takes over the high energy behavior. The integral, proportional to Λ_{UV}^2, is quadratically divergent. Moreover, f can be any of the SM leptons and quarks (with an extra factor of 3 for quarks to take into account color factor). Of all the contributions, the dominant one comes from the top quark due to the large coupling strength

---

[4] If one uses the dimensional regularization, there will be unjustifiable tuning of counter-terms as well. See Ref. [17] for detail.

$y_t \sim O(1)$, which is orders of magnitudes larger than others.

A natural scale for Λ_{UV} is the Planck scale M_{Planck}, if one is willing to consider the QCD and the electroweak theory as fundamental and no new physics exists till the energy scale where the quantum gravity effect starts to manifest. Given that $M_{Planck} = (8\pi G_{Newton})^{-\frac{1}{2}} \sim 10^{19}$ GeV, this quantum correction is about 30 orders of magnitudes larger than the required $m_H^2 \sim (100 \text{ GeV})^2$.

To mitigate the fine-tuning, the first natural attempt is to lower the cutoff scale. An alternative scale is the unification scale $\sim 10^{15} - 10^{16}$ GeV in a unified theory of the strong, the weak and the EM interactions, which helps little with a fine-tuning of more than 20 orders of magnitudes. A desperate rescue is an extreme fine-tuning: set the bare mass squared in the Lagrangian to be close to this enormous correction, so as to magically cancel it out, leaving us $m_H^2 \sim (100 \text{ GeV})^2$. Or rather cleverly, we could introduce new symmetries or new dynamics beyond the ones presented in current Standard Model.

Supersymmetry (SUSY) exploits the fact that bosonic loop corrections to m_H^2 are also proportional to Λ_{UV}^2, but of the opposite sign than that from the fermion loop. A one-loop diagram of a complex scalar particle S with mass m_S and coupling vertex $\lambda_S|H|^2|S|^2$ is given in Fig. 1.1. With exact supersymmetry, the loop correction from the bosonic super-partner cancels precisely the contribution from the fermion loop. However, exact supersymmetry implies degenerate masses for a particle and its super-partner. Since we do not observe experimentally any evidence of such degenerate masses, the supersymmetry has to be broken somehow. However, as long as SUSY breaking is “soft” (see Sect. 1.2.1) and the mass splittings are not too large, supersymmetry still provides acceptable cancellation.

There are alternative solutions to the Hierarchy problem without relying on symmetry. Models with extra dimensions [18, 19] assume that gravity propagates in, on top of the 3+1 dimensional space, extra spatial dimensions. The fundamental Plank scale in this case M might be a lot smaller, probably around weak scale, than the effective four-dimensional Plank scale: $M_{Planck}^2 \approx M^{n+2}V_n$, where V_n is the volume of the extra space. For compactified large extra dimensions, gravity becomes weak because of the loss of flux to extra dimensions. It is also possible that the extra dimensions are warped [20], in which case the extra dimension is not required to be extremely large. Gravity is weak on the visible brane because of the exponential warp factor in metric. Another possibility is to eliminate the fundamental scalar, with bilinear fermion condensate taking the role of the Higgs boson and dynamically breaking the electroweak symmetry. Technicolor models [21] fall into this category.

Little Hierarchy Problem

The little Hierarchy problem refers to the "LEP paradox" derived from the precision electroweak measurements at LEP. Though the hierarchy involved (5 - 10 TeV) is no where as big as the hierarchy between the Plank scale and the EW scale, it still leaves room for quite large radiative corrections to the Higgs mass, which again requires a fairly large amount of fine-tuning.

The self-consistency of the Standard Model, particularly the perturbative unitarity condition and triviality condition lead to upper bounds on the Higgs mass. Perturbative unitary condition, in the analysis of two-body scatterings between longitudinal bosons W_L, Z_L and the Higgs, requires that [22]

$$m_H \leq (\frac{8\pi\sqrt{2}}{3G_F})^{\frac{1}{2}} \approx 1 \text{ TeV}. \tag{1.13}$$

Triviality condition [23, 24] requires Higgs potential to be stable up to the scale Λ where new physics takes over: $\lambda(\Lambda) > 0$. The Renormalization Group Equation (RGE),

$$\frac{1}{\lambda(\Lambda)} = \frac{1}{\lambda(m_H)} - \frac{3}{4\pi^2}\log\frac{\Lambda^2}{m_H^2}, \tag{1.14}$$

then implies an inequality on $\lambda(m_H)$. Choosing the cutoff scale Λ to be around the unification scale or the Plank scale leads to another upper bound $m_H < 170\text{GeV}$ [22].

On the experimental side, precision electroweak measurements performed at LEP over the past decades indicate a light Higgs as well. The Higgs mass enters into the electro-weak precision test (EWPT) observables through the oblique parameter S

[25] and $\Delta\rho$, the correction to

$$\rho = \frac{M_W^2}{M_Z^2 \cos^2\theta}. \tag{1.15}$$

A global fit of the EWPT observables within the SM has constrained the Higgs mass below 186 GeV at 95% C.L. [1], which is consistent with the upper bounds from unitarity and triviality conditions.

On the other hand, one could examine the same EWPT data, taking the SM as the effective low energy approximation of some new physics high above the electroweak scale. The new physics affects the EWPT observables through non-renormalizable operators of dimension ≥ 5, weighted by the corresponding inverse orders of the cutoff scale Λ:

$$\mathcal{L}(E < \Lambda) = \mathcal{L}_{SM} + \sum_{i,p} \frac{c_i}{\Lambda^p} \mathcal{O}_i^{4+p}, \tag{1.16}$$

where c_i is some dimensionless coefficient taken to be of order 1 and $4 + p$ is the dimension of the operator $\mathcal{O}_i$. The analysis of EWPT data leads to Λ around 5 - 10 TeV [26], resulting in a “little” hierarchy above the EW scale.

There have been several attempts to address the little Hierarchy problem. In the little Higgs model [27], the Higgs is the pseudo-Goldstone boson of an approximate global symmetry[28, 29]. This global symmetry is broken when more than one coupling in the Lagrangian are non-vanishing. The collective symmetry breaking mechanism makes the radiative corrections to the Higgs at most logarithmic; the fine-tuning is thus well controlled [30, 31, 32]. Twin Higgs model [33, 34, 35] employs a similar idea of imposing a global symmetry for the Higgs sector. Upon invoking a discrete left-right symmetry [36], the quadratic contribution to the Higgs potential respects the global symmetry. Again the leading divergence in one-loop correction to the Higgs mass squared is at most logarithmic.

Dark Matter

A variety of observational evidence support the existence of dark matter (DM) as major constitutes of the universe (for a recent review, see [37]). The currently most precise measurement of matter density comes from Wilkinson Microwave Anisotropy Probe (WMAP) experiment (Fig. 1.2). The observational data [1] so far indicate a total matter density of $\Omega_m h^2 = 0.133 \pm 0.006$, out of which baryonic matter contributes just $\Omega_b h^2 = 0.0227 \pm 0.0006$, leaving the majority un-accounted for.

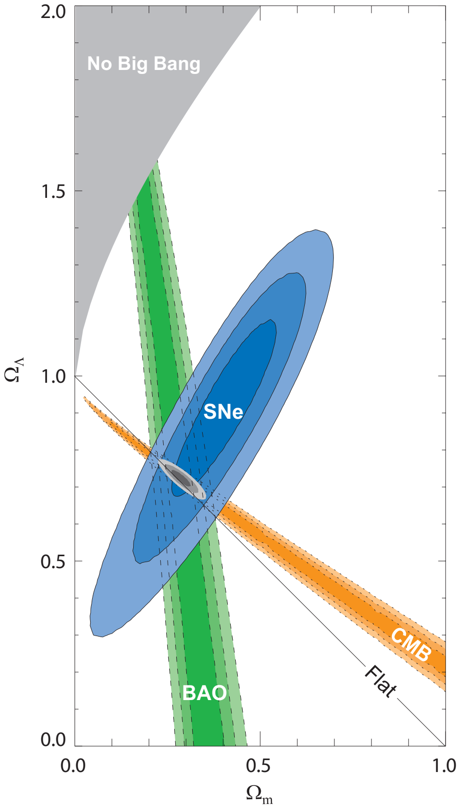

Figure 1.2: Confidence level contours of 68.3%, 95.4% and 99.7% in the Ω_Λ-Ω_m plane from the Cosmic Microwave Background, Baryonic Acoustic Oscillations and the Union SNe Ia set. Plot extracted from Ref.[38].

Further analysis of the data indicates that most of the dark matter should be moving non-relativistically, or "cold", which agrees with the 95% C.L upper bound for the neutrino type dark matter, $\Omega_\nu h^2 \leq 0.00067$ [1]. Furthermore, DM candidates must be stable on cosmological scales to be seen today. They also must be very weakly involved in electromagnetic interaction to qualify as dark matter. The requirements above eliminate all SM particles as valid DM candidate. Alternatives include primordial black holes, axions and weakly interacting massive particles (WIMPs), etc.[39].

Among all DM candidates, WIMPs naturally lead to a relic density close to the observational value, which makes it one of the most popular. In the early universe, temperature was way above the mass m_X of the candidate particle X, so particle X was thermally abundant at the equilibrium state of the creation and self-annihilation processes. As the universe expanded, the number density of X dropped to a threshold below which the annihilation process stoped - particle X froze out. It can be shown that the freeze out density of X is approximately

$$\Omega_X h^2 \approx \frac{10^{-10}\text{GeV}^{-2}}{\langle \sigma_{X\bar{X}} |v| \rangle}, \tag{1.17}$$

where $\langle \sigma_{X\bar{X}} |v| \rangle$ is the average annihilation cross-section multiplied by the relative velocity. The WIMP typically has a mass around the weak scale m_{weak}, thus

$$\langle \sigma_{X\bar{X}} |v| \rangle \propto \frac{\alpha^2}{m_{weak}^2} \approx 10^{-9}\text{GeV}^{-2}, \tag{1.18}$$

which leads to a relic density (~ 0.1) naturally at the order of the observed dark matter density.

Many extensions of the SM addressing the electro-weak symmetry breaking (EWSB) naturally contain WIMP candidates. The stability requirement is often easily met, since most of the extensions have to impose a discrete symmetry to avoid large proton decay rate or large electroweak correction. The lightest particle with different parity from the SM fields would then be stable. Examples are the lightest supersymmetric particle (LSP) in SUSY with R-parity, the lightest KK particle (LKP) with KK-parity, the lightest inert particle (LIP) with Z_2 symmetry, etc. Any legitimate candidate must result in the right relic density and satisfy the bounds from all current direct and indirect searches, which can be used as another constraint on new physics models, as is demonstrated in Chapter 2 and 3.

1.2 Beyond the Standard Model (BSM)

With all the puzzles and missing pieces, it is plausible to claim extensions to the SM to be inevitable. A great deal of efforts have been made towards a solution to issues associated with the current SM framework. Out of all BSM models in the literature, we focus on three, namely the supersymmetric extension of the SM (with different SUSY-breaking mechanisms), the Inert Doublet Model and the Left-Right Twin Higgs model. The phenomenology of aforementioned models will be the subjects of the investigations carried out in Chapter 2 and Chapter 3.

1.2.1 Supersymmetry (SUSY) and SUSY Breaking

The idea that SUSY might serve to solve the SM fine-tuning problem or the Hierarchy problem was proposed by Witten [40], Veltman [41] and Kaul [42]. The radiative corrections to Δm_H^2 from bosonic one-loop diagram and fermionic one-loop diagram are both quadratic in Λ_{UV}^2, but of opposite signs. A systematic cancellation is possible if the couplings of the Higgs to the scalar field is made equal to that of the fermionic field. This fact naturally alerts for a possible symmetry - supersymmetry - that relates bosonic degrees of freedom to fermionic ones. Exact SUSY ensures that the neat cancellation not only occurs at one-loop, but persists to higher orders.

MSSM and Soft Breaking

One supersymmetric extension of the SM is the Minimum Supersymmetric Standard Model (MSSM), which postulates superpartner(s) for each of the SM particles with spin differing by a half (Table 1.2 and 1.3). Exact SUSY implies equal mass among the pair of particle and super particle. For example selectron $\tilde{e}$, the superpartner of electron would have the same mass as electron e. However, no superpartner for the SM particles has yet been observed so far. Thus SUSY, if it exists as to solve the Hierarchy problem, has to be a broken symmetry. And there is no exact cancellation between the bosonic and fermionic radiative correction to the Higgs mass squared. However, a "softly" broken SUSY with scale m_{soft} still manages to solve the SM fine-tuning problem, by lowering the Λ_{UV}^2 correction down to logarithmic order $\sim m_{soft}^2 \log(\Lambda_{UV}/m_{soft})$, provided that m_{soft} is no heavier than a few TeV.

Names		spin 0	spin $\frac{1}{2}$	$SU(3)_C, SU(2)_L, U(1)_Y$
squarks, quarks	Q	$(\tilde{u}_L, \tilde{d}_L)$	(u_L, d_L)	$(3, 2, \frac{1}{3})$
(× 3 families)	$\bar{u}$	$\tilde{\bar{u}}_L$	$\bar{u}_L$	$(\bar{3}, 1, -\frac{4}{3})$
	$\bar{d}$	$\tilde{\bar{d}}_L$	$\bar{d}_L$	$(\bar{3}, 1, \frac{2}{3})$
sleptons, leptons	L	$(\tilde{\nu}_{eL}, \tilde{e}_L)$	(ν_{eL}, e_L)	$(1, 2, -1)$
(× 3 families)	$\bar{e}$	$\tilde{\bar{e}}_L$	$\bar{e}_L$	$(1, 1, 2)$
Higgs, Higgsinos	H_u	(H_u^+, H_u^0)	$(\tilde{H}_u^+, \tilde{H}_u^0)$	$(1, 2, 1)$
	H_d	(H_d^0, H_d^-)	$(\tilde{H}_d^0, \tilde{H}_d^-)$	$(1, 2, -1)$

Table 1.2: Chiral supermultiplets in the MSSM

Names	spin 0	spin $\frac{1}{2}$	$SU(3)_C, SU(2)_L, U(1)_Y$
gluinos, gluons	$\tilde{g}$	g	$(8, 1, 0)$
winos, W bosons	$\tilde{W}^{\pm}, \tilde{W}^0$	$W^{\pm}, W^0$	$(1, 3, 0)$
bino, B boson	$\tilde{B}$	B	$(1, 1, 0)$

Table 1.3: Gauge supermultiplets in the MSSM

From a theoretical perspective, it is reasonable to expect SUSY to be an exact symmetry at certain high energy scale but spontaneously broken at low energy, very much similar to the electro-weak symmetry in the SM. The mechanism for SUSY breaking is not clear (for various conjectured SUSY breaking scenarios, see the next few sections), however a low energy effective parametrization of the soft SUSY-breaking terms can be formulated for phenomenological purpose. The possible gauge invariant soft SUSY-breaking terms are

$$\begin{aligned}
\mathcal{L}_{soft} = & -\frac{1}{2}(M_3\tilde{g}^a\tilde{g}^a + M_2\tilde{W}^a\tilde{W}^a + M_1\tilde{B}^a\tilde{B}^a + h.c.) \\
& - m^2_{\tilde{Q}ij}\tilde{Q}^\dagger_i\tilde{Q}_j - m^2_{\tilde{\bar{u}}ij}\tilde{\bar{u}}^\dagger_{Li}\tilde{\bar{u}}_{Lj} - m^2_{\tilde{\bar{d}}ij}\tilde{\bar{d}}^\dagger_{Li}\tilde{\bar{d}}_{Lj} \\
& - m^2_{\tilde{L}ij}\tilde{L}^\dagger_i\tilde{L}_j - m^2_{\tilde{\bar{e}}ij}\tilde{e}^\dagger_{Li}\tilde{e}_{Lj} \\
& - m^2_{H_u}H^\dagger_uH_u - m^2_{H_d}H^\dagger_dH_d - (bH_uH_d + h.c.) \\
& - a^{ij}_u\tilde{\bar{u}}_{Li}\tilde{Q}_jH_u + a^{ij}_d\tilde{\bar{d}}_{Li}\tilde{Q}_jH_d + a^{ij}_e\tilde{\bar{e}}_{Li}\tilde{L}_jH_d + h.c.,
\end{aligned} \tag{1.19}$$

where each line includes respectively: gaugino mass, squark masses, slepton masses, Higgs mass terms and triple scalar coupling terms. To keep the cancellation in quadratic radiative corrections to the Higgs mass at a satisfactory level, these terms must be "soft", i.e. the coupling and mass parameters are associated with a characteristic mass scale $m_{soft} \sim$ TeV.

It has been shown [43] that there are a total of 105 new parameters (masses, phases and mixing angles) in the above soft SUSY-breaking terms. Fortunately, experiments on flavor-mixing or CP-violating processes constrain severely most of the soft parameters. Usually the hypothesis of "soft SUSY-breaking universality" is assumed, where masses of the squarks and sleptons with the same quantum numbers are degenerate and the triple scalar coupling matrix is proportional to the corresponding Yukawa matrix with no CP-violating phase introduced. Furthermore, the above principle is assumed to hold at some very high SUSY-breaking scale specific to the underlying SUSY-breaking mechanism. The relations among the SUSY-breaking parameters should then be understood as the boundary conditions on the Renormalization Group (RG) running of the soft parameters. Once being evolved to the EW scale, the relations no longer hold. But the violations are usually "minimal", in the sense that the resulting flavor-changing and CP-violating observables are acceptably small.

For the supersymmetry to be spontaneously broken at the SUSY-breaking scale, one could construct models where either the D-terms [44] or the F-terms [45] develops a vev. However, it has been shown that the former does not lead to an acceptable spectrum and there is no gauge singlet in MSSM with F-term that could develop a vev [45]. Thus it is necessary to add a SUSY breaking sector (the hidden sector), that is responsible for the breaking and communicates with the MSSM (the visible sector). Three SUSY breaking scenarios are briefly examined below.

Constrained MSSM

In the constrained MSSM (CMSSM) [46], SUSY-breaking occurs in a hidden sector where the auxiliary field F for certain chiral supermultiplet develops a vev $\langle F \rangle$. The hidden sector communicates with the visible sector through gravitational interaction terms which are suppressed by the Planck scale M_{Plank}. The soft terms in the visible sector should be $m_{soft} \sim \langle F \rangle / M_{plank}$, since $m_{soft} \to 0$ when there is no breaking $\langle F \rangle \to 0$ and when gravity effect is negligible $M_{Plank} \to \infty$.

In the minimal form of CMSSM, the soft terms take a simple pattern:

$$M_3 = M_2 = M_1 = m_{1/2}, \tag{1.20}$$

$$\mathbf{m}^2_{\tilde{Q}} = \mathbf{m}^2_{\tilde{\bar{u}}} = \mathbf{m}^2_{\tilde{\bar{d}}} = \mathbf{m}^2_{\tilde{L}} = \mathbf{m}^2_{\tilde{\bar{e}}} = m_0^2 \mathbf{1}, \tag{1.21}$$

$$m^2_{H_u} = m^2_{H_d} = m_0^2, \tag{1.22}$$

$$\mathbf{a}_u = A_0 \mathbf{y}_u, \mathbf{a}_d = A_0 \mathbf{y}_d, \mathbf{a}_e = A_0 \mathbf{y}_e, \tag{1.23}$$

where the high energy parameters satisfy

$$m_{1/2} \sim \frac{\langle F \rangle}{M_{plank}}, \qquad m_0^2 \sim \frac{\langle F \rangle^2}{M^2_{plank}}, \qquad A_0 \sim \frac{\langle F \rangle}{M_{plank}}. \tag{1.24}$$

To have m_{soft} around TeV scale, $\sqrt{\langle F \rangle}$ must be of order 10^{10} GeV.

The set of parameters that fully specify the CMSSM is thus

$$\{m_0, m_{1/2}, A_0, \tan\beta, sign(\mu)\}, \tag{1.25}$$

where $\tan\beta$ and $sign(\mu)$ are, respectively, the ratio of the two Higgs vev's and the sign of the coefficient μ of the Higgs mass term in the superpotential.

mGMSB

In the minimal gauge-mediated supersymmetry breaking (mGMSB) [47], the scalar S and corresponding auxiliary field F_S acquire vev's during SUSY breaking in the hidden sector. The effect of SUSY breaking is then mediated by these messenger particles through radiative correction to the MSSM masses and couplings.

For example, the gaugino masses at one-loop order and scalar masses at two-loop order are

$$M_a = \frac{\alpha_a}{4\pi}\Lambda N_{mess}, \tag{1.26}$$

$$m^2_{\phi_i} = 2\Lambda^2 N_{mess}\sum_{a=1}^{3} C_a(i)\left(\frac{\alpha_a}{4\pi}\right)^2, \tag{1.27}$$

where N_{mess} are the number of copies of messengers and $\Lambda = \langle F_S\rangle/\langle S\rangle$ is the ratio of the SUSY breaking vev's. In the above equation, the α_a's and C_a's are the coupling strength and the Casimir invariants of the $SU(3)_c \times SU(2)_L \times U(1)_Y$ groups. The $\mathbf{a}_u, \mathbf{a}_d$ and $\mathbf{a}_e$ can be taken as zero, since the messenger loop corrections are greatly suppressed.

The general feature of this type of SUSY breaking scenarios is that the strongly interacting sparticles are heavier than weakly interacting sparticles, due to the coupling strength difference. Another interesting conclusion is that the LSP is most likely to be the gravitino.

The complete set of parameters that fully characterize the mGMSB is

$$\{M_{mess}, N_{mess}, \Lambda, \tan\beta, sign(\mu)\}, \tag{1.28}$$

where M_{mess} is the overall mass scale of the messengers and $M_{mess} \sim \langle S\rangle$.

mAMSB

In the minimal anomaly mediated supersymmetry breaking (mAMSB) [48], SUSY breaking occurs in a hidden brane separated certain distance away from the MSSM brane on an extra spacial dimension. During the spontaneous symmetry breaking, the auxiliary field develops a vev on the hidden brane:

$$\frac{\langle F\rangle}{M_{plank}} \sim m_{aux}. \tag{1.29}$$

The SUSY breaking is then transmitted to the MSSM brane through non-zero beta functions and anomalous dimensions of the couplings and fields [47, 48, 17] in loop diagrams:

$$M_a = m_{aux}\beta_{g_a}/g_a, \tag{1.30}$$

$$(m^2)^i_j = \frac{1}{2}m^2_{aux}\left[\beta_{g_a}\frac{\partial\gamma^i_j}{\partial g_a} + \left(\beta_{y^{kmn}}\frac{\partial\gamma^i_j}{\partial y^{kmn}} + c.c.\right)\right], \tag{1.31}$$

$$a^{ijk} = -m_{aux}\beta_{y^{ijk}}, \tag{1.32}$$

where the β's are the beta-functions and γ's are the anomalous dimensions [47, 48, 17].

It is however found that the slepton masses squared are negative. For remedy, a common phenomenological *ad-hoc* parameter m_0^2 is usually added to all the scalar masses at SUSY-breaking scale.

The complete set of parameters that fully characterize the mAMSB is thus

$$\{m_{aux}, m_0, \tan\beta, sign(\mu)\}. \tag{1.33}$$

1.2.2 Inert Doublet Model

In the SM, electroweak symmetry breaking is triggered by a single Higgs doublet once the $T_3 = -\frac{1}{2}$ component develops a vev. This is just the "minimal" version of the Higgs mechanism. Higgs sector could take the form of a triplet [49] instead, or multiple copies of the Higgs doublets, as in the MSSM where an extra doublet is added.

The Inert Doublet Model extends the Higgs sector with a new Higgs doublet and imposes a Z_2 symmetry under which

$$\Phi_1 \to \Phi_1, \qquad \Phi_2 \to -\Phi_2. \tag{1.34}$$

Here Φ_1 acts like the SM Higgs in EWSB with a vev for the neutral component $\langle \Phi_1^0 \rangle = 246$ GeV while the Φ_2 does not contribute to the EWSB: $\langle \Phi_2 \rangle = 0$. The new Higgs doublet does not couple to fermions in the SM due to the Z_2 symmetry, thus dubbed "inert". However, the inert sector does couple to the gauge bosons.

The IDM, simple as it is, finds applications in explaining the neutrino mass through a radiative seesaw mechanism [50], constructing loop-level electroweak symmetry breaking [51], rendering a natural candidate for the dark matter and solving the naturalness problem [52] (the Little Hierarchy problem) posed by electroweak precision data. Most interestingly, it accommodates naturally a heavy Higgs [52].

Scalar Potential and Mass Spectrum of the IDM

Upon imposing this Z_2 symmetry, the most general CP-even scalar potential of dimension up to 4 takes the form

$$\begin{aligned} V = {} & \mu_1^2 |\Phi_1|^2 + \mu_2^2 |\Phi_2|^2 + \lambda_1 |\Phi_1|^4 + \lambda_2 |\Phi_2|^4 \\ & + \lambda_3 |\Phi_1|^2 |\Phi_2|^2 + \lambda_4 |\Phi_1^\dagger \Phi_2|^2 + \left[\frac{\lambda_5}{2} (\Phi_1^\dagger \Phi_2) + h.c. \right] . \end{aligned} \tag{1.35}$$

After EWSB is triggered by the vev of Φ_1,

$$\Phi_1 = \begin{pmatrix} 0 \\ \frac{v+h}{\sqrt{2}} \end{pmatrix} , \tag{1.36}$$

the scalar spectrum of the model comprises the usual SM Higgs h (the neutral, CP-even degree of freedom in Φ_1), as well as four additional fields corresponding to the four degrees of freedom in Φ_2,

$$\Phi_2 = \begin{pmatrix} H^\dagger \\ \frac{S+iA}{\sqrt{2}} \end{pmatrix} . \tag{1.37}$$

These include a pair of charged scalars $H^\pm$, a neutral, CP-even scalar S, and a neutral, CP-odd scalar A. The masses of these scalars, given in terms of the six free parameters[5] $\{\mu_2^2, \lambda_1, \lambda_2, \lambda_3, \lambda_4, \lambda_5\}$ in Eq. (1.35), are

$$\begin{aligned} m_h^2 &= 2\lambda_1 v^2, &(1.38)\\ m_{H^\pm}^2 &= \mu_2^2 + \lambda_3 v^2/2, &(1.39)\\ m_S^2 &= \mu_2^2 + (\lambda_3+\lambda_4+\lambda_5)v^2, &(1.40)\\ m_A^2 &= \mu_2^2 + (\lambda_3+\lambda_4-\lambda_5)v^2/2. &(1.41)\end{aligned}$$

Also present in the potential, are the couplings from the inert scalars S and A to the SM Higgs h:

$$\lambda_3 v h H^+ H^- + \frac{1}{2}(\lambda_3+\lambda_4+\lambda_5) v h S S + \frac{1}{2}(\lambda_3+\lambda_4-\lambda_5) v h A A, \tag{1.42}$$

which opens new decay channels for the SM Higgs:

$$h \to SS, AA, H^+H^-. \tag{1.43}$$

The SM Higgs decay width as well as the branching ratios can be significantly altered in certain region of the parameter space [52, 53].

A Heavy SM Higgs

One of the fascinating aspects of the IDM is that it naturally accommodates a heavy Higgs with mass up to 400 GeV – 600 GeV without violating the electroweak precision data. Now since the Higgs mass is raised, a relatively larger cutoff scale in the quadratic divergence can be regarded as tolerable, concerning the "naturalness" of the model and the relative amount of fine-tuning. This is another approach of addressing the "LEP paradox" [26].

It is often quoted that the electroweak precision observables indicate a light Higgs: $m_h < 186$ GeV at 95% C.L. [1]. This is obvious upon examining the m_h effect on the the oblique parameters S and T [25]:

$$\Delta T \approx -\frac{3}{8\pi}\log\frac{m_h}{m_Z}, \tag{1.44}$$

$$\Delta S \approx \frac{1}{6\pi}\log\frac{m_h}{m_Z}. \tag{1.45}$$

---

[5] The seventh parameter μ_1^2 appearing in Eq. (1.35) is fixed by the constraint $v^2 = -\mu_1^2/\lambda_1$ from EWSB.

A sufficiently large m_h would easily induce an escape from the experimental limits. As shown in Fig. 1.3, a Higgs of 400 – 600 GeV walks away from the precision bound by a $\Delta T \sim -0.25$. However it should be noted that, the aforementioned analysis of the electroweak precision data which leads to the Higgs mass bound is performed within the minimal SM framework, in absence of any new physics.

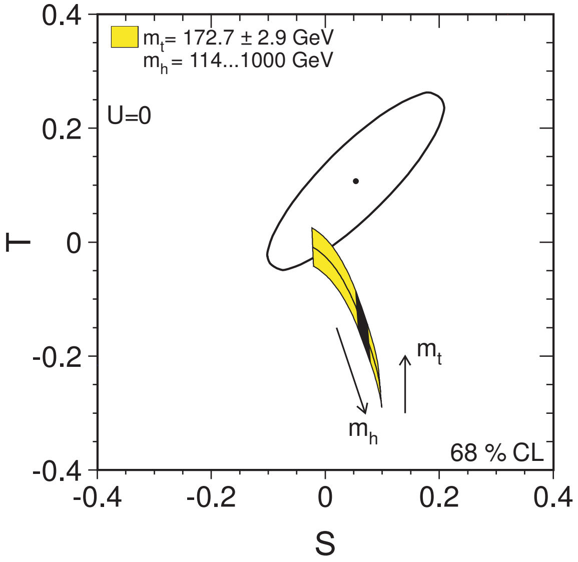

Figure 1.3: STU contour in the SM. The solid ellipse represents the 68% C.L.bound. Plot extracted from Ref.[38].

In the IDM, the story is different. The additional inert doublet brings T back to the 68% C.L. ellipse by contributing another piece [38]:

$$\Delta T = \frac{1}{32\pi^2 \alpha v^2}\left[f(m_{H^\pm}, m_A) + f(m_{H^\pm}, m_s) - f(m_A, m_S)\right], \tag{1.46}$$

where the function f is defined as

$$f(m_1, m_2) = \frac{m_1^2 + m_2^2}{2} - \frac{m_1^2 m_2^2}{m_1^2 - m_2^2} \log \frac{m_1^2}{m_2^2}. \tag{1.47}$$

To have a compensating $\Delta T \sim +0.25$, it is sufficient to require the masses squared to follow

$$(m_{H^\pm} - m_S)(m_{H^\pm} - m_A) \approx (120\text{GeV})^2. \tag{1.48}$$

As long as the charged inert scalar is heavier than both of the neutral scalars, the inert sector produces a positive ΔT. It is shown that there exists regions in the parameter space of the IDM where the above equation holds while being phenomenologically viable.

The parameter space of the IDM is fairly high-dimensional, however it is subject to a number of constraints (details in Sect. 2.1). On the theoretical side, the parameters are restricted by the vacuum stability requirement and perturbativity consideration. Experimentally, electroweak precision measurements exclude processes $W^{\pm} \to SH^{\pm}, AH^{\pm}, Z \to SA, H^{+}H^{-}$, each leading to a restriction on the masses of the S, A and $H^{\pm}$. Bounds obtained from direct search for neutralino in supersymmetric model at LEP can be translated [38] into that applicable to the IDM. Fig. 1.4 shows the LEP exclusion region in the m_S–m_A plane. Lastly, the IDM is also subject to limits from various dark matter detection/measurements. The unbroken Z_2 symmetry guarantees the lightest inert particle to be absolutely stable, and due to the "inert" feature, it arises as a perfect candidate for a WIMP dark matter.

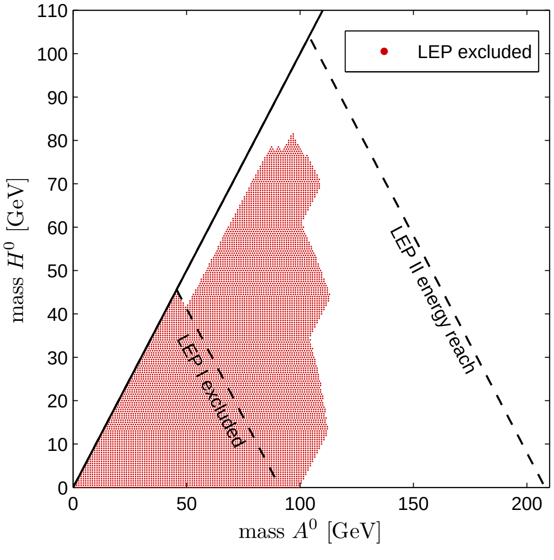

Figure 1.4: LEP exclusion region in the m_S–m_A plane. A different notation is understood here: S for H_0 and A for A^0. Plot extracted from Ref. [38].

The IDM manages to address the little Hierarchy problem by raising the mass of the SM Higgs, such that the relative fine-tuning is tolerable. However, there are other models with different mechanisms that also successfully reduce the level of fine-tuning. The Left-Right Twin Higgs model, for example, is one of the promising conjectures.

1.2.3 Left-Right Twin Higgs Model

The twin Higgs model employs the idea of the Higgs as a pseudo-Goldstone boson from the spontaneous breaking of a global symmetry. The gauge interactions and Yukawa interactions break the global symmetry, resulting in a potential for the Goldstone bosons, in particular the Higgs boson. If an additional discrete symmetry is imposed, the quadratic term in the radiative correction to the Higgs potential would respect the global symmetry, such that it does not contribute to the Higgs mass. The level of fine-tuning is greatly lowered, because now the leading divergence is only logarithmic at most.

In the LRTH model, the left-right symmetry is chosen as the discrete symmetry. Additional Higgs scalars are introduced into the model, as well as several heavy particles, such as heavy gauge bosons, heavy top quark, which lead to rich collider phenomenology.

Higgs as a Pseudo-Goldstone Boson

Consider a complex Higgs field H that resides in the fundamental representation of a global $U(4)$, with a scalar potential of the form

$$V = \mu^2 H^\dagger H + \lambda (H^\dagger H)^2. \tag{1.49}$$

To embed the SM gauge structure, the $SU(2)_L \times SU(2)_R \times U(1)_{B-L}$ subgroup is gauged. To make clear the gauge feature, the Higgs field can be expressed as

$$H = \begin{pmatrix} H_L \\ H_R \end{pmatrix}, \tag{1.50}$$

where H_L is the $SU(2)_L$ doublet and H_R is the $SU(2)_R$ one.

Once the global symmetry is spontaneously broken $U(4) \to U(3)$, the Higgs field H would develop a vev

$$\langle H \rangle = \begin{pmatrix} 0 \\ 0 \\ 0 \\ f \end{pmatrix}, \tag{1.51}$$

with $f = \mu/\sqrt{2\lambda}$ and produce 7 massless Goldstone bosons. $\langle H_R \rangle$ breaks the $SU(2)_R \times U(1)_{B-L}$ down to the $U(1)_Y$ of the SM. Three of the seven Goldstone bosons are absorbed into the longitudinal components of the gauge bosons associated with $SU(2)_R$: $W_H^\pm$ and Z_H. The subscript H reflects the fact that these gauge bosons are quite heavy with mass $\sim gf$, where g is the gauge coupling, so as to avoid constraints from electroweak precision measurements. The remaining of the Goldstones from H_L would be identified as the SM Higgs, which is going to break the electroweak symmetry when acquiring a vev.

Left-right Symmetry

The global $U(4)$ symmetry of the Higgs potential is in fact explicitly broken by the gauged subgroup or gauge interactions in the Lagrangian, thus the would-be Goldstone bosons are expected to receive masses proportional to the explicit breaking.

Gauge loops, for example, thus contribute to the Higgs potential quadratically at the leading order

$$\Delta V = \frac{9 g_L^2 \Lambda^2}{64\pi^2} H_L^\dagger H_L + \frac{9 g_R^2 \Lambda^2}{64\pi^2} H_R^\dagger H_R + \cdots , \tag{1.52}$$

where the $g_{L/R}$ are the gauge couplings for the left and right $SU(2)$ gauge group and Λ is the cutoff of the theory.

Upon imposing a parity symmetry which equates $g_L = g_R \equiv g$, the correction to the Higgs potential becomes

$$\Delta V = \frac{9 g_L^2 \Lambda^2}{64\pi^2} H^\dagger H + \cdots . \tag{1.53}$$

The quadratic piece now respects the global $U(4)$, thus will not contribute to the would-be Goldstone boson masses. The leading order divergence in the mass is then logarithmic at most. The mirror symmetry [54] could take the role of the parity here, however it would leads to an additional complete mirror copy of the SM particles. The left-right symmetry [55] does a better job, introducing a minimum set of new particles.

The fermions in the model are also made left-right symmetric:

$$\begin{aligned} Q_L &= (u,d)_L, \qquad & L_L &= (\nu,e)_L, \\ Q_R &= (u,d)_R, \qquad & L_R &= (\nu,e)_R. \end{aligned} \tag{1.54}$$

The up/down type Yukawa interactions arise from the non-renormalizable terms

$$\begin{aligned} &\frac{\bar{Q}_L H_R H_L^\dagger Q_L + \bar{L}_R H_R H_L^\dagger L_L}{\Lambda} + h.c., \\ &\frac{\bar{Q}_R H_R^\dagger H_L Q_L}{\Lambda} + h.c., \end{aligned} \tag{1.55}$$

that reduce to the SM Yukawa interaction when H_R acquires a vev. In particular, small Dirac mass terms can be generated for the neutrino. It is also possible to include large Majorana mass terms for ν_R, which renders small neutrino mass via seesaw mechanism.

To obtain large Yukawa coupling for the top quark, added into the model are new vector-like quarks T_L and T_R that transform as $[1,1,4/3]$ and $[1,1,4/3]$ under $SU(2)_L \times SU(2)_R \times U(1)_{B-L}$:

$$(y\bar{Q}_R H_R^\dagger T_L + y\bar{Q}_L H_L^\dagger T_R + M\bar{T}_L T_R) + h.c.. \tag{1.56}$$

The right-handed SM top quark is a mixture of the up-type in Q_R and T_R, The mass eigenstates in the top sector is a light SM top plus a heavy top t_H.

The idea of the Higgs as a pseudo-Goldstone boson and the left-right symmetry work well, except that it is necessary to have large mass for $SU(2)_R$ gauge bosons to avoid the electroweak precision bounds, requiring f higher than ~ 2 TeV [56], which tends to have a fair amount of fine-tuning re-introduced by the contribution from the top sector. The solution is to add another Higgs field $\hat{H} = (\hat{H}_L, \hat{H}_R)$ exactly like H, except that it couples only to the gauge sector, but not to the fermions, in particular not to the top quark. Otherwise the heavy top obtains a mass $\sim y\hat{f}$ around a few TeV, which contributes excessively to the loop correction to the Higgs mass due to the large Yukawa coupling of top, thus in turn increase the level of fine-tuning. A matter parity is imposed to ensure the absence of coupling from $\hat{H}$ to matter fields. It is then possible to have the vev $\hat{f}$ of $\hat{H}$ around a few TeV in order for large $SU(2)_R$ gauge boson masses, while keeping f around a few hundred GeV.

The Heavy Top Quark

As mentioned earlier, to account for the $O(1)$ top Yukawa coupling and a top mass around the weak scale, a pair of vector-like quarks are introduced as in Eq.(1.56). Once the Higgs field $H = (H_L, H_R)$ develops a vev, a light SM top quark and a heavy top quark emerge, with masses

$$m_t^2 \sim y^2 f^2 \sin^2 x - M^2 \sin^2 x \sim (\frac{yv}{\sqrt{2}})^2, \tag{1.57}$$

$$m_{t_H}^2 = y^2 f^2 + M^2 - m_t^2, \tag{1.58}$$

where M controls the mixing between the light and heavy top quarks.

Direct search for the heavy top quark t_H at the Large Hadron Collider (LHC) might provide evidence for the twin Higgs mechanism and discrimination from the little Higgs models. At the LHC, the heavy top quark could be produced via single production or pair production process. Due to the large mass of t_H, the phase space for the pair production is severely limited.

The s–channel with resonances W/W_H dominates the single production, as compared to the t–channel W/W_H exchange process. Once the heavy top quark is produced, it primarily decays into $\phi^+ + b$, followed by ϕ^+ decay into the SM final states: $pp \to T\bar{b} \to \phi^+ b\bar{b}$ with $\phi^+ \to tb \to l^+ \nu bb$. The signal to look for at the LHC is then l + 4 b-jets + $\not{E}_T$. The heavy top quark production differs from the SM backgrounds with the same final states (such as $t\bar{t}$ and QCD W + 4 jets) in that the b-jet associated with the single heavy top quark production is very energetic. Furthermore, b-tagging might also help reducing the SM backgrounds.

1.3 Outline

The rest of the thesis is organized as follows.

Chapter 2 presents comprehensive case studies of direct search for new physics at the LHC. In Sect. 2.1, we first outline the IDM framework and present the investigation of the discovery potential of IDM through dilepton channel, over a variety of phenomenologically motivated regions. We further discuss the supplementary trilepton signature of the IDM at the LHC. In Sect. 2.2, we review the setup of the LRTH model and experimental constraints, followed by a study of the phenomenology, in particular, the heavy top quark partner at the LHC. Part of the results presented in Chapter 2 is published as in Ref. [57, 58].

In Chapter 3, we explore low energy B-physics observables and electroweak precision data in the CMSSM, the mGMSB and the mAMSB mechanism. The framework and parameters of the three scenarios are first introduced in Sect. 3.2, followed by an outline of the precision observables under consideration in Sect. 3.3. χ^2 analysis of the three scenarios is presented in Sect. 3.4. Finally, we discuss future sensitivities of the precision observables in Sect. 3.5. This section is based on the paper published as in Ref. [59].

In Chapter 4, we summarize the the results presented and conclude.

CHAPTER 2

COLLIDER SIGNATURE OF THE BSM PHYSICS

With the Large Hadron Collider (LHC) turned on, the particle physics is entering in to an exciting, unique era. Operating at a center-of-mass energy of 7 - 14 TeV – far beyond the operating energy at Tevatron, the LHC is probing directly the TeV territory, with the potential to reveal new physics beyond the Standard Model (SM).

One of the high hopes for the LHC is to unveil the missing Higgs boson in the SM and the mechanism responsible for the electroweak symmetry breaking (EWSB). There have also been alternative proposals concerning the EWSB to the minimal Higgs mechanism, which are likely to show up at the LHC. Here we focus on two of them: the Inert Doublet Model (IDM) and the Left-right Twin Higgs (LRTH) model. In this chapter, we present the investigation of the collider signatures and the prospects of uncovering these two models at the LHC.

2.1 The Inert Doublet Model at the LHC

The Inert Doublet Model [60] (IDM) is one of the simplest extensions of the Standard Model (SM), yet it is also one of the most versatile. Perhaps the most intriguing of these stems from the recent observation [52] that the fields of this additional scalar doublet can provide a positive contribution to the oblique T parameter [61] sufficient to render a SM Higgs mass of $m_h = 400-600$ GeV consistent with precision data [62]. A host of other potential applications for inert[1] doublets exist as well. These range from explaining the lightness of neutrino masses via a one-loop radiative see-saw

---

[1] The descriptor "inert" is applied to the additional scalar doublet in the IDM in order to indicate that it does not couple to the SM fermions. We will therefore continue to refer to the fields this doublet comprises as "inert" particles, even though these particles are not truly inert in the sense that they have SM gauge interactions.

mechanism [50] to the loop-level induction of electroweak-symmetry breaking [51] to engineering successful grand unification [63]. Furthermore, the model yields a natural dark matter candidate in the form of the lightest inert particle (LIP), whose absolute stability is guaranteed by an unbroken Z_2 symmetry. Studies of the relic abundance of LIP dark matter [64, 65], as well as its prospects for indirect detection via neutrino [66], cosmic-ray positron and antiproton [67], and gamma-ray [68, 69] signatures, and for direct detection [70] have also been performed.

Since the coupling structure of the fields of the additional scalar doublet in the IDM differs from that of typical two-Higgs doublet models (2HDM) in the manner discussed above, the collider phenomenology of the IDM also differs markedly from that of such 2HDM. It is therefore worthwhile to investigate the prospects for detecting the additional fields of the IDM via their decay signatures at the LHC. In this section, we focus on the dilepton/trilepton (plus missing energy) channel, which turns out to be one of the most auspicious channels in terms of its discovery potential. Some preliminary, parton-level studies of this channel have been conducted [71] within one particular region of parameter space. Here, we present a more comprehensive, detector-level analysis in which we investigate a variety of different benchmark regions motivated by dark-matter studies, etc., and assess the prospects for observing $\ell^+\ell^- + \not{E}_T$ and $\ell^+\ell^-\ell^\pm + \not{E}_T$ signal at the LHC in each regime. We note that the results of this analysis, although conducted in the context of the IDM, should also be applicable to other extensions of the SM with similarly-modified scalar sectors, as long as the extra scalars in those extensions have similar decay patterns to those in the IDM.

We begin in Sect. 2.1.1, summarizing the theoretical and experimental constraints to which the model is subject. We outline a set of representative benchmark points which correspond to phenomenologically interesting regions of the parameter space in which all of these constraints are satisfied. In Sect. 2.1.2, we discuss dilepton production in the IDM, as well as the SM backgrounds for $\ell^+\ell^- + \not{E}_T$ at the LHC, and we outline the event-selection criteria we use to differentiate signal events from those produced by these backgrounds and present our numerical results.

In Sect. 2.1.3, we discuss trilepton production in the IDM and outline the event-selection criteria we use to differentiate the trilepton signal from the SM background. We then proceed to present our numerical results and discuss the LHC discovery potential for each of our benchmark scenarios.

2.1.1 Model Constraints and Benchmarks

For pheonomenological purpose, it will be useful to parametrize the model using the alternative parameter set $\{m_h, m_S, \delta_1, \delta_2, \lambda_2, \lambda_L\}$, where $\delta_1 \equiv m_{H^\pm} - m_S$, $\delta_2 \equiv m_A - m_S$, and $\lambda_L \equiv \lambda_3 + \lambda_4 + \lambda_5$. This parametrization is particularly useful in that it characterizes the model in terms of physically significant quantities such as particle masses, mass splittings, and λ_L: the coefficient which controls the trilinear hSS and quartic $hhSS$ couplings.

A variety of considerations, stemming both from theoretical consistency [2] conditions and from experimental bounds, constrain the IDM. Below, we briefly summarize these constraints, which were discussed in detail in Ref. [65].

- **Perturbativity:**

$$\lambda_3^2 + (\lambda_3 + \lambda_4)^2 + \lambda_5^2 < 12\lambda_1^2, \qquad \lambda_2 < 1. \tag{2.1}$$

- **Vacuum stability:**

$$\begin{aligned} &\lambda_1 > 0, && \lambda_2 > 0, \\ &\lambda_3 > -2\sqrt{\lambda_1\lambda_2}, && \lambda_3 + \lambda_4 - |\lambda_5| > -2\sqrt{\lambda_1\lambda_2}. \end{aligned} \tag{2.2}$$

- **Limits from direct collider searches:**

  First of all, the excellent agreement between the experimentally-measured values for Γ_W and Γ_Z obtained from LEP and Tevatron data [72] and the predictions of the SM requires that

$$\begin{aligned} &2m_S + \delta_1 > M_W, && 2m_S + \delta_1 + \delta_2 > M_W, \\ &2m_S + \delta_2 > M_Z, && 2m_S + 2\delta_1 > M_Z, \end{aligned} \tag{2.3}$$

---

[2] Of course, it is in some sense from personal aesthetic point of view.

in order that the decays $W^\pm \to SH^\pm, AH^\pm$ and $Z \to SA, H^+H^-$ are kinematically forbidden.

Second of all, bounds on the invisible decays of the Higgs boson from LEP data [73] also serve to constrain scenarios in which the Higgs is light and $m_h > 2m_S$. In this section, however, we will be primarily concerned with cases in which $m_h > 114$ GeV, for which the bounds from the searches on invisible Higgs decay do not apply.

Third and finally, one can consider limits arising from direct searches for $H^\pm$, A, and S, both at LEP and at the Tevatron [74, 75]. It should first be noted that the standard limits on additional charged and neutral Higgs scalars do not apply, because the standard search channels from which they are derived generally involve the couplings of such scalars to fermions, which are absent in the IDM. On the other hand, bounds derived from the non-observation of $e^+e^- \to \chi_1^0\chi_2^0$ [76] and $e^+e^- \to \chi_1^+\chi_1^-$ [77] decays in supersymmetric models can be used to constrain the IDM parameter space, since $e^+e^- \to SA$ and $e^+e^- \to H^+H^-$ in the IDM lead to similar signals. A detailed analysis of the constraints on $e^+e^- \to SA$ in the IDM based on LEP II searches for $e^+e^- \to \chi_1^0\chi_2^0$ was conducted in Ref. [38], which showed that regions of parameter space with $m_S \leq 80$ GeV and $m_A \leq 100$ GeV for $\delta_2 \geq 8$ GeV had been ruled out. For $\delta_2 \leq 8$ GeV, however, only the LEP I constraint $m_S + m_A > M_Z$ applies. A rough bound of $m_{H^\pm} \geq 70 - 90$ GeV [78] can also be derived from the LEP $e^+e^- \to \chi_1^+\chi_1^-$ limit by making the necessary modifications to account for the difference in cross-section between fermion-pair and scalar-pair production. Taking these considerations into account, we will henceforth restrict our attention to models for which $m_{H^\pm} > 80$ GeV.

- **Electroweak precision constraints:**

  Electroweak precision measurements set limits on contributions from the additional Higgs doublet to the oblique S and T parameters [61]. We consider a given parameter choice to be consistent with electroweak precision constraints as long as the overall values of S and T it yields, once all contributions are taken into account, lie within the 68% C.L. ellipse determined by the LEP Electroweak Working Group [79]. For a light SM Higgs, with $m_h \leq 200$ GeV, the constraint is weak as long as δ_1 and δ_2 are of roughly the same order. For a heavy SM Higgs, a large splitting between $H^\pm$ and S is preferred, and $\delta_1 > \delta_2$.

- **Dark matter relic density:**

  One of the attractive aspects of the Inert Doublet Model is that it can provide a viable WIMP dark matter candidate in the form of a stable, neutral LIP. The model is therefore constrained by experimental limits on the relic density of dark matter in the universe. In what follows, we will assume that the LIP relic density represents the dominant component of $\Omega_{\rm DM}h^2$ and falls within the 3σ range of the dark-matter density of the universe as measured by WMAP [80][3]: $0.085 < \Omega_{\rm DM}h^2 < 0.139$. A detailed examination of the relic density of a CP-even scalar LIP in the IDM was conducted in [65]. It was found that the correct dark-matter relic density could be realized in several distinct regions of parameter space in which all the aforementioned theoretical and experimental constraints were also satisfied. For a light SM Higgs with $m_h \sim 120$ GeV, two scenarios are possible. The first of these involves a light LIP with $m_S \sim 40 - 80$ GeV and mass splittings δ_1 and δ_2 which are sizable, but of the same order. The second involves a heavier dark matter particle with $m_S \geq 400$ GeV and relatively small mass splittings. For a heavy SM Higgs with $m_h \geq 400$ GeV, the regions which the constraints leave open are those in which $m_S \sim 80$ GeV and $\delta_1 > \delta_2$, with both δ_1 and δ_2 relatively large, or $m_S \sim 50 - 75$ GeV, $\delta_2 \leq 8$ GeV with a large δ_1.

In Table 2.1, we define a set of benchmark points, each designed to represent a particular region of the remaining, "habitable" parameter space, with an eye toward its collider phenomenology. We emphasize that each benchmark point in Table 2.1

---

[3] In the event that additional sources contribute to $\Omega_{\rm DM}h^2$, only the upper bound applies.

Benchmark	m_h (GeV)	m_S (GeV)	δ_1 (GeV)	δ_2 (GeV)	λ_L
LH1	150	40	100	100	-0.275
LH2	120	40	70	70	-0.15
LH3	120	82	50	50	-0.20
LH4	120	73	10	50	0.0
LH5	120	79	50	10	-0.18
LH6	130	40	100	70	-0.18
LH7	117	37	70	100	-0.14
LH8	120	78	70	35	-0.18
HH1	500	76	250	100	0.0
HH2	500	76	225	70	0.0
HH3	500	76	200	30	0.0

Table 2.1: A list of benchmark points used in our analysis, defined in terms of the model parameters $\{m_h, m_S, \delta_1, \delta_2, \lambda_L\}$. Dark matter relic density and collider phenomenology of the IDM depend little on λ_2, which is set to 0.1 for all benchmark points. The points LH1 − LH8 involve a light (120 GeV $\leq m_h \leq$ 150 GeV) Higgs boson, while the points HH1 − HH3 involve a heavy ($m_h = 500$ GeV) Higgs.

is consistent with all of the applicable constraints detailed above, and that each yields an LIP relic density that falls within the WMAP 3σ range for $\Omega_{\mathrm{DM}}h^2$.

The first regime of interest involves a light SM Higgs with $m_h < 200$ GeV. For such Higgs masses, as discussed above, the electroweak precision constraints are not terribly stringent, and a wide variety of possible particle spectra are permissible. We have included five different benchmark points in our analysis which correspond to this regime (labeled LH1−LH5 for "light Higgs"), the properties of which are listed in Table 2.1. These points are representative of the set of possible scenarios which differ qualitatively from the perspective of a dilepton-channel analysis at the LHC. The points LH1 and LH2 both represent cases in which the LIP is light ($\sim$ 40 GeV) and δ_1 and δ_2 are large and of the same order. However, for the point LH1, $\delta_1 > M_W$ and $\delta_2 > M_Z$, meaning that both $H^\pm$ and A can decay on shell (to $SW^\pm$ and SZ, respectively), whereas for LH2, $\delta_1 < M_W$ and $\delta_2 < M_Z$, so only three-body decay is kinematically accessible. A slightly larger Higgs mass $m_h = 150$ GeV is mandated in LH1 by perturbativity constraints. However, the collider phenomenology of S, A

and $H^{\pm}$ — at least as far as the dilepton channel is concerned — does not depend significantly on the value of m_h, as will soon be made apparent.

Points LH3−LH5 all correspond to situations in which $m_S \sim 80$ GeV, but each represents a different relationship between δ_1 and δ_2. The point LH3 represents a situation similar to that embodied by LH2, in which δ_1 and δ_2 are on the same order and on-shell decays to SA and $SW^{\pm}$ are inaccessible. Larger values of $\delta_{1,2} > M_{W,Z}$ are disfavored by the aforementioned battery of constraints. The point LH4 represents the case of intermediate δ_2 and small δ_1, while the point LH5 represents the opposite situation, in which δ_1 is of intermediate size and δ_2 is small. It is also possible to realize a situation similar to that of LH4, but with $\delta_2 > M_Z$ and hence on-shell A decay. The dilepton-channel analysis in this case would be similar to that in LH1 and HH1. Another possibility would be a point similar to LH5, but with $\delta_1 > M_W$, so that on-shell $H^{\pm}$ decays would be allowed. However, as will be explained in more detail below, the dilepton-signal contribution from H^+H^- decay is hard to disentangle from the SM W^+W^- background. Consequently, varying δ_1 has little effect on the observability of the dilepton signal via SA associated production, by far the most useful production process for discovery at the LHC.

The second regime of interest involves a heavy SM Higgs with $m_h \geq 400$ GeV. A large splitting between $H^{\pm}$ and S is required to satisfy the constraints from electroweak precision measurements in this case. Broadly speaking, these constraints, taken in tandem with relic-abundance considerations, prefer δ_1 to be quite large (and generally much larger than δ_2) and the LIP mass to lie within the range $m_S \approx 70 - 80$ GeV [65]. This parameter-space regime is represented by the benchmark points HH1−HH3 (where "HH" stands for "Heavy Higgs") in Table 2.1. The point labeled HH1 represents the case in which $\delta_2 > M_Z$ and A decays proceed via an on-shell Z intermediary, while the point HH2 represents the case in which $\delta_2 < M_Z$, and the decay $A \to SZ$ is kinematically inaccessible. HH3 is similar to HH2, but has a small $\delta_2 = 30$ GeV. Since precision constraints generally dictate that $m_H^{\pm} > m_A > m_S$ if S is to be the LIP, these three cases encapsulate the only qualitatively different possibilities in this regime from the perspective of dilepton-channel analysis. It is worth noting that another region of parameter space does exist in which all the aforementioned constraints are satisfied: one in which 50 GeV $\leq m_S \leq$ 75 GeV and the mass splitting δ_2 is very small ($\delta_2 \leq$ 8 GeV). However, a dilepton signal tends to be exceedingly difficult to observe in scenarios of this sort, due to the softness of the jets and leptons in the final states. For this reason, we do not include a representative benchmark point for this region in the present study.

For the other allowed region of parameter space — that in which $m_S \geq$ 400 GeV and the mass splittings δ_1 and δ_2 are relatively small — no benchmark points have been included in this study. This is because a scenario of this sort does not yield a detectable signal in the dilepton channel. One reason for this is that the pair-production cross-sections for the inert scalars are highly suppressed due to their heavy masses. Another is that the jets and leptons produced during $H^\pm$ and A decays will be quite soft, owing to the small size of the mass splittings. Therefore, although it remains a phenomenologically viable scenario, we will not discuss this possibility further in this chapter.

2.1.2 Dilepton Signature at the LHC

Signals, Backgrounds, and Event Selection

Let us now turn to examine the signal and background processes relevant to an analysis of the dilepton channel in the IDM at the LHC. The inert scalars $H^\pm$, A, and S can be pair-produced directly at the LHC by Drell-Yan processes involving virtual photons and $W^\pm, Z$ bosons:

$$\begin{aligned} q\bar{q} &\to Z \to AS, & q\bar{q} &\to Z/\gamma^* \to H^+H^-, \\ q\bar{q}' &\to W^\pm \to AH^\pm, & q\bar{q}' &\to W^\pm \to SH^\pm. \end{aligned} \tag{2.4}$$

In Table 2.2, we listed the production cross-sections for SA, H^+H^-, $SH^\pm$, and $AH^\pm$ at the LHC for the various benchmark points defined in Table 2.1. Once so produced, the unstable $H^\pm$ and A bosons further decay to lighter states plus $W^{(*)}$

Benchmark	σ_{SA} (fb)	$\sigma_{H^+H^-}$ (fb)	$\sigma_{SH^\pm}$ (fb)	$\sigma_{AH^\pm}$ (fb)
LH1	289.2	69.8	503.3	125.2
LH2	628.8	163.6	1055.1	299.0
LH3	179.9	86.0	319.0	154.9
LH4	248.9	440.2	1050.3	370.1
LH5	465.5	93.3	352.9	302.3
HH1	91.8	2.9	25.4	13.5
HH2	152.0	4.0	33.0	20.5
HH3	336.7	5.6	43.7	35.2

Table 2.2: Leading-order cross-sections for the associated production of SA, H^+H^-, $SH^\pm$, and $AH^\pm$ at the LHC, with center-of-mass energy $\sqrt{s} = 14$ TeV, for the various benchmark points defined in Table 2.1.

or $Z^{(*)}$. Depending on how $H^\pm$ and A decay, a number of final states are possible. Each of these states, as required by matter parity, includes precisely two LIPs, as well as a number of jets, charged leptons, and neutrinos.

The presence of sizable QCD backgrounds for final states involving one or more jets renders such states difficult to use for discovery; final states involving charged leptons alone, on the other hand, have far smaller SM backgrounds and hence are far more auspicious in terms of their LHC discovery potential. A single lepton plus missing E_T signal would be difficult to resolve, due to the huge SM W background, but a variety of multi-lepton signatures initiated by the electroweak processes enumerated above may be observable at the LHC. The trilepton + $\not{E}_T$ channel, for example, which is of crucial importance for supersymmetry searches [81], can potentially also be important in searching for an additional, inert scalar doublet. In this section, we will focus on dilepton channel, which seems to offer the brightest prospects for discovery.

The dominant signal contribution to $\ell^+\ell^-+\not{E}_T$ in the IDM, where $\ell = \{e, \mu\}$, results from either $pp \to SA$ with $A \to S\ell^+\ell^-$, or $pp \to H^+H^-$, with $H^\pm \to S\ell^\pm\nu$, depending on the choice of parameters. These processes are depicted diagrammatically in panels (a) and (b) of Fig. 2.1, respectively. Other processes that result in $\ell^+\ell^-+\not{E}_T$

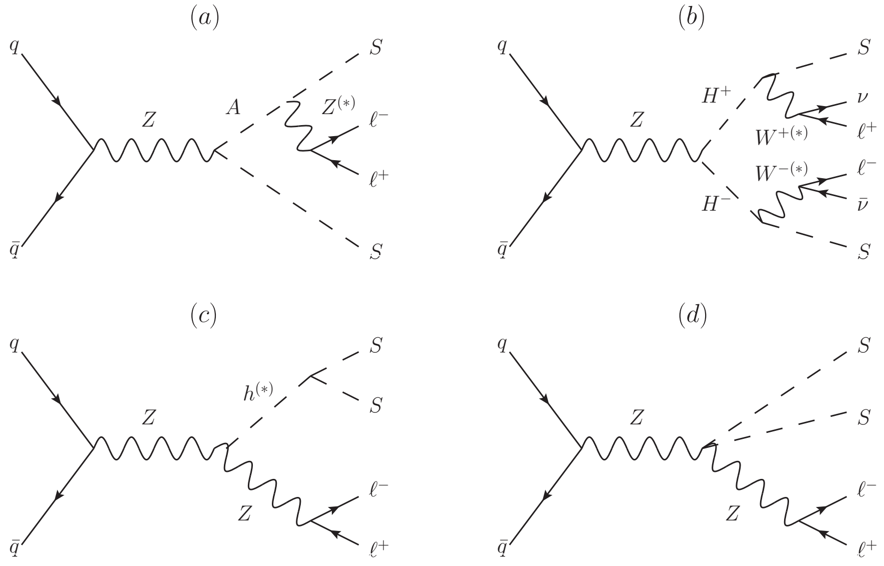

Figure 2.1: Diagrams corresponding to the contributions to the $pp \to \ell^+\ell^-\not{E}_T$ in the IDM discussed in the text.

final states, e.g. $pp \to H^+H^-$ with $H^+ \to S\ell^+\nu$ and $H^- \to A\ell^-\bar{\nu} \to S\ell^-\bar{\nu}\nu\bar{\nu}$, generally contribute only a small amount to the signal cross-section and can therefore be safely ignored. Another contribution comes from processes in which a leptonically-decaying pseudoscalar A is produced in association with some other particle or particles which decay to jets or charged leptons too soft to register in the detector. In general, the event rates for such processes (the most important of which is $pp \to H^\pm A \to \ell^+\ell^- jj + \not{E}_T$) are also small compared to that for $pp \to SA \to \ell^+\ell^- + \not{E}_T$. However, if δ_1 is small (as it is in benchmark LH4), a substantial fraction of the jets and charged leptons from $H^\pm$ decays will be sufficiently soft that such processes do yield a considerable contribution and therefore need to be accounted for in the analysis.

In addition to the pair-production processes discussed above, the electroweak Higgs-associated-production process

$$q\bar{q} \to hZ \tag{2.5}$$

can also result in a $\ell^+\ell^- + \not{E}_T$ final state in the manner illustrated in panel (c) of

Fig. 2.1, as long as the decay $h \to SS$ is permitted. The dilepton-channel contribution from this process is significant only in cases in which λ_L is nonzero and $m_h > 2m_S$ — the conditions under which h can decay on-shell to a pair of LIPs. Of the eight benchmark scenarios defined in Table. 2.1, these conditions are satisfied only in scenarios LH1 and LH2, for which $\sigma_{hZ} \times \text{Br}(h \to SS) = 343.12$ fb and 706.65 fb, respectively. As these rates are roughly on the same order as those for $pp \to SA$ production, it will be necessary to take this contribution into account in the ensuing analysis.

A further contribution to the $\ell^+\ell^-\not{E}_T$ production cross-section in the IDM results from $pp \to SSZ$ production via the four-point $SSZZ$ interaction shown in panel (d) of Fig. 2.1. However, this contribution is quite small in comparison with that from SA pair production, as the former is a three-body process while the latter is only two-body. Interference effects between the diagrams depicted in panels (a), (c), and (d) of Fig. 2.1 are consequently tiny as well, and can be safely neglected.

In what follows, we will focus on $pp \to SA \to \ell^+\ell^-SS$ as our signal process, and treat $pp \to H^+H^- \to \ell^+\ell^-\nu\bar{\nu}SS$ as part of the background. The reason for this is twofold. First, since the constraints in Sect. 2.1.1 (and especially those from WMAP and electroweak precision data) typically prefer situations in which $2m_{H^+} \geq m_A + m_S$, production cross-sections for $pp \to H^+H^-$ tend to be lower than those for $pp \to SA$. Second, a $pp \to H^+H^- \to \ell^+\ell^- + \not{E}_T$ signal turns out to be far more difficult to distinguish from the dominant SM backgrounds (discussed in detail below) on the basis of event topology. We will also treat $pp \to hZ \to SS\ell^+\ell^-$ and $pp \to SSZ \to SS\ell^+\ell^-$ as a contribution to the background, because the event topologies generally differ from those associated with $pp \to SA \to \ell^+\ell^-SS$.

The SM backgrounds relevant for the $\ell^+\ell^- + \not{E}_T$ channel are well-known from studies of the supersymmetric process $pp \to \chi_1^0\chi_2^0 \to \ell^+\ell^- + \not{E}_T$, where χ_1^0 and χ_2^0 are the lightest and next-to-lightest neutralinos. These include irreducible backgrounds from WW and ZZ/γ^* production (with the contribution from off-shell photons [82] properly taken into account), as well as reducible backgrounds from $t\bar{t}$, WZ/γ^*, Wt, and $Zb\bar{b}$ processes; $WW + n$ jets and $ZZ + n$ jets; and Drell-Yan production of $\tau^+\tau^-$

pairs.

In the present analysis, events were generated at parton-level, both for the signal process and for the backgrounds discussed above, in MadGraph [83] and then passed through PYTHIA [84] for parton showering and hadronization. Events were then passed through PGS4 [85] to simulate the effects of a realistic detector. Subsequent to event generation, in order to distinguish signal events from those associated with these backgrounds and to account for the performance thresholds of the LHC detectors, we impose three sets of cuts in our analysis. The first such set, henceforth referred to as our Level I cuts, is designed to mimic a realistic detector acceptance:

- Exactly two electrons or muons with opposite charge.
- $p_T^\ell \geq 15$ GeV and $|\eta_\ell| \leq 2.5$ for each of these charged leptons.
- For lepton isolation, we require $\Delta R_{\ell\ell} \geq 0.4$ for the charged-lepton pair, and $\Delta R_{\ell j} \geq 0.4$ for each combination of one jet and one charged lepton.

It should be noted that for $\ell = \{e, \mu\}$, the above lepton p_T^ℓ cut is sufficient to meet the Level I triggering requirements for both ATLAS [86] and CMS [87].

The subsequent two sets of selection criteria we impose are designed to discriminate efficiently between signal and background events. Our Level II cuts are aimed at suppressing reducible backgrounds from processes such as $t\bar{t}$, WZ/γ^*, Wt, and $Zb\bar{b}$, which tend to involve either hard jets, little missing transverse energy, or both. We impose a veto on all events manifesting high-p_T jet activity within the central region of the detector, as well as a minimum missing transverse energy cut:

- No jets with $p_T^j > 20$ GeV and pseudorapidity within the range $|\eta_j| < 3.0$.
- $\not{E}_T > 30$ GeV.

The efficacy of this latter missing E_T cut should not be overemphasized: while each signal event necessarily includes a pair of LIPs, these particles tend to be produced back-to-back. As a result, their contributions to the overall $\not{E}_T$ tend to cancel each other out, to the end that the $\not{E}_T$ distributions for signal events tend not to differ radically from those for processes like ZZ/γ^*, WW, and $t\bar{t}$ which involve energetic neutrinos. Nevertheless, this $\not{E}_T$ cut is highly efficient in eliminating background contributions from $Zb\bar{b}$ and WZ/γ^* events (with the W decaying hadronically) with jets soft enough so as to survive the central-jet veto.

After imposing Level I and II cuts, contributions from $Zb\bar{b}$ and Drell-Yan production of leptonically-decaying $\tau^+\tau^-$ pair, are effectively eliminated. The dominant remaining backgrounds are the irreducible ones from WW and ZZ/γ^* events, as well as residual $t\bar{t}$, WZ/γ^* and Wt events which survive the Level II cuts. In Table 2.3, we list the signal cross-sections for $pp \to SA \to \ell^+\ell^-\not{E}_T$ at the LHC for each of the benchmark points presented in Table 2.1, after the application of the Level I and Level II cuts discussed in the previous section. We also show the effect that these cuts have on the cross-sections for those background processes, both reducible and irreducible, which remain at non-negligible levels after the Level II cuts have been applied: WW, ZZ/γ^*, $t\bar{t}$, WZ/γ^*, and Wt. Results for $pp \to H^+H^- \to \ell^+\ell^-\not{E}_T$ and $pp \to h^{(*)}Z \to SS\ell^+\ell^-$, also treated as background processes in this analysis, are shown here as well. It is evident from the data presented in Table 2.3 that the application of the Level I+II cuts results in a substantial reduction of the reducible backgrounds from $t\bar{t}$, WZ/γ^*, and Wt. However, as efficient as these cuts are, the rates for these background processes (and especially from $t\bar{t}$) are large enough that a substantial number of events still survive them. Consequently, these reducible backgrounds cannot be neglected in the final analysis.

In order to differentiate the $pp \to SA$ signal from these remaining backgrounds, it is necessary to impose a third level of event-selection criteria based largely on event topology, whose thresholds can be adjusted to optimize significance of discovery in any given benchmark scenario. For the benchmark points included in our survey, the optimal pattern of Level III cuts generally falls into one of two categories, depending primarily on whether or not the decay of $A \to SZ^{(*)}$ occurs on shell.

In all of our benchmark scenarios in which $\delta_2 > M_Z$, the CP-odd scalar A decays essentially 100% of the time to an LIP and an on-shell Z; thus the distribution of the invariant mass $M_{\ell\ell}$ of the charged-lepton pair in such scenarios tends to peak sharply

	Level I Cuts			Level I+II Cuts		
Benchmarks	σ_{SA}(fb)	$\sigma_{H^+H^-}$(fb)	σ_{hZ}(fb)	σ_{SA}(fb)	$\sigma_{H^+H^-}$(fb)	σ_{hZ}(fb)
LH1	9.61	0.82	2.90	6.03	0.46	1.79
LH2	10.28	1.06	5.75	6.53	0.51	3.47
LH3	2.32	0.34	0.01	1.47	0.13	0.01
LH4	3.84	0.19	0	2.07	0.02	0
LH5	0.38	~ 0	0.01	~ 0	0.14	0.01
HH1	3.23	0.02	0	1.97	0.01	0
HH2	3.01	0.03	0	1.81	0.01	0
HH3	1.69	0.02	0	1.09	0.01	0
SM Backgrounds	σ_{BG}(fb)			σ_{BG}(fb)		
WW	621.44			316.97		
ZZ/γ^*	132.09			76.46		
$t\bar{t}$	4531.51			58.87		
WZ/γ^*	113.97			51.85		
Wt	709.14			52.11		
Total SM	6108.15			556.26		

Table 2.3: Leading-order cross-sections for the signal processes $pp \to SA \to \ell^+\ell^- \not{E}_T$ at the LHC with $\sqrt{s} = 14$ TeV after Level I and II cuts for each of the benchmark points presented in Table 2.1. Also shown are the backgrounds $pp \to H^+H^- \to \ell^+\ell^- \not{E}_T$, $pp \to h^{(*)}Z \to \ell^+\ell^- \not{E}_T$, WW, ZZ/γ^*, $t\bar{t}$, WZ/γ^*, Wt after Level I+II cuts, as well as a total background cross-section.

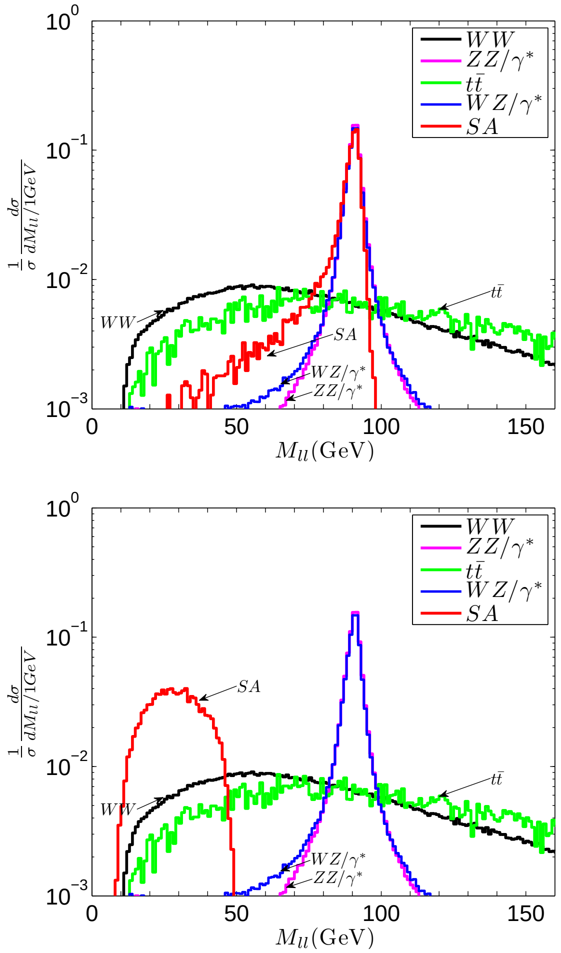

Figure 2.2: Dilepton-invariant-mass distributions for the benchmark points LH1 (top panel) and LH3 (bottom panel) both for the signal process and for the most relevant SM backgrounds.

around M_Z. This is the case for points LH1 and HH1, the $M_{\ell\ell}$ distribution for the former of which is shown in the top panel of Fig. 2.2. It is therefore advantageous to select events on the basis of whether or not $M_{\ell\ell}$ falls within a window

- $M_{\ell\ell}^{\text{min}} \leq M_{\ell\ell} \leq M_{\ell\ell}^{\text{max}}$,

where the parameters $M_{\ell\ell}^{\text{min}}$ and $M_{\ell\ell}^{\text{max}}$ are to be adjusted to optimize the statistical significance of discovery for each benchmark point. In cases of this sort, the best results are generally obtained by imposing a window around 20 GeV wide, centered near M_Z. Such a cut efficiently reduces the W^+W^-, $Z\gamma^*$, $W\gamma^*$, $t\bar{t}$ and Wt backgrounds, leaving the ZZ and WZ backgrounds (which are little affected by such a cut) as the dominant ones.

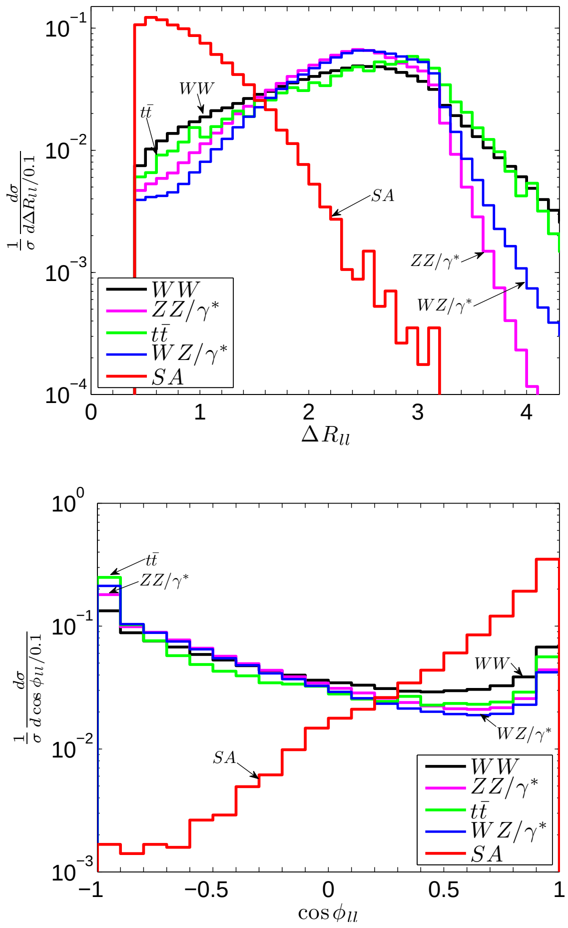

Figure 2.3: Distributions of the angular separation variables $\Delta R_{\ell\ell}$ (top panel) and $\cos\phi_{\ell\ell}$ (bottom panel) for benchmark point LH3, in which decays of the pseudoscalar A occur via an off-shell Z. These distributions justify the imposition of the minimum $\cos\phi_{\ell\ell}$ and maximum $\Delta R_{\ell\ell}$ cuts described in the text.

In cases where $\delta_2 < M_Z$ (LH2−LH5, HH2−HH3), the two body decay $A \to SZ$ is kinematically inaccessible. Likewise, the decay channel $A \to H^\pm W^\mp$ is not open unless $\delta_2 > \delta_1 + M_W$ — a condition which is difficult to realize, given the constraints on the model, and which is not satisfied for any of the benchmark points in our study. When these decays are unavailable, the dominant leptonic decay channel for the A involves the three-body process $A \to S\ell^+\ell^-$, which proceeds through an off-shell Z. As a result, the dilepton invariant mass distribution is peaked well below M_Z, around the value of δ_2, as shown in the bottom panel of Fig. 2.2 for benchmark point LH3. In cases of this sort, imposing an upper limit $M_{\ell\ell}^{\max} \sim \delta_2$ on the dilepton invariant mass can assist in improving the signal-to-background ratio. A cut of this sort can effectively suppress the ZZ and WZ backgrounds, the $M_{\ell\ell}$ distributions for which are peaked sharply around M_Z.

To further suppress the Standard-Model WW, $Z\gamma^*$, $W\gamma^*$, Wt, and $t\bar{t}$ backgrounds in cases in which $\delta_2 < M_Z$, it is useful to select events on the basis of observables related to the angular separation between charged leptons. The ℓ^+ and ℓ^- produced by these SM background processes are typically energetic and well-separated from one another. On the other hand, those resulting from A decay via an off-shell Z tend to be soft, with small (and extremely so, if δ_2 is quite small) angular separation. This difference in event topology is readily apparent from Fig. 2.3, which displays the $\Delta R_{\ell\ell}$ (top panel) and $\cos\phi_{\ell\ell} \equiv \cos(\phi_{\ell^+} - \phi_{\ell^-})$ (bottom panel) distributions for benchmark LH3. It is therefore useful, in cases in which $\delta_2 < M_Z$, to impose the additional cuts

- $\Delta R_{\ell\ell} \leq \Delta R_{\ell\ell}^{\max}$,
- $\cos\phi_{\ell\ell} \geq \cos\phi_{\ell\ell}^{\min}$,

where $\Delta R^{\max}$ and $\cos\phi_{\ell\ell}^{\min}$ are to be optimized for each benchmark point.

In certain situations, the imposition of additional event-selection criteria can also be helpful in distinguishing signal from background events. For example, it can also be advantageous to impose a minimum cut on the total transverse momentum variable

$$H_T \equiv \not{p}_T + \sum_i p_T^{\ell_i}, \tag{2.6}$$

which can serve as an efficient discriminant in both the $\delta_2 > M_Z$ and $\delta_2 < M_Z$ cases:

- $H_T \geq H_T^{\min}$.

Benchmark	$M_{\ell\ell}^{\rm min}$ (GeV)	$M_{\ell\ell}^{\rm max}$ (GeV)	$\Delta R_{\ell\ell}^{\rm max}$	$\cos\phi_{\ell\ell}^{\rm min}$	$H_T^{\rm min}$ (GeV)	$\not{E}_T^{\rm min}$ (GeV)	$p_{T\ell}^{\rm max}$ (GeV)
LH1	80	100	–	–	150	50	–
LH2	–	70	1.2	0.7	200	100	–
LH3	20	50	0.8	0.7	200	90	–
LH4	20	50	0.8	0.7	200	90	–
LH5	–	10	0.6	0.9	–	30	25
HH1	80	100	2.0	–	200	80	–
HH2	20	70	1.2	0.7	200	90	
HH3	–	25	–	–	–	30	–

Table 2.4: A list of the optimized Level III cuts used in the analysis of each of the benchmark points presented in Table 2.1. An entry of "–" indicates that the corresponding cut is not imposed. Note that a $\not{E}_T^{\rm min}$ cut of 30 GeV has been applied in each of these scenarios as a part of the Level II cuts, but that this threshold has been raised for several of the points at Level III. For more details on the definition of the thresholds used, see text.

Again, the threshold $H_T^{\rm min}$ can be optimized to suit a given benchmark point. This cut can be helpful in reducing the WW and $Z\gamma^*$ backgrounds, but is less so in reducing the contribution from $t\bar{t}$. In addition, it can sometimes also be useful to tighten the minimum $\not{E}_T$ cut applied during the Level II cuts. Therefore, at Level III, we allow for the imposition of an additional missing-transverse-energy cut

- $\not{E}_T \geq \not{E}_T^{\rm min}$.

Furthermore, in cases in which δ_2 is small and the charged leptons associated with the signal process far less energetic than those associated with the SM backgrounds, it can be useful to impose a ceiling $p_{T\ell}^{\rm max}$ on the p_T of each charged lepton, as we do here for benchmark point LH5.

- $p_{T\ell} \leq p_{T\ell}^{\rm max}$.

In Table 2.4, we list the Level III cuts applied in each of the benchmark scenarios listed in Table 2.1. The precise numbers appearing in this table have been selected in order to maximize the $S/\sqrt{B}$ ratio for each individual benchmark point. It should be noted that the particular set of cuts applied in each case indeed depends primarily on the relationship between δ_2 and M_Z.

Results

Now that we have discussed in detail the event-selection procedure to be used in our numerical analysis of dilepton signals in the IDM, we next present the results of that numerical analysis. In Table 2.5, we list the cross-sections for the signal process and the most relevant backgrounds after the application of our Level I+II+III cuts. The last two rows in the Table display the signal-to-background ratio S/B and the statistical significance (as given by $S/\sqrt{B}$ at an integrated luminosity of $\mathcal{L} = 100$ fb^{-1}) for each benchmark point[4] in our analysis, after the implementation of these same cuts. Note that the numbers quoted here for benchmark LH4 with small δ_1 include, in addition to the usual $pp \to SA \to \ell^+\ell^- + \not{E}_T$ contribution, contributions from the processes $pp \to H^\pm A \to \ell^+\ell^- jj + \not{E}_T$ and $pp \to H^\pm A \to \ell^+\ell^-\ell^\pm + \not{E}_T$ in which the additional jets or leptons from $H^\pm$ decay are sufficiently soft as to escape detection. It should be noted that taking these contributions into account results in an increase in the statistical significance of discovery in this channel from 2.07σ to 3.29σ. For the other benchmark points listed in Table 2.1, $\delta_1 \geq 50$ GeV, and consequently the contribution from $pp \to H^\pm A$ processes with soft jets or leptons will be negligible.

Let us now turn to examine the results for each of the individual benchmark scenarios in our study in more detail. We begin with the LH1, which involves a light Higgs boson, a light LIP ($m_S \sim 40$ GeV), and a large mass splitting ($\delta_2 = 100$ GeV $> M_Z$). The dominant backgrounds in this scenario are those from ZZ and WZ, each of which also involves the leptonic decay of an on-shell Z and is therefore difficult to differentiate from the signal process on the basis of kinematical variables. The remaining backgrounds are efficiently suppressed after the imposition of the $M_{\ell\ell}$

---

[4] One modification is made in the case of LH5. For this point, both signal and background event rates are quite low, and consequently the significance value quoted in the last column of Table 2.5 was obtained using Poisson statistics rather than $S/\sqrt{B}$.

	LH1	LH2	LH3	LH4	LH5	HH1	HH2	HH3
σ_{SA}	3.42	0.89	0.18	0.19	0.004	0.65	0.37	1.01
$\sigma_{H^+H^-}$	0.04	~ 0	~ 0	~ 0	~ 0	~ 0	0.01	~ 0
σ_{hZ}	1.28	0.01	~ 0	0	~ 0	0	0	0
σ_{WW}	11.59	0.07	0.03	0.03	0.13	0.45	0.08	17.49
σ_{ZZ/γ^*}	36.99	0.24	0.15	0.15	0.04	13.41	0.26	1.06
$\sigma_{t\bar{t}}$	4.55	0.11	0.05	0.05	~ 0	0.55	0.12	1.60
σ_{WZ/γ^*}	19.52	0.08	0.04	0.04	0.04	5.85	0.09	0.76
σ_{Wt}	3.82	0.07	0.06	0.06	0.01	0.45	0.12	1.65
$\sigma_{\mathrm{BG}}^{\mathrm{comb}}$	77.79	0.58	0.34	0.34	0.23	20.71	0.67	22.56
S/B	0.04	1.53	0.52	0.57	0.02	0.03	0.56	0.04
$S/\sqrt{B}$	3.87	11.66	3.04	3.29	0.02	1.42	4.55	2.12

Table 2.5: Cross-sections for the processes $pp \to SA \to \ell^+\ell^-\not{E}_T$, $pp \to H^+H^- \to \ell^+\ell^-\not{E}_T$, and $pp \to h^{(*)}Z \to \ell^+\ell^-\not{E}_T$ at the LHC for each of the benchmark points presented in Table 2.1 after the application of our Level III cuts. Cross-sections for the dominant SM backgrounds (WW, ZZ/γ^*, etc.) after the application of the Level III cuts are also shown, as is the total background cross-section including all of these individual contributions. An entry of "$\sim$ 0" indicates a cross-section less than 1 ab. The last two rows display the signal-to-background ratio S/B and statistical significance (as given by $S/\sqrt{B}$) corresponding to an integrated luminosity of $\mathcal{L} = 100$ fb^{-1} after the application of these same cuts.

cut near the M_Z window. With 100 fb^{-1} of integrated luminosity, a significance level of 3.87σ could be obtained in this benchmark scenario. The situation for the heavy-Higgs benchmark HH1 is similar; however the smaller SA-production cross-section in this case (due primarily to an increased LIP mass) translates into a lower statistical significance.

Benchmark point LH2 also includes a 40 GeV dark matter particle, but involves a smaller mass splitting than that of LH1: $\delta_2 = 70$ GeV. This scenario affords the best opportunity for discovery at the LHC out of any of the benchmark points in our analysis, yielding a statistical significance of 11.66σ with 100 fb^{-1} of integrated luminosity. Two factors contribute to its success: a small production threshold $m_S + m_A$, and the fact that $\delta_2 < M_Z$, which implies that the CP-odd scalar A decays via an off-shell Z. The latter consideration makes it possible to eliminate ZZ and WZ background contributions quite efficiently by setting $M_{\ell\ell}^{\max}$ comfortably below the Z pole. Further cuts on the angular variables $\cos\phi_{\ell\ell}$ and $\Delta R_{\ell\ell}$ serve to reduce the remaining backgrounds to a manageable level. After all cuts are imposed, events from the low-$M_{\ell\ell}$ tail of the ZZ distribution form the dominant background. It should be noted, however, that while the aforementioned angular-separation cuts are quite efficient in reducing background events, this efficiency comes with a price: the cuts also eliminate a substantial fraction of signal events. This explains why the signal cross-section for LH2 is less than that for LH1, as no angular separation cuts are imposed in the latter scenario.

Benchmarks LH3 and LH4 are superficially similar, given that they involve a similar LIP mass $m_S \sim 80$ GeV and the same mass splitting $\delta_2 = 50$ GeV. In this case, however, the marked difference in δ_1 — a parameter which generally has little effect on observability of the dilepton signal in the SA associated-production channel — between the two points has a substantial impact on their collider phenomenology. The reason for this is twofold. First of all, since $\delta_2 > \delta_1$ for LH4 (unlike any other benchmark in our analysis), the decay channels $A \to H^\pm W^\mp \to X + \not{E}_T$, where X denotes either four jets, two jets and a single charged lepton, or two charged leptons, are open in this scenario, with a branching ratio BR$(A \to H^\pm W^\mp \to X + \not{E}_T) =$

0.435. As a result, BR($A \rightarrow SZ \rightarrow \ell^+\ell^- + \not{E}_T$), and thus the dilepton signal cross-section, are reduced by an additional factor of two relative to those points for which such competing decays are kinematically prohibited. Second of all, as discussed above, the small value for $\delta_1 = 10$ GeV in LH4 allows the additional contribution of $AH^\pm$ process to the signal due to the unobservable soft jets and leptons from $H^\pm$ decay. These additional contributions augment the overall signal cross-section and more than compensate for the diminished BR($A \rightarrow SZ \rightarrow \ell^+\ell^- + \not{E}_T$), as discussed above. For 100 fb^{-1} of integrated luminosity, a significance level greater than 3σ could be reached for LH4 as well as LH3.

The final light-Higgs scenario in our analysis, LH5, turns out to be the most difficult benchmark point for which to observe a dilepton signal, primarily because of the small mass splitting $\delta_2 = 10$ GeV between S and A. The charged leptons in the final state tend to be extremely soft, and consequently the signal remains buried under the SM background even after an optimized set of Level III cuts is applied. Scenarios with a small value of δ_2 will in general be difficult to discover via this channel at the LHC. It should be noted that the results we obtain for this benchmark differ significantly from the parton-level results quoted in [71] for a similar benchmark scenario, also with $\delta_2 = 10$ GeV. The discrepancy owes primarily to our imposition of a Level I cut of $\Delta R_{\ell\ell} > 0.4$ cut designed to replicate the effect of electron and muon isolation requirements at the ATLAS and CMS detectors. Since the angular separation between the lepton momenta tends to be extremely small for such a small value of δ_2, a vast majority of signal events will have $\Delta R_{\ell\ell} < 0.4$ and hence be eliminated by this cut.

Let us now turn to discuss the benchmark points which feature a heavy ($m_h =$ 500 GeV) Higgs boson — in other words, those benchmarks for which the IDM successfully addresses the LEP paradox. While the electroweak precision constraints discussed in Sect. 2.1.1 are more stringent in this case, these constraints primarily affect δ_1, which is typically required to be quite large. Since this parameter generally does not affect results in the dilepton channel, which depend primarily on m_S and δ_2, the same qualitative results obtained for the light-Higgs benchmarks also apply here.

For HH1, with $\delta_2 = 100$ GeV, a significance level of only 1.42σ can be achieved with 100 fb^{-1} of integrated luminosity, due to both the overwhelming SM backgrounds that exist for dilepton processes involving on-shell Z decay, and a suppressed signal cross-section relative to benchmark LH1 (which has a far lighter LIP). For HH3 — a benchmark with a somewhat small value of δ_2 — a $M_{\ell\ell}^{\max} = 25$ GeV cut helps to cut down the SM backgrounds from processes involving on-shell Z decay. It is, however, hard to improve upon the statistical significance by implementing additional cuts. The remaining background events which survive this cut (most of which come from WW) tend to have similar $\cos\phi_{\ell\ell}$ and $\Delta R_{\ell\ell}$ distributions to those of the signal — a situation which makes the application of further, angular cuts essentially redundant. Furthermore, since the missing-energy distribution for the signal events in scenarios with small δ_2 peaks at relatively low values of $\not{E}_T$, there is little to be gained by increasing $\not{E}_T^{\min}$ much beyond the Level II threshold of 30 GeV. By contrast, in scenarios with larger δ_2, an elevated missing-energy cut works quite effectively in tandem with the angular cuts in reducing backgrounds from WW and $t\bar{t}$. A significance level of 2.32σ is reached for HH3 with 100 fb^{-1} of integrated luminosity.

It is benchmark HH2, however, which affords the best opportunity for discovery at the LHC from among the heavy-Higgs scenarios, with a statistical significance of 4.55σ at 100 fb^{-1} of integrated luminosity. This is because the signal for this benchmark can be distinguished from the WZ and ZZ backgrounds on the basis of $M_{\ell\ell}$ cuts, and from the remaining WW, Wt, and $t\bar{t}$ backgrounds on the basis of $\cos\phi_{\ell\ell}$, $\Delta R_{\ell\ell}$, and $\not{E}_T$ cuts in the same manner as for the low-Higgs-mass point LH2. We therefore conclude that even scenarios in which the IDM permits an evasion of the LEP upper bound on m_h can yield an observable dilepton signal at the LHC.

From the results in Table 2.5, it is evident that the prospects for detecting a signal in the dilepton channel in the IDM model hinge primarily on two criteria. The first of these is the dependence of the cross-section for $q\bar{q} \to SA$ on $m_S + m_A$ and δ_2. This cross-section is, of course, larger in cases where the pair-production threshold energy $m_S + m_A$ is small. Among cases with similar values of $m_S + m_A$, those in which δ_2 is smaller will have larger production cross-sections. This can be understood by noting that the partonic cross-section for this process depends on m_S and δ_2 in the following way:

$$\hat{\sigma}_{q\bar{q}\to SA}(\hat{s}) \;\propto\; [\hat{s}^2 - 2\hat{s}(\delta_2(\delta_2 + 2m_S) + 2m_S^2) + \delta_2^2(\delta_2 + 2m_S)^2]^{3/2}. \tag{2.7}$$

For values of $\hat{s} \sim m_S + m_A$, for which the dependence of this expression on m_S and δ_2 is non-negligible, it is apparent that for fixed $m_S + m_A$, $\hat{\sigma}_{q\bar{q}\to SA}(\hat{s})$ decreases with increasing δ_2. This accounts for the difference between the $pp \to SA$ production cross-sections for benchmarks LH1 and HH3 quoted in Table 2.2.

The second criterion is the relationship between δ_2 and M_Z: cases in which $\delta_2 < M_Z$ tend to have a higher statistical significance than those in which $\delta_2 > M_Z$, as is manifest from comparing the results for benchmarks LH2 and LH1 in Table 2.5. This is because in the latter case, it is difficult to distinguish the signal process from the dominant ZZ background on the basis of event topology. On the other hand, when δ_2 is exceedingly small (as it is in our LH5 scenario), the charged leptons will be so soft that the detector-acceptance (i.e. Level I) cuts will eliminate the vast majority of would-be signal events, as discussed above. Between these extremes, a window of

$$40 \text{ GeV} \leq \delta_2 \leq 80 \text{ GeV} \tag{2.8}$$

emerges within which the prospects for observing a signal are quite good, so long as the LIP mass also falls roughly within the $40 - 80$ GeV range. For cases in which $\delta_2 \geq M_Z$, the prospects for discovery at the LHC are reasonable — meaning a statistical significance around the 3σ level with 100 fb^{-1} of integrated luminosity — only if the dark-matter particle is light ($m_S \sim 40$ GeV).

It is not difficult simultaneously to satisfy the constraints discussed in Sect. 2.1.1 and to realize a δ_2 value within this mass window of $40 - 80$ GeV while keeping the LIP mass relatively light ($m_S \leq 80$ GeV) — or, alternatively, to obtain a large mass splitting $\delta_2 \geq M_Z$ and a light LIP mass of around 40 GeV. This is true not only in models where the Higgs boson is light and the parameters of the theory comparatively unconstrained, but also in cases in which the mechanism of Ref. [52]

for evading electroweak precision bounds on the Higgs mass is realized in nature, and $m_h \sim 500$ GeV. In either case, it would be possible to observe a dilepton signal at the LHC at a significance level of 3σ or higher, with an integrated luminosity of 100 fb^{-1}.

Conclusion

In this section, we have investigated the potential for observing a dilepton signature in the Inert Doublet Model at the LHC. We have explored the prospects for a number of benchmark scenarios, including several in which the IDM successfully ameliorates the LEP paradox and the Higgs-boson mass can be elevated as high as $m_h = 400 - 500$ GeV, as well as several of the dark-matter motivated scenarios cataloged in Ref. [65]. We have shown that for cases in which the dark matter candidate is relatively light $(40 - 80$ GeV$)$ and 40 GeV $\leq \delta_2 \leq$ 80 GeV, a signal with a significance of more than 3σ should be apparent at the LHC with less than 100 fb^{-1} of integrated luminosity. Moreover, in cases when the LIP is on the lighter end of this range, a 3σ discovery would be possible with only 10 fb^{-1} of integrated luminosity. In addition, there are also certain cases in which $\delta_2 > M_Z$ and the LIP is light ($m_S \sim 40$ GeV) for which the prospects for detection are also reasonably good.

Of course the observation of an excess in the $\ell^+\ell^- + \not{E}_T$ channel alone, while exciting, is by no means conclusive evidence for the Inert Doublet Model. Indeed, many models of beyond-the-Standard-Model physics lead to such a signature, including weak-scale supersymmetry, two-Higgs-doublet models, etc. Fortunately, evidence for the IDM can come from a number of other sources. Some of these sources involve other channels associated with the SM-like Higgs at the LHC. One potentially interesting signal could arise due to deviations of the decay properties of the Higgs boson h from those of a SM Higgs. In situations in which $m_h > 2m_S$, for example, $\Gamma(h \to SS)$ can contribute substantially to the invisible Higgs width. Searches for the Weak-Boson Fusion (WBF) process $qq' \to qq'h$, with h decaying invisibly, can be used effectively to identify a Higgs boson at the LHC [88], and preliminary studies [71] indicate that a 5σ discovery should be possible with only 10 fb^{-1} of integrated luminosity in regions of parameter space where $\text{BR}(h \to \text{invisible})$ is large. Moreover, if $m_h > 2m_A$, the tetralepton + $\not{E}_T$ signatures resulting from decays of the form $h \to AA \to SS\ell^+\ell^-\ell^+\ell^-$ may also be detectable in certain regions of parameter space. The observation of signals of this sort, along with the non-observation of other signals which appear in standard 2HDM due to $\phi_i \bar{f} f'$ couplings (where $\phi_i = H^\pm, A, S$ and f and f' are SM fermions) absent in the Inert Doublet Model, could together serve to distinguish the IDM from other scenarios for physics beyond the Standard Model.

Evidence for the IDM could also come from a variety of other sources, including dark-matter-direct-detection experiments and from the observation of energetic gamma-rays [68, 69] or neutrinos [66] resulting from LIP dark matter annihilation. Clearly, the particular set of signals that an inert doublet would manifest differs substantially, depending on which of the allowed regions of parameter space the model happened to inhabit, and as we have shown, the $\ell^+\ell^- + \not{E}_T$ channel can provide an important probe into which region that might be.

2.1.3 Trilepton Signature at the LHC

Since a great many scenarios for physics beyond the Standard Model (BSM) also give rise to a $\ell^+\ell^- + \not{E}_T$ signature, it is worthwhile to investigate other channels which might also yield observable signals indicating the presence of an inert doublet. In this section, we focus on the detection prospects in the trilepton channel: $\ell^+\ell^-\ell^\pm + \not{E}_T$. Indeed, this channel has long been regarded as one of the most promising channels in which to look for evidence of physics beyond the Standard Model, and, in particular, of supersymmetry [81], due to its relatively small SM background.

Trilepton Production in the Inert Doublet Model

A number of processes contribute to the overall trilepton signal in the IDM. Here, we will concentrate on the most promising contributions for detection: those in which one lepton is produced via $W^{(*)}$ decay and the other two via $Z^{(*)}$ decay. The most significant such contributions are

- $q\bar{q}' \to AH^{\pm}$ with $A \to SZ^{(*)} \to S\ell^{+}\ell^{-}$ and $H^{\pm} \to SW^{\pm(*)} \to S\ell\nu$.
- $q\bar{q}' \to SH^{\pm}$ with $H^{\pm} \to AW^{\pm(*)} \to A\ell\nu$ and $A \to SZ^{(*)} \to S\ell^{+}\ell^{-}$.

the corresponding Feynman Diagrams for which are shown in Fig. 2.4. Note that in our analysis, we will consider the case in which $\ell = e, \mu$ only.

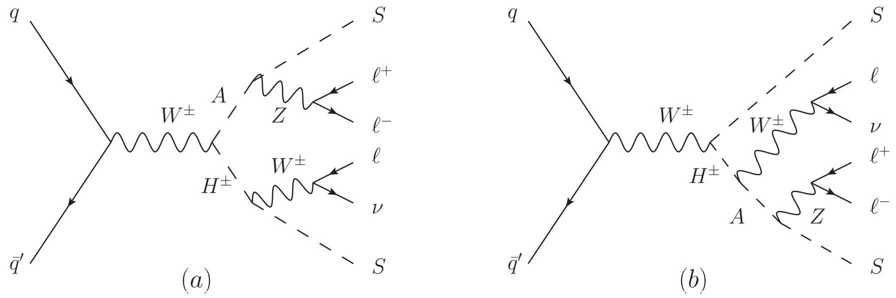

Figure 2.4: Diagrams corresponding to the processes which provide the leading contributions to the $\ell^{+}\ell^{-}\ell^{\pm} + \not{E}_T$ cross-section in the IDM.

Process (a) will occur in any IDM scenario in which the S plays the role of the LIP, whereas process (b) will occur only in scenarios in which $\delta_1 > \delta_2$ and will only be sizable when $\delta_1 < M_W$ or $\delta_1 > \delta_2 + M_W$. For all the benchmark points listed in Table 2.1, process (b) is sizable only for LH8. Even in that case, it is subdominant compared to process (a), the overall cross-section for which (taking into account all relevant decay branching ratios) is a factor of 20 larger than that for process (b). In cases in which $\delta_2 > \delta_1$, the process $q\bar{q}' \to AH^{\pm}$, with $A \to H^{\pm}W^{\mp(*)} \to H^{\pm}\ell\nu$ and $H^{\pm} \to SW^{\pm(*)} \to S\ell\nu$, also contributes to trilepton production. The leptons produced in this process all come from $W^{(*)}$ decay, and for this reason, it is difficult to resolve this process from the SM background. For all the benchmark points that we have selected for our study, however, the overall cross-section for this process is negligibly small, and can therefore be safely neglected.

Results for the LHC production cross-sections for the dominant ($pp \to AH^{\pm}$) signal process at $\sqrt{s} = 14$ TeV, as well as the branching fractions for $H^{\pm} \to S\ell^{\pm}\nu$

Benchmark	$\sigma_{AH^\pm}$ (fb)	BR($H^\pm \to S\ell^\pm\nu$)	BR($A \to S\ell^+\ell^-$)
LH1	125.2	0.216	0.067
LH2	299.0	0.233	0.068
LH3	154.9	0.233	0.069
LH6	187.0	0.216	0.069
LH7	204.2	0.233	0.067
LH8	159.4	0.226	0.070

Table 2.6: Leading-order cross-sections for the associated production of $AH^\pm$ at the LHC, with center-of-mass energy $\sqrt{s} = 14$ TeV, for the various benchmark points defined in Table 2.1. The relevant branching fractions of the scalars A and $H^\pm$ are also shown.

and $A \to S\ell^+\ell^-$ decay, are provided in Table 2.6. Note that for benchmark point LH8, the subdominant contribution to the trilepton signal from $pp \to SA^\pm$ has also been included in our analysis.

A number of processes contribute to the SM background for trilepton production. The most important of these is the irreducible background from WZ/γ^* production, though a number of reducible backgrounds also contribute. These include $t\bar{t}(j)$, $Wt(j)$, ZZ, and, as recently emphasized in [89], heavy-flavor processes such as $b\bar{b}Z/\gamma^*$ and $c\bar{c}Z/\gamma^*$.

In our analysis, event samples both for the signal process and for these backgrounds were generated at parton-level using the MadGraph [83] package. These events were subsequently passed through PYTHIA [84] for parton showering and hadronization, and then through PGS4 [85] to simulate the effects of a realistic detector. The one exception involves the background from heavy-flavor processes, which is somewhat cumbersome to analyze numerically, given the amount of data required to obtain a statistically reliable sample. However, as has been shown in Ref. [89], this background can be effectively eliminated via the implementation of a stringent missing energy cut of order $\not{E}_T > 50$ GeV. A similarly stringent cut on the total transverse momentum variable H_T should also be quite effective in this regard. We shall therefore assume that these backgrounds are effectively eliminated by the $\not{E}_T$ and H_T cuts included among our event-selection criteria.

Let us now turn to discuss those event-selection criteria, which we apply in three successive stages or sets, in more detail. The first set of cuts we impose (hereafter to be referred to as our Level I cuts) is designed to mimic a realistic detector acceptance. More specifically, we require:

- Exactly three charged leptons (either electrons or muons), including one same-flavor, opposite-sign (SFOS) pair.
- $p_T^\ell > 15$ GeV and $|\eta_\ell| < 2.5$ for each of these leptons.
- For lepton isolation, we require $\Delta R_{\ell\ell} > 0.4$ for each possible charged-lepton pairing, and $\Delta R_{j\ell} > 0.4$ for each combination of one jet and one charged lepton.

Our second set of cuts (hereafter referred to as our Level II cuts) is designed to suppress reducible backgrounds from SM processes which involve either hard jets or little missing transverse energy:

- No jets with $p_T^j > 20$ GeV and pseudorapidity $|\eta| < 3.0$.
- $\not{E}_T > 50$ GeV.

As discussed above, a missing-energy cut of this magnitude effectively eliminates the background from heavy-flavor processes such as $b\bar{b}Z/\gamma^*$ and $c\bar{c}Z/\gamma^*$. The jet veto is quite efficient in reducing background contributions from $t\bar{t}(j)$, $Wt(j)$, and other processes which involve substantial hadronic activity in the central region of the detector. Indeed, after the application of the Level I+II cuts discussed above, the dominant remaining background is the irreducible one from WZ/γ^* production, as shown in Table 2.7. In addition, there is also a non-negligible contribution (amounting to around 5% of the WZ/γ^* background) from residual $t\bar{t}(j)$ and $Wt(j)$ events which survive the jet veto. Other reducible backgrounds, including those from W + jets and heavy-flavor processes, are effectively eliminated by this choice of cuts.

After the imposition of the Level I and Level II cuts, we impose one further battery of event-selection criteria (hereafter referred to as our Level III cuts). Unlike

Signal			SM Background		
Benchmark	Level I (fb)	Level I+II (fb)	Process	Level I (fb)	Level I+II (fb)
LH1	0.760	0.317	WZ/γ^*	125.767	32.949
LH2	0.817	0.290	$t\bar{t}(j)$	38.869	1.046
LH3	0.289	0.082	$Wt(j)$	1.794	0.536
LH6	0.618	0.239	Total BG	166.430	34.531
LH7	1.089	0.420			
LH8	0.204	0.048			

Table 2.7: Cross-sections for the signal process $pp \to AH^\pm \to \ell^+\ell^-\ell^\pm + \not{E}_T$ in each of the benchmark scenarios presented in Table 2.1, and for the relevant SM backgrounds, after the application of our Level I and Level II cuts.

these first two sets of cuts, which are applied universally to all benchmark points used in this analysis, our Level III cuts are individually tailored to optimize the statistical significance of discovery for each benchmark point. A wide variety of possible criteria could in principle be used in this optimization process; however, we find that one particularly useful criterion that can be used to differentiate between signal and background events is the invariant mass $M_{\ell_Z\ell_Z}$ of the requisite pair of SFOS charged leptons (which we dub ℓ_Z^+ and ℓ_Z^-) that any event must include in order to pass the Level I cuts. If only one SFOS pairing can be constructed for a given event, $M_{\ell_Z\ell_Z}$ is unambiguously defined. In cases in which more than one SFOS combination exists and $\delta_2 \geq 70$ GeV, the pair whose invariant mass is closest to $\min(\delta_2, M_Z)$ will be identified as ℓ_Z^+ and ℓ_Z^-, and that invariant mass will be identified as $M_{\ell_Z\ell_Z}$. In cases in which $\delta_2 < 70$ GeV, the pair whose invariant mass is closest to 70 GeV will be so identified.[5]

The distribution for $M_{\ell_Z\ell_Z}$ peaks around M_Z for the Standard-Model WZ/γ^* background. For the signal process, the peak is around $\min(\delta_2, M_Z)$, as shown

---

[5] We choose this criterion for identifying the SFOS pair, rather that simply selecting whichever pair has an invariant mass closer to δ_2. This is because for $\delta_2 \leq 70$ GeV, the latter procedure would result in more frequent misidentification of which leptons were produced via Z/γ^* decay in the WZ/γ^* background sample, and consequently lower statistical significance values.

clearly in Fig. 2.5 for LH1 ($\delta_2 = 100$ GeV, top panel) and LH3 ($\delta_2 = 50$ GeV, bottom panel). This suggests that a cut on $M_{\ell_Z \ell_Z}$ around δ_2 has the potential to suppress significantly the SM background in scenarios in which $\delta_2 < M_Z$. Therefore, in our analysis, we select events on the basis of whether $M_{\ell_Z \ell_Z}$ lies below the threshold

- $M_{\ell_Z \ell_Z} \leq M_{\ell_Z \ell_Z}^{\max}$.

In principle, one could also introduce a minimum threshold for $M_{\ell_Z \ell_Z}$, but it turns out that the imposition of such a cut is not particularly helpful in practice; thus we will only make use of the above criterion in what follows.

Furthermore, in cases in which $A \to S\ell^+\ell^-$ decay occurs via an off-shell Z, the charged leptons will tend to be more collinear than those produced from the decay of an on-shell Z. For this reason, cuts such as

- $\cos\phi_{\ell\ell} \geq \cos\phi_{\ell\ell}^{\min}$
- $\Delta R_{\ell\ell} \leq \Delta R_{\ell\ell}^{\max}$,

where $\phi_{\ell\ell}$ is the azimuthal angle between the SFOS lepton pair, can be quite effective in discriminating between signal and background in cases in which $\delta_2 < M_Z$. In practice, we find the $\Delta R_{\ell\ell}^{\max}$ cut alone to be sufficient for our purposes, and thus make use of this criterion exclusively.

From the four-momentum of the remaining lepton (the one that is not part of the $\ell_Z^+ \ell_Z^-$ pair), which we dub ℓ_W, we can construct an additional quantity: a transverse-mass variable M_{T_W}, which we define according to the relation

$$M_{T_W}^2 \equiv (E_{\ell_W} + \not{E}_T)^2 - (\vec{p}_{T\ell_W} + \vec{\not{p}}_T)^2, \tag{2.9}$$

where $\not{E}_T$ and $\vec{\not{p}}_T$ respectively denote the *total* missing transverse energy and missing transverse momentum vector. The distribution for M_{T_W} drops sharply around M_W for the SM WZ/γ^* background. A similar drop also occurs for the signal process, in cases in which the $H^\pm$ decays via an on-shell W, but the presence of additional sources of $\not{E}_T$ (the pair of LIPs) in this case results in a smoother M_{T_W} distribution that falls more gently above M_W. In cases in which $\delta_1 < M_W$, and the lepton in

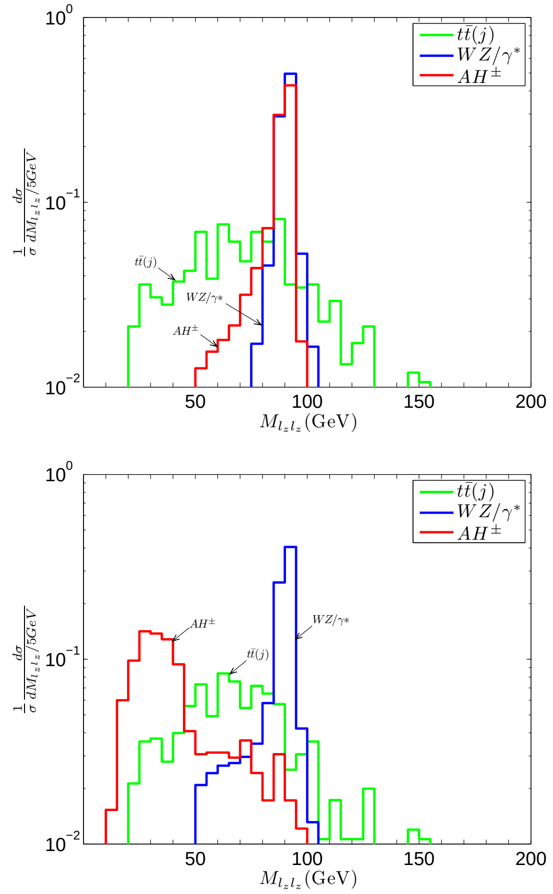

Figure 2.5: Distributions of the invariant mass of the SFOS lepton pair after the application of the Level I+II cuts described in the text, in our benchmark scenarios LH1 (top panel) and LH3 (bottom panel), both for the signal process and for the dominant SM backgrounds. Note that the area under each distribution histogram has been normalized to one.

question comes from off-shell W decay, the drop in M_{T_W} is quite gradual and occurs near δ_1. The distributions for M_{T_W}, both for the signal process and for the dominant SM backgrounds, are shown in Fig. 2.6 for LH1 ($\delta_1 = 100$ GeV, top panel) and LH3 ($\delta_1 = 50$ GeV, bottom panel). The evidence in this figure suggests that in cases in which $\delta_1 > M_W$, imposing a minimum threshold for M_{T_W} can be helpful in reducing the dominant WZ/γ^* background. Conversely, when $\delta_1 < M_W$ an upper limit on M_{T_W} can likewise be of use. Motivated by these considerations, we allow for either a minimum or a maximum threshold for M_{T_W} in our event-selection criteria, and only retain events for which

- $M_{T_W} \geq M_{T_W}^{\min} \quad$ or $\quad M_{T_W} \leq M_{T_W}^{\max}$,

depending on the benchmark point in question. As we shall see, such cuts on $M_{\ell_Z \ell_Z}$ and M_{T_W} will turn out to be particularly useful in distinguishing a trilepton signal from the dominant WZ/γ^* background.

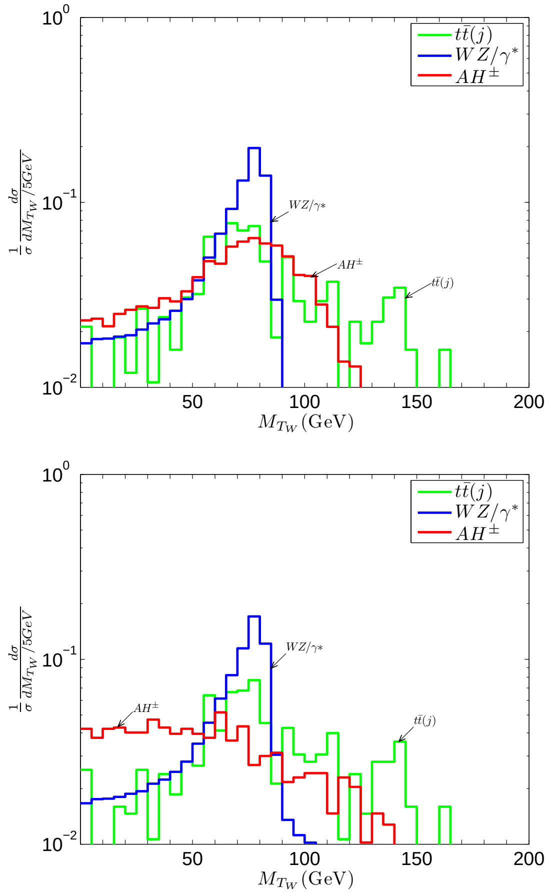

Figure 2.6: Distributions of the transverse mass variable M_{T_W} defined in Eq. (2.9), after the application of the Level I+II cuts described in the text, in our benchmark scenarios LH1 (top panel) and LH3 (bottom panel), both for the signal process and for the dominant SM backgrounds.

Benchmark	$M_{\ell_Z \ell_Z}^{\max}$ (GeV)	$M_{T_W}^{\min}$ (GeV)	$M_{T_W}^{\max}$ (GeV)	$\Delta R_{\ell\ell}^{\max}$	$H_T^{\min}$ (GeV)	$p_{T\ell}^{\min}$ (GeV)
LH1	100	90	–	1.6	240	–
LH2	65	–	60	1.3	150	–
LH3	50	–	60	1.2	140	–
LH6	65	–	–	1.1	200	20
LH7	100	–	65	–	200	–
LH8	40	–	–	–	–	–

Table 2.8: A list of the optimized Level III cuts used in the analysis of each of the benchmark points presented in Table 2.1. An entry of "–" indicates that the corresponding cut is not imposed. For more details on the definition of the thresholds used, see text.

It can also be useful to impose a more stringent lower limit $p_{T_\ell}^{\min}$ on the transverse momentum p_{T_ℓ} of the charged leptons than that imposed at Level I:

- $p_{T_\ell} \geq p_{T_\ell}^{\min} > 15$ GeV.

Likewise, a cut on the total-transverse-momentum variable H_T:

- $H_T \geq H_T^{\min}$,

with H_T defined in terms of the sum

$$H_T = \not{E}_T + \sum_{i=1}^{3} |p_{T\ell_i}|, \tag{2.10}$$

can also be useful in differentiating signal from background. A roster of the particular cuts implemented for each benchmark used in our analysis is compiled in Table 2.8.

Results

In Table 2.9, we show the discovery potential for the trilepton signal at the LHC (assuming a center-of-mass energy of 14 TeV) for each of the IDM benchmark points defined above, assuming an integrated luminosity of 300 fb^{-1} in each of the two detectors. The best prospects for discovery are obtained for the benchmarks LH2

Benchmark	Level III Cuts						
	$\sigma_{H^\pm A}$ (fb)	σ_{WZ/γ^*} (fb)	$\sigma_{t\bar{t}(j)}$ (fb)	$\sigma_{Wt(j)}$ (fb)	$\sigma_{\text{BG}}^{\text{comb}}$ (fb)	S/B	$S/\sqrt{B}$ (300 fb^{-1})
LH1	0.038	0.159	0.020	0.011	0.191	0.20	2.15
LH2	0.078	0.073	0.019	0.021	0.114	0.68	5.64
LH3	0.035	0.093	0.023	0.014	0.131	0.27	2.36
LH6	0.101	0.185	0.030	0.007	0.221	0.46	5.27
LH7	0.270	7.137	0.084	0.038	7.259	0.04	2.45
LH8	0.031	0.385	0.144	0.061	0.591	0.05	1.00

Table 2.9: Cross-sections for the signal process $pp \to AH^\pm \to \ell^+\ell^-\ell^\pm + \not{E}_T$ and for the dominant SM backgrounds from WZ/γ^*, $t\bar{t}(j)$ and $Wt(j)$ production for each of the benchmark points presented in Table 2.1, after the application of our Level III cuts. The total background cross-section is also shown. The last two columns display the signal-to-background ratio S/B, and the statistical significance (as given by $S/\sqrt{B}$) corresponding to an integrated luminosity of $\mathcal{L} = 300$ fb^{-1} in each detector at the LHC (operating at a center-of-mass energy $\sqrt{s} = 14$ TeV), after the application of these same cuts.

and LH6, each of which yields a statistical significance of more than 5σ. The reason why these benchmarks are comparatively auspicious is twofold. First, both involve a light LIP, with a mass $m_S \sim 40$ GeV. Second, both also feature a mass splitting $\delta_2 \sim 70$ GeV, which, on the one hand, is small enough that $A \to SZ \to S\ell^+\ell^-$ decays will occur through an off-shell Z boson, but, on the other hand, is large enough so that the resulting charged leptons will not generally be too soft to escape detection.

For LH7, which features a similarly light LIP, with $m_S \sim 40$ GeV, but for which $(\delta_1, \delta_2) = (70, 100)$ GeV, the primary difficulty in resolving the signal is that the (dominant) WZ/γ^* background cannot be suppressed by applying a Z veto on $M_{\ell_Z\ell_Z}$, since $A \to SZ \to S\ell^+\ell^-$ decays occur via an on-shell Z. Indeed, this two-body decay mode of the A is analogous to what are often referred to as "spoiler" processes in the literature on trilepton signals in weak-scale supersymmetry [81]. Thus, although the signal cross section for LH7 after cuts is relatively large, the unsuppressed Standard-Model WZ/γ^* background renders discovery via this channel difficult. As for LH1, for which $\delta_{1,2} > M_{W,Z}$, the Standard-Model WZ/γ^* background can be suppressed by imposing a lower limit on M_{T_W}. The signal cross section, however, is very small after the imposition of this cut, which renders a discovery via this channel difficult for this benchmark scenario as well.

The discovery prospects for benchmark point LH3 are also less auspicious. One reason for this is that the LIP mass is far heavier in this scenario, and the production cross-section is therefore appreciably lower, as indicated in Table 2.6. Another is that since δ_1 and δ_2 are smaller for this benchmark than for LH1 and LH6, the charged leptons will be significantly softer, and more of them will escape detection. For this reason, a proportionally greater reduction in signal events occurs as a result of our detector-acceptance cuts, as can be seen from Table 2.7. For benchmark point LH8, δ_2 is smaller still, and the effect of the Level I cuts even more severe; hence the trilepton signal is even more difficult to resolve.

A few further remarks comparing and contrasting the trilepton phenomenology of the IDM with that of supersymmetric models are in order. Indeed, the process $pp \to H^\pm A \to \ell^+\ell^-\ell^\pm + \not{E}_T$, which yields the dominant contribution to the trilepton signal in the IDM is in many ways analogous to the direct chargino-neutralino production process $pp \to \chi_2^0\chi_1^\pm$, with $\chi_2^0 \to \chi_1^0 Z^{(*)} \to \chi_1^0\ell^+\ell^-$ and $\chi_1^\pm \to \chi_1^0 W^{(\pm *)} \to \chi_1^0 \ell\nu$, where $\chi_{1,2}^0$ are the lightest and second lightest neutralinos and $\chi_1^\pm$ is the lightest chargino. This channel has long been regarded as a promising discovery channel for weak-scale supersymmetry. Indeed, as was shown in [90], for certain opportune regions of parameter space, an observable signal could be obtained with less than 30 fb^{-1} of integrated luminosity at the LHC. More recently, the CMS collaboration, working in the context of minimal supergravity, has indicated that a 5σ discovery of supersymmetry could be achieved in this channel with 30 fb^{-1} of integrated luminosity, provided that the gaugino mass parameter $M_{1/2} \leq 180$ GeV [87].

Thus, we see that given similar mass spectra, the discovery prospects for the supersymmetric process are markedly better than those for its IDM counterpart. This is primarily due to to the substantial difference — a relative factor of around

16 — between the production cross-sections for $pp \to \chi_2^0\chi_1^\pm$ in the minimal supersymmetric Standard Model (MSSM) and $pp \to AH^\pm$ in the IDM. This difference owes to two important distinctions between the characteristics of the relevant particles in the two models. The first of these is that $\chi_1^\pm$ and χ_2^0 are Weyl fermions whereas $H^\pm$ and A are real scalars. As a consequence, the cross-sections for the corresponding processes in the two models differ by a relative factor of roughly 4 in the high-energy limit (i.e. the limit in which $s \gg m_i^2$, where m_i denotes the mass of any of the particles involved in the interaction). The second relevant distinction is that the scalar doublet ϕ_2 of the IDM is in the fundamental representation of $SU(2)$, whereas the charged and neutral Winos (which respectively constitute the dominant components of $\chi_1^\pm$ and χ_2^0 in the relevant region of SUSY parameter space) are in the adjoint representation. This translates into another relative factor of 4 between the corresponding production cross-sections. The practical consequence of this result, of course, is that observing a trilepton signal in the IDM is far more difficult than it is in its MSSM analogue. Indeed, we have seen that although the trilepton channel is one of the cleanest channels in which one might hope to discover supersymmetry at the LHC, in the IDM, this channel can only be observed in the region of parameter space in which the LIP is light ($m_S \sim 40$ GeV) and the mass splitting δ_2 is relatively large ($\delta_2 \sim 70$ GeV).

While the above analysis was performed assuming a center-of-mass energy $\sqrt{s} = 14$ TeV, it is also worthwhile to consider how the discovery prospects would differ at an LHC operating energy of $\sqrt{s} = 10$ TeV. In this case, the $pp \to H^\pm A$ production cross-sections are reduced to roughly 60% of the values given in Table 2.6, while the (generally dominant) WZ/γ^* background drops to roughly 80% of its 14 TeV value. Since signal event count is not generally a limiting factor in event selection, we would expect each of the $S/\sqrt{B}$ values quoted above to drop to roughly 65% of its 14 TeV value at a 10 TeV machine, given identical luminosities and assuming similar cut efficiencies. While this is not an imperceptible reduction, it is by no means a severe one; thus, were our universe in fact to resemble that described by an IDM benchmark scenario such as LH2 or LH6, one would still expect to see evidence of trilepton production from the decays of heavy inert particles at the LHC, even at $\sqrt{s} = 10$ TeV.

Conclusions

The Inert Doublet Model is a simple yet incredibly versatile scenario for physics beyond the Standard Model. Among its phenomenological advantages is that it provides a viable WIMP dark-matter candidate in the form of the lightest inert particle. In this section, we have investigated the observability of a trilepton signal at the LHC in the Inert Doublet Model. While the first signals of an inert doublet at the LHC are likely to appear in the dilepton channel [58], the observation of a signal in the trilepton channel could provide valuable additional information about the parameter space of the model and assist in distinguishing the IDM from other BSM scenarios which give rise to similar signature patterns. We have shown that at an integrated luminosity $\mathcal{L} = 300$ fb^{-1}, it should be possible to resolve the trilepton signal, provided that the LIP is light ($m_S \sim 40$ GeV), the mass splitting δ_2 lies within the range 50 GeV $\leq \delta_2 \leq M_Z$, and δ_1 is small enough ($\delta_1 \leq 100$ GeV) that $H^\pm A$ production is not drastically suppressed. These criteria coincide with those which lead to the best detection prospects in the dilepton channel as well.

It should be noted, however, that one could only hope to observe a trilepton signal in regions of parameter space in which the Higgs is lighter than around 180 GeV. Although the Inert Doublet Model can certainly accommodate a heavier Higgs boson — indeed, among the model's numerous advantages is its ability to alleviate the little hierarchy problem — the requisite contributions to the oblique T parameter needed for this owe to the existence of a sizable mass splitting between $H^\pm$ and S. When this is the case, the $pp \to AH^\pm$ production cross-section will be highly suppressed, and the trilepton-signal contribution from this process will consequently be unobservable at the LHC.

As a final word, we note that although the analysis performed in this work was conducted within the framework of the Inert Doublet Model, similar signatures involving the production of charged and neutral scalars which subsequently decay into other, lighter, scalar particles and SM gauge bosons appear in many other BSM scenarios. We emphasize that our results should also apply in any such scenario in which the aforementioned lighter scalar particle is neutral and stable (on collider time scales), and hence appears in the detector as missing energy. The observation of a clean trilepton + $\not{E}_T$ signal above the SM background would be a clear indication of new physics. To determine the precise nature of that new physics, however, and to pin down the particle nature of the dark matter candidate will likely require additional data from a variety of sources. These may include complementary channels at the LHC, signals at direct or indirect dark-matter-detection experiments, or results from one of many other available experimental probes of physics beyond the Standard Model.

2.2 The Left-Right Twin Higgs Model at the LHC

The twin Higgs mechanism [33, 34, 35] is proposed as a solution to the little Hierarchy problem, which employs the idea of Higgs boson as Goldstone arising from breaking a global symmetry for the Higgs sector. Upon invoking a discrete symmetry [36], the quadratic contribution to the Higgs potential respects the global symmetry. The leading divergence in one-loop correction to the Higgs mass squared is at most logarithmic, greatly reducing the amount of fine-tuning.

The twin Higgs mechanism can be implemented in a couple of ways. The discrete symmetry can be identified as the mirror parity [34]. A complete copy of the SM particle content and interactions is introduced. The leading quadratic divergences from the SM particle and the mirror copy cancel out.

The left-right symmetry [36] also works here, which brings in new particles as necessary. A variety of heavy states emerges: the heavy gauge bosons $W_H^{\pm}$ and Z_H, heavy top quark T, extra neutral/charged Higgs bosons. The cancellation of the quadratic divergence to the Higgs mass occurs between the SM particle and the heavy states.

In what follows, we first review the model setup of the LRTH as in Sect. 1.2.3.

Here we focus on the mass spectrum that is most relevant to collider study of the heavy top T and define a set of benchmark points. Then we go on to explore the heavy top quark production and SM backgrounds at the LHC, and develop an event-selection procedure. At the very end of the section, we present the optimized cuts and the results.

2.2.1 Model Framework, Mass Spectrum and Benchmarks

In the LRTH model, a global $U(4)\times U(4)$ symmetry is imposed on the Higgs potential, with gauged subgroup $SU(2)_L \times SU(2)_R \times U(1)_{B-L}$. The discrete symmetry to invoke $U(4)$ invariant quadratic contribution to the potential is identified as the left-right symmetry, which interchanges L with R. The left-right symmetry equates the gauge couplings of the left and right $SU(2)$ group: $g_L = g_R \equiv g$.

Two Higgs fields are introduced:

$$H = \begin{pmatrix} H_L \\ H_R \end{pmatrix}, \quad \hat{H} = \begin{pmatrix} \hat{H}_L \\ \hat{H}_R \end{pmatrix}, \tag{2.11}$$

where H_L is the $SU(2)_L$ doublet and H_R is the $SU(2)_R$ one. They transform as (**4**, **1**) and (**1**, **4** repectively. Once the the H and $\hat{H}$ develop vev's: $\hat{f} \gg f$,

$$\langle H\rangle = \begin{pmatrix} 0 \\ 0 \\ 0 \\ f \end{pmatrix}, \qquad \langle \hat{H}\rangle = \begin{pmatrix} 0 \\ 0 \\ 0 \\ \hat{f} \end{pmatrix}, \tag{2.12}$$

the global symmetry is spontaneously broken, with 14 Goldstone bosons. The $SU(2)_R \times U(1)_{B-L}$ gauge symmetry is also broken, into the $U(1)_Y$ of the SM.

Three of the Goldstone bosons are eaten by the gauge bosons and become the longitudinal components of $W_H^{\pm}$ and Z_H. The masses of the heavy gauges bosons are:

$$\begin{aligned} m_{W_H}^2 &= \frac{1}{2} g_2^2 (\hat{f}^2 + f^2 \cos^2 x), \\ m_{Z_H}^2 &= \frac{g_1^2 + g_2^2}{g_2^2} (m_{W_H}^2 + m_W^2) - m_Z^2, \end{aligned} \tag{2.13}$$

where $x = v/\sqrt{2}f$, $g_1 = e/\sqrt{\cos 2\theta_w}$ and $g_2 = e/\sin\theta_W$ are the gauge couplings of the $SU(2)$ and $U(1)_{B-L}$ respectively and are related to the e and the Weinberg angle.

The remaining Goldstone bosons obtain masses through loop corrections. The masses can be obtained by expanding the one-loop CW potential. Of particular interest is the mass of the charged scalars [6]:

$$m_{\phi^\pm}^2 \sim \frac{3}{16\pi^2} g_1^2 m_{W_H}^2 \left(\log \frac{\Lambda^2}{m_{Z_H}^2} + 1 \right), \tag{2.14}$$

where λ is the cutoff scale of the model, usually taken to be $4\pi f$.

To account for the $O(1)$ top Yukawa coupling and a top mass $\sim$ weak scale, a pair of vector-like quarks are introduced as in Eq.(1.56). Once the Higgs field $H = (H_L, H_R)$ develops vev, a light SM top quark and a heavy top quark T emerge, with masses:

$$m_t^2 \sim y^2 f^2 \sin^2 x - M^2 \sin^2 x \sim (\frac{yv}{\sqrt{2}})^2, \tag{2.15}$$

$$m_T^2 = y^2 f^2 + M^2 - m_t^2, \tag{2.16}$$

where M controls the mixing between the light and heavy top quarks.

The free parameters that control the mass spectrum relevant for collider study of the heavy top quark are:

$$\{f, \Lambda, M\}. \tag{2.17}$$

The cutoff scale is usually taken to be $4\pi f$. The mixing parameter M is in general small, here to be fixed at 150 GeV. A table of benchmark points are listed in Table.2.10 for f in the range 500 GeV – 1.5 TeV.

2.2.2 Heavy Top Quark Signature at the LHC

Signals, Backgrounds and Event Selection

One single heavy top quark can be produced at the LHC with one extra jet, via s-channel or t-channel W or W_H exchange as is shown in Fig. 2.7. For a heavy

---

[6] For exact mass formulas, refer to [91]

	mass spectrum (GeV)			
f (GeV)	m_T	m_{W_H}	m_{Z_H}	$m_{\phi^\pm}$
600	614	1393	1665	199
1000	1007	2605	3115	321
1500	1504	4053	4846	476

Table 2.10: Benchmark points for the LRTH mode.

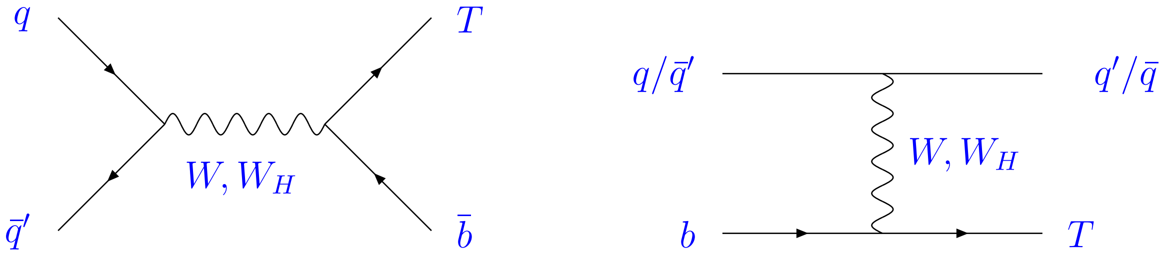

Figure 2.7: Feynman diagram for single heavy top production at the LHC.

top with mass 500–1500 GeV, the cross-section is in the range 7×10^3 fb – 10 fb. The contribution from diagrams involves the W boson is negligible, the reason is two-fold: first of all, the heavy top quark mass is larger than the W boson mass by an order of magnitude (see Table. 2.11), secondly the $W\bar{T}b$ coupling is suppressed by $(M/f)(v/f)$. As for the W_H, since it is heavier than the heavy top T, the intermediate W_H in the s-channel is mostly on-shell; thus it contributes more than 80% to the total cross-section. The implication here is that the jet associated with the single production of heavy top is mostly a b-jet, as opposed to u/d jets from the t-channel process.

The pair production of heavy tops at the LHC is also possible, in similar manner to the pair production of the SM top quark, via gluon exchange: $q\bar{q}, gg \to T\bar{T}$. In the case of pair production of the SM top quarks, the large QCD coupling leads to huge cross-section, which makes the LHC a "top factory". However, it is not the case for the heavy top T. The pair production process suffers from severe phase space suppression, due to the significantly large heavy top quark mass. The cross-section of the pair production is about a factor of five smaller than that of single production mentioned above. Thus in what follows, we focus only on heavy top quark from the single production mode.

Once produced at the LHC, the heavy top quark could decay into ht, Zt and Wb, but predominantly into $\phi^+ b$. This is best understood if one examines the relevant couplings of the suppressed decay modes: they are all accompanied by a factor of $\frac{M}{f}$ due to the mixing between the heavy and the light top. For our benchmarks, where M is taken to be 150 GeV and f is in the range 500 GeV – 1500 GeV, the suppression factors for couplings are in the range 0.1 – 0.3, relative to the un-suppressed $\phi^+ \bar{T} b$. Numerically, more than 70% of the time the heavy top T ends up in $\phi^+ b$ channel.

The cascade decay chain for heavy top T under investigation is thus:

$$T \to \phi^+ b, \quad \phi^+ \to tb, \quad t \to W^+ b \to l^+ \nu b. \tag{2.18}$$

The appearance of the SM top quark t in ϕ^+ decay is natural, because of the large Yukawa coupling it bears. For lepton identification and triggering efficiency consideration, l is understood to be either e or μ in this section, unless explicitly stated otherwise. The signal of the heavy top quark at the LHC comprises of 4 b jets + one charged lepton (e or μ) + missing $\not{E}_T$, where the additional energetic b jet associated with the single T production is also taken into account.

Several SM processes produce similar final states as the LRTH heavy top cascade decay, the first of which is $t\bar{t}$ process, where the SM top quarks decay into two b quarks and W boson, followed by leptonic decay for one of the W boson and hadronic decay for the other. The collider signature of $t\bar{t}$ process is thus $bbjj + l^\pm +$ missing $\not{E}_T$. The QCD processes are another source of backgrounds: $Wjjjj$, $Wcjjj$, $Wccjj$ and $Wbbjj$, where W boson undergoes leptonic decay into e or μ and $j = u, d, s$ here indicates jets originating from light quarks.

In the present study, signal and the SM $t\bar{t}$ background events are generated at parton-level, in MadGraph [83], followed by the decay of unstable particles in BRIDGE [92]. QCD backgrounds are generated at parton-level in Alpgen [93]. All events are then passed through PYTHIA [84] for parton showering and hadronization

Signal			SM backgrounds			
Benchmarks f (GeV)	σ_{Tj} (fb)	$\sigma_{\bar{T}j}$ (fb)	Process	σ (pb)	Process	σ (pb)
600	360.8	144.7	$t\bar{t}$	90	$Wbbjj$	4.87
1000	29.5	8.6	$Wjjjj$	244.5	$Wccjj$	4.56
1500	2.2	0.5	$Wcjjj$	45.2		

Table 2.11: Cross-sections of signal processes $pp \to Tj/\bar{T}j$ in three benchmarks in LRTH model, as well as relevant SM backgrounds For SM processes, both of the conjugated processes are included. The cross-sections listed are understood as after fully decay of any unstable state and after the application of Stage-I selection cuts.

and PGS4 for detector effect simulation.

To account for detector performance thresholds and better understand the difference among signals and backgrounds, the following Stage-I cuts are imposed on all events:

- Exactly one charged lepton $l^{\pm}$ with $P_{T,l} > 10$ GeV and $|\eta_l| < 2.5$, where $l = e/\mu$.
- For lepton isolation, $\Delta R_{jl} > 0.4$ for each combination of the lepton and one of the jets presented.

The resulting cross-sections are listed in Table 2.11. Both the $t\bar{t}$ and the QCD $W + 4$ jets type backgrounds have cross-sections orders of magnitudes larger than the heavy top signal cross-section. The smallness of the signal cross-section is a reflection of the restricted phase space due to the extremely massive T. The enormous cross sections of the backgrounds, on the other hand, are due to the large QCD coupling strength taking part in the SM background processes. However, the signal kinematics and topology differ from that of the backgrounds significantly in a variety of ways.

The leading jet transverse-momentum P_T distribution reveals drastically distinct features between the signal and the background processes. In single production of heavy top T, the s-channel diagram with intermediate heavy boson W_H dominates. The b jet coming from W_H on-shell decay bears extremely high P_T with a sharp

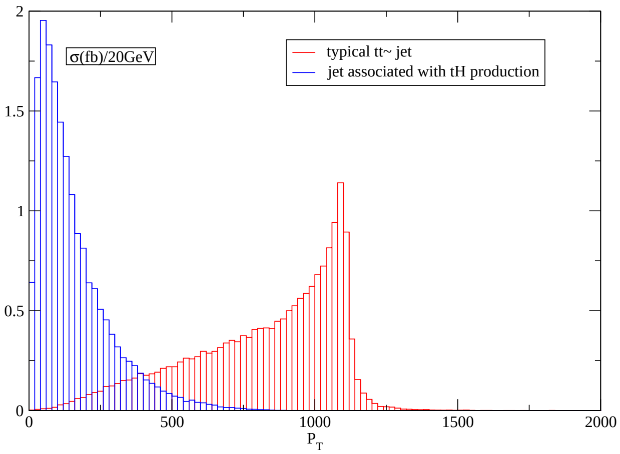

Figure 2.8: Leading jet P_T distribution from the heavy top production ($f = 1000$ GeV) and $t\bar{t}$ backgrounds.

edge around f and comprises most of the time the jet with leading P_T. It is obvious from the distribution plot in Fig. 2.8 leading jet P_T rarely goes below 200 GeV for the signal process in $f = 1000$ GeV benchmark. The other two benchmarks display similar feature in leading jet P_T distribution, with edges located according to the mass spectrum of the heavy particles. On the contrary, the jets from $t\bar{t}$ are relatively soft and the leading jet P_T peaks at the low P_T region $\sim$ 50–100 GeV. In the QCD $W + 4$ jets backgrounds, the jets are even more soft. A careful designed cut on the leading jet P_T thus serves to cut down the SM backgrounds, while holding onto the heavy top signal. Based on this observation, we impose a cut on the leading transverse-momentum among jets:

- Leading jet $P_T > P^{min}_{T,leadingjet}$,

where the $P^{min}_{T,leadingjet}$ varies with the benchmarks, for optimal outcome in terms of the signal-to-background ratio. Similar cuts on the second leading jet P_T are sometimes employed.

The difference from topology of the cascade decay chain of the heavy top T to that of the $t\bar{t}$ and the QCD processes also helps to distinguish the signal from the SM backgrounds. Subsequent to the point of production of heavy top T, it decays following a long chain: $T \to \phi^{\pm}$, $\phi^{\pm} \to tb$, $t \to Wb$ and at the last stage $W \to l\nu$. The hierarchy in the mass spectrum of T, $\phi^{\pm}$, t, $W^{\pm}$ makes the decay involved in the chain mostly on-shell, forming a series of resonances, which are obviously absent in the $t\bar{t}$ and QCD backgrounds.

We then construct the resonances bottom-up starting with the W boson and top quark t and require that the reconstructed mass to be in the vicinity of the assumed mass $\{m_W,\, m_t,\, m_{\phi^{\pm}},\, m_T\}$ in the benchmarks. The reconstruction of the W and t also fixes the momentum of the missing neutrino.

- The beam direction momentum of the neutrino P_z^{ν} is calculated up to a two-fold ambiguity, assuming that P_z^{ν} combined with the missing $\not{E}_T$ and the lepton constructs a W boson of mass m_W.

- The candidate P_z^{ν} together with missing $\not{E}_T$ and the lepton is combined with all jets one at a time to form a t resonance. The combination of $\{P_z^{\nu}$, lepton, jet$\}$ with reconstructed mass M_t that best matches m_t is kept. Label the jet added at this stage $jet(t)$. We impose the following cuts on the reconstructed mass M_t and the transpose momentum of $jet(t)$:

$$\begin{aligned} m_t - \Delta m_t < &M_t < m_t + \Delta m_t, \\ P^{min}_{T,jet(t)} < &P_{T,jet(t)}. \end{aligned}$$

  The event is discarded should it fail the cuts.

- A second jet is added to reconstruct the $\phi^{\pm}$ resonance. The combination with reconstructed mass $M_{\phi^{\pm}}$ that best matches $m_{\phi^{\pm}}$ is kept. Label the jet added at this stage $jet(\phi^{\pm})$. We impose the following cuts on the reconstructed mass $M_{\phi^{\pm}}$ and the transpose momentum of $jet(\phi^{\pm})$:

$$\begin{aligned} m_{\phi^{\pm}} - \Delta m_{\phi^{\pm}} < &M_{\phi^{\pm}} < m_{\phi^{\pm}} + \Delta m_{\phi^{\pm}}, \\ P^{min}_{T,jet(\phi^{\pm})} < &P_{T,jet(\phi^{\pm})}. \end{aligned}$$

The event is discarded should it fail the cuts.

- A third jet is added to reconstruct the heavy top T resonance. The combination with reconstructed mass M_T that best matches m_T is kept. Label the jet added at this stage $jet(T)$. We impose the following cuts on the reconstructed mass M_T and the transpose momentum of $jet(T)$:

$$\begin{aligned} m_T - \Delta m_T <& M_T < m_T + \Delta m_T, \\ P^{min}_{T,jet(T)} <& P_{T,jet(T)}. \end{aligned}$$

The event is discarded should it fail the cuts.

The notation we adopt on subscript "T" is seemingly confusing. The rule is: following mass (m/M) or to label a jet, it means the heavy top T; otherwise (following momentum or energy P/E), it stands for "transverse".

The signal topology differs furthermore from the backgrounds in that it comprises mostly 4 b-jets, whereas the backgrounds contain at most two. Thus we find it particularly useful to place a cut on the number of jet tagged as b jet and require:

$$N_b^{min} < N_b, \tag{2.19}$$

where again N_b^{min} is chosen for optimal signal-to-background ratio.

Optimized Cuts and Results

Now that we have discussed extensively the event-selection procedure for the heavy top production at the LHC, we turn to present the optimized cuts and the results of the numerical analysis. We list the optimized cuts imposed on each of the three benchmark points in Table 2.12 and the corresponding cross sections and $S/\sqrt{B}$ ratio in Table 2.13.

The first set of cuts applied on missing $\not{E}_T$ and $P_{T,l}$ works on both signal and background processes. The distributions of both quantities do not vary much in different benchmark points, which explains the universal lower bounds.

Cuts (GeV)	Benchmarks		
	$f = 600$ GeV	$f = 1000$ GeV	$f = 1500$ GeV
$\not{E}_T^{min}$	15	15	15
$P_{T,l}^{min}$	30	30	30
$P_{T,leadingjet}^{min}$	400	600	1000
Δm_t	20	30	50
$P_{T,jet(t)}^{min}$	30	0	0
$\Delta m_{\phi^\pm}$	30	100	100
$P_{T,jet(\phi^\pm)}$	0	30	30
Δm_T	50	200	300
$P_{T,jet(T)}^{min}$	250	250	400
N_b^{min}	2	2	1

Table 2.12: A list of the optimized cuts in each of the benchmark points. All threshold quantities bear units of GeV, except for N_b^{min}.

The leading jet P_T distribution does vary between benchmark points, with peak positively correlated with the mass of heavy top T, or equivalently f. Stringent cuts are possible when we have large f, in which case we can relax other cuts applied, in order to keep more of the signal.

The constraints imposed on the resonances and the jet at each stage of reconstruction are the third set of cuts listed in Table 2.12. The Δm's chosen in the table reflects partially the width of the the massive states. As can be observed for $\phi^\pm$ and T reconstruction stages, the selected Δm steps up when we go from benchmark point with $f = 600$ GeV to $f = 1500$ GeV. The P_T cut on the jet shows similar trend.

The cross sections are listed in Table 2.13. For SM backgrounds, we always report 95% C.L. upper bounds. Due to the enormous production cross sections of the backgrounds, the sample sizes necessary to render significant statistics exceeds the computational capacity of regular PC in a limited time frame. Our approach, instead of generating a huge sample, is to assume a Poisson distribution of the observed number of events that pass our optimal cuts, and infer the 95% upper bound on the Poisson parameter which is interpreted as the expected number of

f (GeV)	600	1000	1500
σ_{Tj} (fb)	0.98	0.72	0.16
$\sigma_{\bar{T}j}$ (fb)	0.59	0.26	0.04
σ^{comb}_{signal} (fb)	1.57	0.98	0.20
$\sigma_{t\bar{t}}$ (fb)	<0.108	<0.108	<0.027
σ_{Wjjjj} (fb)	<0.801	<0.267	<0.076
σ_{Wcjjj} (fb)	<0.146	<0.097	<0.028
σ_{Wbbjj} (fb)	<0.092	<0.023	<0.011
σ_{Wccjj} (fb)	<0.058	<0.058	<0.013
σ^{comb}_{BG} (fb)	<1.21	<0.55	<0.16
S/B	1.20	1.78	1.25
$S/\sqrt{B}$	7.81	7.23	2.74

Table 2.13: Cross sections for signal and background processes at the LHC for each of the benchmark points, after the application of the optimized cuts Listed in Table.2.12. The $<$ sign indicates a 95% C.L. upper bounds. The $S/\sqrt{B}$ ratios corresponds to an integrated luminosity of 30fb^{-1}.

events. We then report the cross section associated with this number as is listed in Table 2.13.

Benchmark point with $f = 600$ GeV and $f = 1000$ GeV shows the best potential of being discovered at the LHC. With an integrated luminosity of 30 fb^{-1}, we are expecting $\sim$ 47/30 events respectively for these two benchmark points, at a significance level exceeding 7 σ.

For $f = 1500$ GeV, however, the significance level drops to $\sim$ 2.7, with an expected number of events $\sim$ 6. It is not surprising that we find it difficult to observe heavy top T: the cross section of the signal production is so tiny to begin with. However, in later stages of the LHC operation when the luminosity is accumulated up to 100 fb^{-1}, the $S/\sqrt{B}$ ratio is raised above 5, with an expected number of heavy top events $\sim$ 20.

Conclusion

In this section, we have investigated the potential for observing the heavy top quark T signature in the LRTH model at the LHC. We have covered a variety of benchmarks points that is phenomenologically viable, with the heavy top T mass as high as ~ 1.5 TeV. We have demonstrated that an integrated luminosity of 30 fb^{-1} would reveal the heavy top quark signature with a significance level exceeding 7 σ, should the heavy top T bear mass in the range 600 GeV up to 1 TeV. We would have to wait till the LHC accumulates an integrated luminosity of 100 fb^{-1} for a 1.5TeV heavy top T.

Of course, the confirmation of twin Higgs mechanism at the LHC could come from other signatures within the LRTH model. The heavy neutral gauge bosons Z_H provides yet another interesting possibility. The dominant Z_H decay mode is into di-jets, however this mode suffers from the overwhelming QCD di-jet backgrounds. The discovery mode of Z_H could be the leptonic decay into l^+l^-. with a branching ratio of 2.5% for each lepton species. $e^+e^-/\mu^+\mu^-$ final states provides a clean signal. The invariant di-lepton invariant mass $m_{l^+l^-}$, peaked at M_{Z_H} high above, distinguishes the heavy gauge boson signature from that of the SM backgrounds.

CHAPTER 3

PRECISION OBSERVABLES AND SUSY BREAKING

With the help of the LHC, it is now possible to explore TeV territory which was never directly reachable experimentally. However, the precision data provides complimentary approach probing new physics. Here we present hints gathered from precision observables, concerning the mechanisms of soft SUSY-breaking.

3.1 Introduction

The dimensionality of the parameter space of the minimal supersymmetric extension of the Standard Model (MSSM) [94, 95] is so high that phenomenological analyses often make simplifying assumptions that reduce drastically the number of parameters. One assumption that is frequently employed is that (at least some of) the soft SUSY-breaking parameters are universal at some high input scale, before renormalization. One model based on this simplification is the constrained MSSM (CMSSM), in which all the soft SUSY-breaking scalar masses m_0 are assumed to be universal at the GUT scale, as are the soft SUSY-breaking gaugino masses $m_{1/2}$ and trilinear couplings A_0. The assumption that squarks and sleptons with the same gauge quantum numbers have the same masses is motivated by the absence of identified supersymmetric contributions to flavor-changing neutral interactions and rare decays (see [96] and references therein). Universality between squarks and sleptons with different gauge interactions may be motivated by some GUT scenarios [97]. Other "simplified" versions of the MSSM that are based on (some) unification at a higher scale are (minimal) Gauge mediated SUSY-breaking (mGMSB) [98, 99, 100] and (minimal) Anomaly mediated SUSY-breaking (mAMSB) [101, 102, 103].

One approach to analyze the reduced parameter spaces of the CMSSM, mGMSB, mAMSB or other GUT-based models is a combined χ^2 analysis of electroweak precision observables (EWPO) and of B-physics observables (BPO). Those analyses have yet been restricted to the CMSSM or the non-universal Higgs mass (NUHM) model [104, 105, 106, 107, 108, 109, 110, 111] (see also [112, 113, 114, 115]). In these analyses also the cold dark matter density constraint imposed by WMAP and other cosmological data [116] has been taken into account. In this case the lightest SUSY particle (LSP), assumed to be the lightest neutralino, is required to give rise to the correct amount of cold dark matter (CDM).

The aim of this chapter is to perform a χ^2 analysis to compare the predictions of the CMSSM, mGMSB and mAMSB. The mechanisms to fulfill the CDM constraints are less clear in mGMSB and mAMSB as compared to the CMSSM. In order to treat the three soft SUSY-breaking scenarios on the same footing, we do not impose the CDM constraint in our analysis and scan over the full parameter space of the three models. Concerning the impact of CDM constraints, it should be kept in mind that small modifications of the physics scenario that concern neither the theory basis nor the collider phenomenology could have a strong impact on the CDM derived bounds. If the amount of CDM appears to be too small, other DM candidates can provide the necessary amount to reach the measured density (see also [117] for a recent analysis). If, on the other hand, the CDM density appears to be too large, a small amount of R-parity violation [118], not affecting the collider phenomenology, could remove the CDM bound completely. Other possibilities not invoking R-parity violation are “thermal inflation” [119] or “late-time entropy injection” [120]. They could offer a mechanism for bringing a high CDM density into agreement with the WMAP measurements. Applying the WMAP constraints always assumes “standard cosmology”. Therefore the choice of not imposing the CDM constraints, as we do, can be motivated in the wider class of models under investigation here. We have checked for the CMSSM that previous results could be reproduced when including the CDM constraint.

The set of EWPO included in our analysis is the W boson mass M_W, the effective leptonic weak mixing angle $\sin^2\theta_{eff}$, the anomalous magnetic moment of the muon $(g-2)_\mu$, and the mass of the lightest CP-even MSSM Higgs boson M_h. In addition, we also include two BPO: the branching ratios BR($b \to s\gamma$) and BR($B_s \to \mu^+\mu^-$). Other BPO such as BR($B_u \to \tau\nu_\tau$) and the B_s mass mixing parameter ΔM_{B_s} have shown to possess only a low sensitivity with the current precision in this kind of χ^2 analysis [106]. For the evaluation of the BPO we assume minimal flavor violation (MFV) at the electroweak scale. Non-minimal flavor violation (NMFV) effects can be induced by RGE running from the high scale, see e.g. [121], that may amount to $\sim$ 10% of the SUSY corrections. These additional contributions are neglected throughout our study. For each observable, we construct the χ^2 function including both theoretical and experimental systematic uncertainties, as well as statistical errors. Our analysis should be seen as an exploratory study, with the main goal to compare the three soft SUSY-breaking scenarios. A more elaborate investigation using more precision data and a refined χ^2 analysis, see e.g. [111], can be performed in a later stage and is beyond the scope of this chapter.

The rest of the chapter is organized as follows. We first briefly review the three soft SUSY-breaking scenarios and the investigated parameter space. In 3.3 we shortly describe the current status of the EWPO and BPO that we use, our treatment of the available theoretical calculations and their uncertainties, as well as their present experimental values. The analysis within the three soft SUSY-breaking scenarios using current experimental data can be found in 3.4. In a final step we assume an improvement of the various EWPO and BPO accuracies from future experimental data and theory calculations and analyze in 3.5 the improvement in the parameter determination. The conclusions can be found in 3.6.

3.2 The Soft SUSY-breaking Scenarios

The fact that no SUSY partners of the SM particles have so far been observed means that low-energy SUSY cannot be realized as an unbroken symmetry in nature, and SUSY models thus have to incorporate additional Supersymmetry breaking interactions. This is achieved by adding to the Lagrangian (defined by the $\mathrm{SU}(3)_C \times \mathrm{SU}(2)_L \times \mathrm{U}(1)_Y$ gauge symmetry and the superpotential W) some further interaction terms that respect the gauge symmetry but break Supersymmetry (softly, i.e. no quadratic divergences appear), so called "soft SUSY-breaking" (SSB) terms. Assuming that the R-parity symmetry [118] is conserved, which we do in this study for all SUSY breaking scenarios, reduces the amount of new soft terms allowed in the Lagrangian. Choosing a particular soft SUSY-breaking pattern allows further reduction of the number of free parameters and the construction of predictive models. The three most prominent scenarios for such models are

- **CMSSM** (constrained Minimal Supersymmetric Standard Model) [122, 123]: Apart from the SM parameters (for the experimental values of the SM input parameters we use [124]), 4 parameters and a sign are required to define the CMSSM scenario:

  $$\{\ m_0\ ,\ m_{1/2}\ ,\ A_0\ ,\ \tan\beta\ ,\ \mathrm{sign}(\mu)\ \}\ . \tag{3.1}$$

  While m_0, $m_{1/2}$ and A_0 define the scalar and fermionic masses and the trilinear couplings at the GUT scale ($\sim 10^{16}$ GeV), $\tan\beta$ (the ratio of the two vacuum expectation values) and the sign(μ) (μ is the supersymmetric Higgs mass parameter) are defined at the low-energy scale. For our numerical analyses, see Sects. 3.4 and 3.5, we have scanned over the following parameter space

  $$\begin{aligned} 50\ \mathrm{GeV} \leq \quad & m_0 && \leq 2\ \mathrm{TeV}\ , \\ 50\ \mathrm{GeV} \leq \quad & m_{1/2} && \leq 2\ \mathrm{TeV}\ , \\ -3\ \mathrm{TeV} \leq \quad & A_0 && \leq 3\ \mathrm{TeV}\ , \\ 1.5 \leq \quad & \tan\beta && \leq 60\ , \\ & \mathrm{sign}\,\mu && = \pm 1. \end{aligned} \tag{3.2}$$

- **mGMSB** (minimal Gauge Mediated SUSY-Breaking) [100]: A very promising alternative to the CMSSM is based on the hypothesis that the soft SUSY-breaking occurs at relatively low energy scales and is mediated mainly by gauge interactions through the so-called "messenger sector" [98, 99, 100, 125, 126]. Also in this scenario, the low-energy parameters depend on 4 parameters and a sign,

$$\{\ M_{\rm mess},\ N_{\rm mess},\ \Lambda,\ \tan\beta,\ {\rm sign}(\mu)\ \}\ , \tag{3.3}$$

where $M_{\rm mess}$ is the overall messenger mass scale; $N_{\rm mess}$ is a number called the messenger index, parameterizing the structure of the messenger sector; Λ is the universal soft SUSY-breaking mass scale felt by the low-energy sector. The phenomenology of mGMSB is characterized by the presence of a very light gravitino $\tilde{G}$ with mass given by $m_{3/2} = m_{\tilde{G}} = \frac{F}{\sqrt{3}M'_P} \simeq \left(\frac{\sqrt{F}}{100\ {\rm TeV}}\right)^2 2.37$ eV [127], where $\sqrt{F}(\sim M_{\rm mess})$ is the fundamental scale of SSB and $M'_P = 2.44 \times 10^{18}$ GeV is the reduced Planck mass. Since $\sqrt{F}$ is typically of order 100 TeV, the $\tilde{G}$ is always the LSP in these theories. The numerical analysis in Sects. 3.4 and 3.5 is based on the following scatter ranges:

$$\begin{aligned} 10^4\ {\rm GeV} \leq &\quad \Lambda &&\leq 2\,\times\,10^5\ {\rm GeV}\ , \\ 1.01\,\Lambda \leq &\quad M_{\rm mess} &&\leq 10^5\,\Lambda\ , \\ 1 \leq &\quad N_{\rm mess} &&\leq 8\ , \\ 1.5 \leq &\quad \tan\beta &&\leq 60\ , \\ &\quad {\rm sign}\,\mu &&= \pm 1. \end{aligned} \tag{3.4}$$

Values of $N_{\rm mess}$ larger than ~ 8 result in problems with perturbativity of the gauge interactions at very high scales [100].

- **mAMSB** (minimal Anomaly Mediated SUSY-Breaking) [101, 102, 103]:
  In this model, SUSY breaking happens on a separate brane and is communicated to the visible world via the super-Weyl anomaly. The particle spectrum is determined by 3 parameters and a sign:

$$\{m_{\rm aux},\ m_0,\ \tan\beta,\ {\rm sign}(\mu)\}. \tag{3.5}$$

The overall scale of SUSY particle masses is set by $m_{\rm aux}$, which is the vacuum expectation value of the auxiliary field in the supergravity multiplet. m_0 is introduced as a phenomenological parameter to avoid negative slepton mass squares, for other approaches to this problem see [101, 128, 129, 130, 131]. The scatter parameter space for the numerical analysis in Sects. 3.4 and 3.5 is chosen to be

$$\begin{aligned} 20\text{ TeV} \leq \quad m_{\text{aux}} &\leq 200\text{ TeV}, \\ 0 \leq \quad m_0 &\leq 2\text{ TeV}, \\ 1.5 \leq \quad \tan\beta &\leq 60, \\ \operatorname{sign}\mu &= \pm 1. \end{aligned} \tag{3.6}$$

The upper bound on m_0 has been chosen in agreement with the CMSSM scenario. Concerning m_{aux}, being linked to the SUSY-breaking scale, we have chosen the upper bound of 200 TeV, which should be sufficient to cover the essential features of the low-energy spectrum of mAMSB.

The low-energy spectra for all soft SUSY-breaking scenarios have been evaluated with the program `SoftSUSY` [132] (version `2.0`), taking into account the experimental constraints from SUSY particle searches [124]. The parameter ranges have been sampled by a random scan over the four- (three-)dimensional space of the free parameters in the CMSSM and mGMSB (in mAMSB). The sign of μ has been treated as another free parameter. For each soft SUSY-breaking scenario about $\sim 10^5$ random points have been generated. This large number ensures that all regions of the four- (three-)dimensional hypercube of free parameters are reached.

3.3 The Precision Observables

The considered data set includes four EWPO [133]: the mass of the W boson, M_W, the effective leptonic weak mixing angle, $\sin^2\theta_{\text{eff}}$, the anomalous magnetic moment of the muon, $(g-2)_\mu$, and the mass of the lightest CP-even MSSM Higgs boson, M_h. Another EWPO, the total Z boson width, Γ_Z, has shown to have little sensitivity to SUSY corrections [106, 134]. In addition, we include two BPO: the branching ratios $\text{BR}(b \to s\gamma)$ and $\text{BR}(B_s \to \mu^+\mu^-)$. Other BPO such as $\text{BR}(B_u \to \tau\nu_\tau)$ and the

B_s mass-mixing parameter ΔM_{B_s} with their current experimental and theoretical precision have only a small sensitivity to SUSY corrections [106].

In this Section we start our analysis by recalling the current precisions of the experimental results and the theoretical predictions for all these observables. In the following, we refer to the theoretical uncertainties from unknown higher-order corrections as 'intrinsic' theoretical uncertainties and to the uncertainties induced by the experimental errors of the SM input parameters as 'parametric' theoretical uncertainties. We do not discuss here the theoretical uncertainties in the renormalization-group running between the high-scale input parameters and the weak scale. At present, these uncertainties are less important than the experimental and theoretical uncertainties in the precision observables.

Assuming that the six observables listed above are uncorrelated, a χ^2 fit has been performed with

$$\chi^2 \equiv \sum_{n=1}^{4} \left(\frac{R_n^{\rm exp} - R_n^{\rm theo}}{\sigma_n} \right)^2 + \chi^2_{M_h} + \chi^2_{B_s}. \tag{3.7}$$

Here $R_n^{\rm exp}$ denotes the experimental central value of the nth observable (M_W, $\sin^2\theta_{\rm eff}$, $(g-2)_\mu$ and $\text{BR}(b \to s\gamma)$), $R_n^{\rm theo}$ is the corresponding MSSM prediction and σ_n denotes the combined error, as specified below. $\chi^2_{M_h}$ and $\chi^2_{B_s}$ denote the χ^2 contribution coming from the experimental limits on the lightest CP-even MSSM Higgs boson mass and on $\text{BR}(B_s \to \mu^+\mu^-)$, respectively, which are also described below. In Sect. 3.5 we assume a future measurement of M_h and use $\chi^2_{M_h} = ((M_h^{\rm exp} - M_h^{\rm theo})/\sigma_{M_h})^2$.

We also list below the parametric uncertainties in the predictions on the observables induced by the experimental uncertainties of all relevant SM input parameters. These parametric uncertainties are then added to the other errors (intrinsic and experimental) of the observables as described in the text below. A particularly important input parameter in this respect is the top-quark mass. We evaluate the SUSY spectrum and the observables for each data point for the nominal value, $m_t = 171.4$ GeV [135] but include the error induced by the experimental uncertainty of $\delta m_t^{\rm exp} = 2.1$ GeV.[1]

3.3.1 The W Boson Mass

The W boson mass can be evaluated from

$$M_W^2 \left(1 - \frac{M_W^2}{M_Z^2}\right) = \frac{\pi\alpha}{\sqrt{2}G_F}\left(1 + \Delta r\right), \tag{3.8}$$

where α is the fine structure constant and G_F the Fermi constant. The radiative corrections are summarized in the quantity Δr [137]. The prediction for M_W within the SM or the MSSM is obtained by evaluating Δr in these models and solving eq. (3.8) for M_W.

We include the complete one-loop result in the MSSM [138, 139] as well as higher-order QCD corrections of SM type that are of $\mathcal{O}(\alpha\alpha_s)$ [140, 141] and $\mathcal{O}(\alpha\alpha_s^2)$ [142, 143], where $\alpha_s = g_s^2/(4\pi)$. Furthermore, we incorporate supersymmetric corrections of $\mathcal{O}(\alpha\alpha_s)$ [144] and of $\mathcal{O}(\alpha_t^2)$ [145] to the quantity $\Delta\rho$, which involves the leading universal corrections induced by the mass splitting between fields in an isospin doublet [146]. [2] Here $\alpha_t = y_t^2/(4\pi)$ in terms of the coupling of the Higgs to the top quark.

The remaining intrinsic theoretical uncertainty in the prediction for M_W within the MSSM is still significantly larger than in the SM. For typical parameters (based on Ref. [145]) we estimate the current and future intrinsic uncertainties to be

$$\Delta M_W^{\rm intr,current} \lesssim 10 \text{ MeV} , \quad \Delta M_W^{\rm intr,future} = 2 \text{ MeV} , \tag{3.9}$$

depending on the mass scale of the supersymmetric particles. The parametric uncertainties are dominated by the experimental error of the top-quark mass and the hadronic contribution to the shift in the fine structure constant. Their current errors

---

[1] Using the most recent experimental value, $m_t = 172.6$ GeV, including the experimental error of $\delta m_t^{\rm exp} = 1.4$ GeV [136], see below, would have a relatively small impact on our analysis, see also the discussion at the end of Sect. 3.4.2.

[2] A recent re-evaluation of M_W [147] shows good agreement with the values used here.

induce the following parametric uncertainties [106, 133]

$$\delta m_t^{\rm current} = 2.1 \text{ GeV} \;\;\Rightarrow\;\; \Delta M_W^{{\rm para},m_t,{\rm current}} \approx 13 \text{ MeV}, \tag{3.10}$$

$$\delta(\Delta\alpha_{\rm had}^{\rm current}) = 35 \times 10^{-5} \;\;\Rightarrow\;\; \Delta M_W^{{\rm para},\Delta\alpha_{\rm had},{\rm current}} \approx 6.3 \text{ MeV} . \tag{3.11}$$

At the ILC, the top-quark mass will be measured with an accuracy of about 100 MeV [148, 149]. The parametric uncertainties induced by the future experimental errors of m_t and $\Delta\alpha_{\rm had}$ [150] will then be [151]

$$\delta m_t^{\rm future} = 0.1 \text{ GeV} \;\;\Rightarrow\;\; \Delta M_W^{{\rm para},m_t,{\rm future}} \approx 1 \text{ MeV}, \tag{3.12}$$

$$\delta(\Delta\alpha_{\rm had}^{\rm future}) = 5 \times 10^{-5} \;\;\Rightarrow\;\; \Delta M_W^{{\rm para},\Delta\alpha_{\rm had},{\rm future}} \approx 1 \text{ MeV}. \tag{3.13}$$

The present experimental value of M_W is [152, 153, 154, 155, 156], see also Ref. [157].

$$M_W^{\rm exp,current} = 80.398 \pm 0.025 \text{ GeV}. \tag{3.14}$$

With the GigaZ option of the ILC (i.e. high-luminosity running at the Z resonance and the WW threshold) the W-boson mass will be determined with an accuracy of about [158, 159]

$$\delta M_W^{\rm exp,future} = 7 \text{ MeV}. \tag{3.15}$$

We add the experimental and theoretical errors for M_W (for the current situation as well as for the future estimates) in quadrature in our analysis.

The predictions for M_W in the three scenarios are compared with each other in Fig. 3.3.1 (for $\mu > 0$, see Sect. 3.3.3), where the W boson mass is shown as a function of the lighter scalar top quark mass, $m_{\tilde{t}_1}$. The shown areas are obtained as the borders of the scan over the parameters as specified in eqs. (3.2), (3.4) and (3.6). The upper limit of $m_{\tilde{t}_1}$ reached in the three scenarios is similar in the CMSSM and in mAMSB (related to the upper bounds on $m_{1/2}$ and $m_{\rm aux}$), whereas the allowed area for $m_{\tilde{t}_1}$ is somewhat larger in mGMSB. Since these upper bounds depend on the chosen ranges for the high-energy scale parameters, they should be considered to be artificial and it does not make sense to compare the three soft SUSY-breaking scenarios in these terms. Consequently, we have truncated the plot at $m_{\tilde{t}_1} = 3$ TeV.

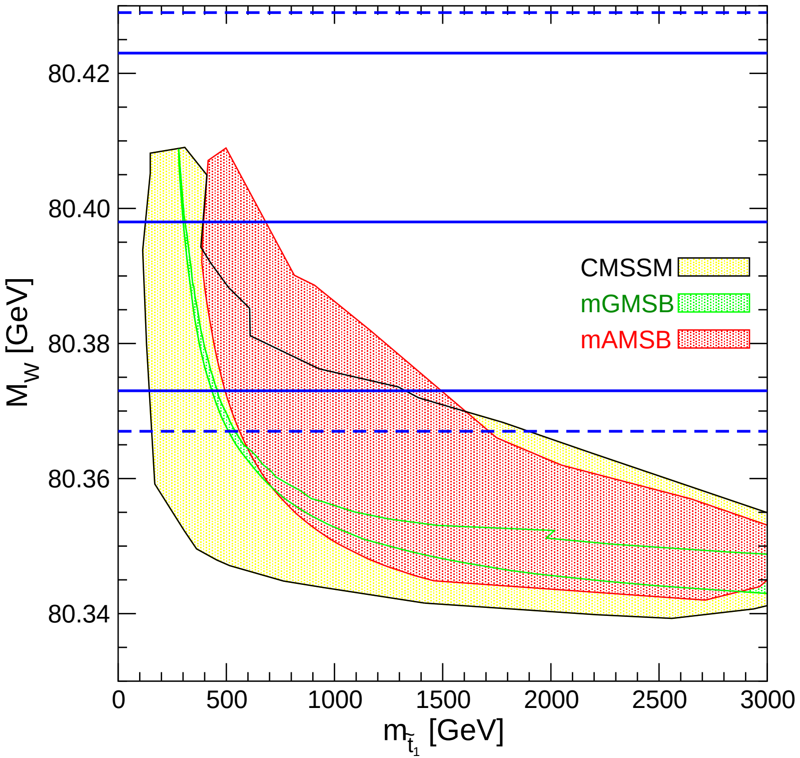

Figure 3.1: The predictions for M_W as obtained from the parameter scan are shown as a function of $m_{\tilde{t}_1}$ for the three soft SUSY-breaking scenarios for $\mu > 0$. The top quark mass has been fixed to $m_t = 171.4$ GeV. The solid (dashed) lines indicate the currently allowed $1\,\sigma$ interval from the experimental uncertainty (including also theoretical uncertainties).

The range of the M_W prediction is very similar in the three scenarios. The solid (dashed) lines represent the currently allowed $1\,\sigma$ interval from the experimental uncertainty (including also theoretical uncertainties). This indicates that at the current level of accuracy all three models agree similarly well with the experimental measurement. A preference for relatively low values of $m_{\tilde{t}_1}$ is visible, which is most prominent in mGMSB.

3.3.2 The Effective Leptonic Weak Mixing Angle

The effective leptonic weak mixing angle at the Z boson peak can be written as

$$\sin^2\theta_{\text{eff}} = \frac{1}{4}\left(1 - \text{Re}\,\frac{v_{\text{eff}}}{a_{\text{eff}}}\right) , \tag{3.16}$$

where $v_{\rm eff}$ and $a_{\rm eff}$ denote the effective vector and axial couplings of the Z boson to charged leptons. Our theoretical prediction for $\sin^2\theta_{\rm eff}$ contains the same class of higher-order contributions as described in Sect. 3.3.1, supplemented with a small correction based on Ref. [134], see the evaluation in Ref. [106].

For the intrinsic theoretical uncertainty in the prediction for $\sin^2\theta_{\rm eff}$ we use an estimate (based on Refs. [145, 106, 160]) of

$$\Delta\sin^2\theta_{\rm eff}^{\rm intr,current} \lesssim 12\times10^{-5}\ , \quad \Delta\sin^2\theta_{\rm eff}^{\rm intr,future} \lesssim 2\times10^{-5}\ . \qquad (3.17)$$

The experimental errors of m_t and $\Delta\alpha_{\rm had}$ induce the following parametric uncertainties [134]

$$\delta m_t^{\rm current} = 2.1 \text{ GeV} \;\Rightarrow\; \Delta\sin^2\theta_{\rm eff}^{{\rm para},m_t,{\rm current}} \approx 6.3\times10^{-5}, \qquad (3.18)$$

$$\delta(\Delta\alpha_{\rm had}^{\rm current}) = 35\times10^{-5} \;\Rightarrow\; \Delta\sin^2\theta_{\rm eff}^{{\rm para},\Delta\alpha_{\rm had},{\rm current}} \approx 12\times10^{-5}. \qquad (3.19)$$

For the future accuracies we assume

$$\delta m_t^{\rm future} = 0.1 \text{ GeV} \;\Rightarrow\; \Delta\sin^2\theta_{\rm eff}^{{\rm para},m_t,{\rm future}} \approx 0.4\times10^{-5}, \qquad (3.20)$$

$$\delta(\Delta\alpha_{\rm had}^{\rm future}) = 5\times10^{-5} \;\Rightarrow\; \Delta\sin^2\theta_{\rm eff}^{{\rm para},\Delta\alpha_{\rm had},{\rm future}} \approx 1.8\times10^{-5}. \qquad (3.21)$$

The experimental value is [152, 153][3]

$$\sin^2\theta_{\rm eff}^{\rm exp,current} = 0.23153 \pm 0.00016\ . \qquad (3.22)$$

The experimental accuracy will improve to about

$$\delta\sin^2\theta_{\rm eff}^{\rm exp,future} = 1.3\times10^{-5}. \qquad (3.23)$$

at GigaZ [161] (see also Ref. [162] for a corresponding discussion). We add the experimental and theoretical errors for $\sin^2\theta_{\rm eff}$ in quadrature in our analysis.

---

[3] It should be noted that this value is determined mostly by two measurements that are only marginally compatible: the forward-backward asymmetry for b quarks $A_{\rm FB}^b$, and the left-right asymmetry for electrons $A_{\rm LR}^e$ [152].

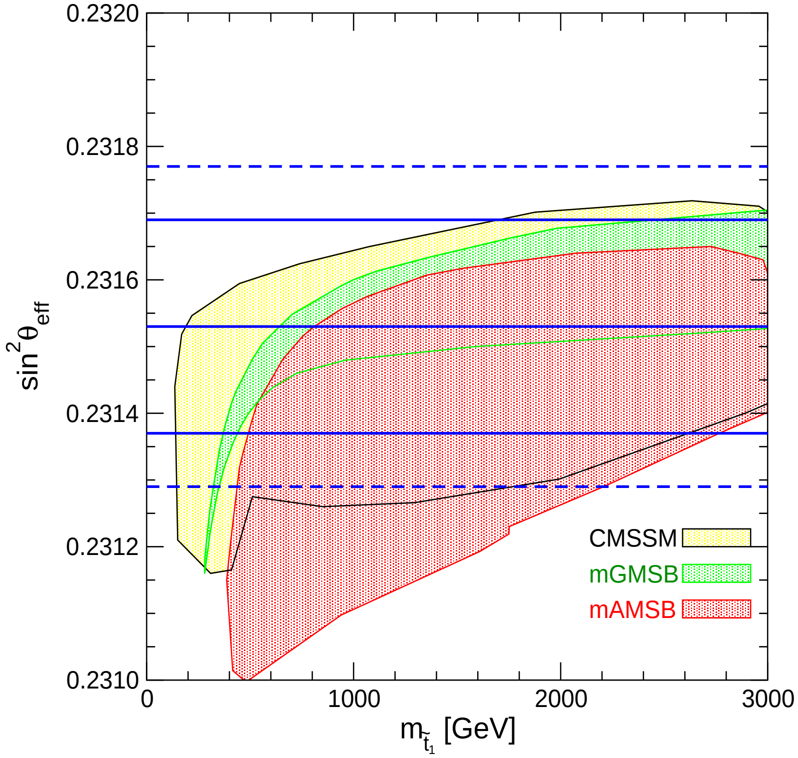

Figure 3.2: The predictions for $\sin^2\theta_{\text{eff}}$ as obtained from the parameter scan are shown as a function of $m_{\tilde{t}_1}$ for the three soft SUSY-breaking scenarios for $\mu > 0$. The top quark mass has been fixed to $m_t = 171.4$ GeV. The solid (dashed) lines indicate the currently allowed $1\,\sigma$ interval from the experimental uncertainty (including also theoretical uncertainties).

The predictions for $\sin^2\theta_{\text{eff}}$ in the three scenarios are compared with each other in Fig. 3.2 (for $\mu > 0$, see Sect. 3.3.3), where the effective weak mixing angle is shown as a function of the lighter scalar top quark mass, $m_{\tilde{t}_1}$ (truncated at $m_{\tilde{t}_1} =$ 3 TeV). As for M_W, the range of the $\sin^2\theta_{\text{eff}}$ prediction is very similar in the three scenarios. Smallest values are reached in mAMSB. The solid (dashed) lines indicate the currently allowed $1\,\sigma$ interval from the experimental uncertainty (including also theoretical uncertainties). This indicates, as for M_W, that at the current level of accuracy all three models agree equally well with the experimental data, where no preference for $m_{\tilde{t}_1}$ can be deduced.

3.3.3 The Anomalous Magnetic Moment of the Muon

The SM prediction for the anomalous magnetic moment of the muon, $a_\mu = \frac{1}{2}(g-2)_\mu$, (see Refs. [163, 164, 165, 166, 167, 168] for reviews) depends in particular on the evaluation of QED contributions (see Refs. [169, 170, 171] for recent updates), the hadronic vacuum polarization and light-by-light (LBL) contributions. The former have been evaluated in Refs. [172, 173, 174, 175, 167, 176, 177] and the latter in Refs. [178, 179, 180, 181]. The evaluations of the hadronic vacuum polarization contributions using e^+e^- and τ decay data give somewhat different results. In view of the fact that recent e^+e^- measurements tend to confirm earlier results, whereas the correspondence between previous τ data and preliminary data from BELLE [182] is not so clear, and also in view of the additional uncertainties associated with the isospin transformation from τ decay (see Ref. [183]), we use here the latest estimate based on e^+e^- data [177]:

$$a_\mu^{\text{theo}} = (11\,659\,180.5 \pm 4.4_{\text{had}} \pm 3.5_{\text{LBL}} \pm 0.2_{\text{QED+EW}}) \times 10^{-10}, \tag{3.24}$$

where the source of each error is labeled. We note that the more recent e^+e^- data sets of Refs. [184, 185, 186, 187] have been partially included in the updated estimate of $(g-2)_\mu$.

The SM prediction is to be compared with the final result of the Brookhaven $(g-2)_\mu$ experiment E821 [188, 189], namely:

$$a_\mu^{\text{exp}} = (11\,659\,208.0 \pm 6.3) \times 10^{-10}, \tag{3.25}$$

leading to an estimated discrepancy [177, 190]

$$a_\mu^{\text{exp}} - a_\mu^{\text{theo}} = (27.5 \pm 8.4) \times 10^{-10}, \tag{3.26}$$

equivalent to a 3.3-σ effect[4]. While it would be premature to regard this deviation as a firm evidence for new physics, within the context of SUSY, it does indicate a preference for a non-zero contribution from superpartners.

---

[4] Three other recent evaluations yield slightly different numbers [167, 174, 166], but similar discrepancies with the SM prediction.

Concerning the MSSM contribution, the complete one-loop result was evaluated over a decade ago [191]. In view of the correlation between the signs of $(g-2)_\mu$ and of μ [192], variants of the MSSM with $\mu < 0$ (or more precisely a positive $\mu \cdot M_2$, where we use the convention of positive M_2 for the three scenarios) are already severely challenged by the present data on a_μ. However, as indicated in Sect. 3.2, we have analyzed both signs of μ, and correspondingly find a strong preference for $\mu > 0$, see Fig. 3.3 below. Therefore, in the other plots shown here we focus on the case $\mu > 0$.

In addition to the full one-loop contributions, the leading QED two-loop corrections have also been evaluated [193]. Further corrections at the two-loop level have been obtained more recently [194, 195], leading to corrections to the one-loop result that are $\lesssim 10\%$. These corrections are taken into account in our analysis according to the approximate formulas given in Refs. [194, 195].

The current intrinsic uncertainties in the SUSY contributions to a_μ can be estimated to be $\lesssim 1 \times 10^{-10}$ [165]. We assume that in the future the uncertainty in eq. (3.26) will be reduced by a factor two. All errors are added in quadrature.

The predictions for $\Delta a_\mu^{\rm SUSY}$ in the three scenarios are compared with each other in Fig. 3.3, where the anomalous magnetic moment of the muon is shown as a function of the lighter scalar top quark mass, $m_{\tilde{t}_1}$ (truncated at $m_{\tilde{t}_1} = 3$ TeV). The full (dot) shaded areas are obtained for $\mu > (<)0$, resulting in $\Delta a_\mu^{\rm SUSY} > (<)0$. The range of the a_μ prediction is very similar in the three scenarios. The solid (dashed) lines indicate the currently allowed $1(2)\,\sigma$ intervals of the experimental uncertainty. It becomes apparent that points with $\mu < 0$ are strongly disfavored by the analysis of $(g-2)_\mu$. Furthermore, at the $2\,\sigma$ level stop masses heavier than ~ 2 TeV are clearly disfavored.

3.3.4 The Mass of the Lightest CP-even MSSM Higgs Boson

The mass of the lightest CP-even MSSM Higgs boson can be predicted in terms of the other MSSM parameters. At the tree level, the two CP-even Higgs boson masses are obtained as functions of M_Z, the CP-odd Higgs boson mass M_A, and $\tan\beta$,

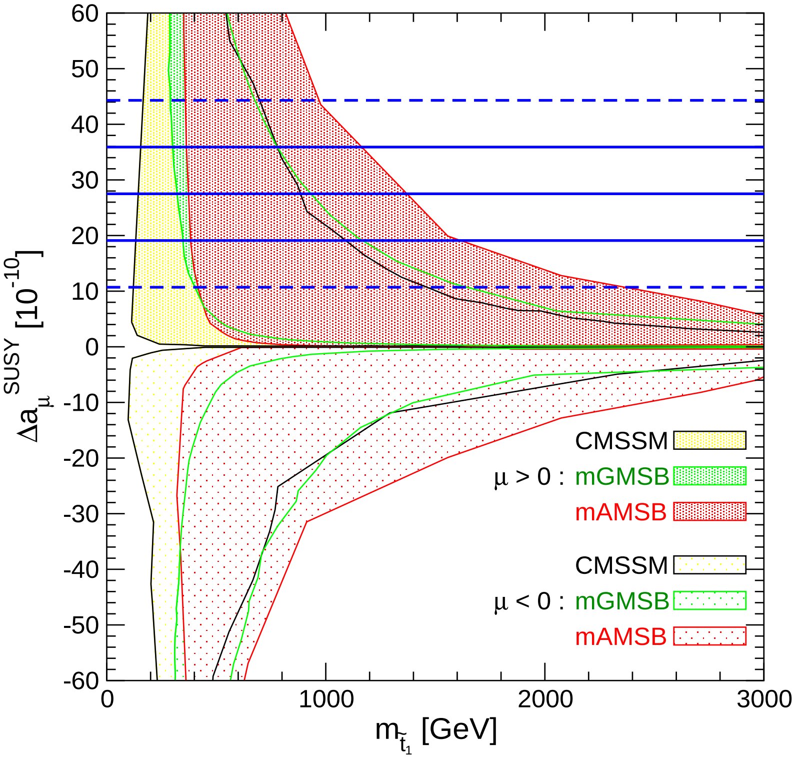

Figure 3.3: The predictions for $\Delta a_\mu^{\rm SUSY}$ as obtained from the parameter scan are shown as a function of $m_{\tilde{t}_1}$ for the three soft SUSY-breaking scenarios. The full (dot) shaded areas are obtained for $\mu > (<)0$, resulting in $\Delta a_\mu^{\rm SUSY} > (<)0$. The top quark mass has been fixed to $m_t = 171.4$ GeV. The solid (dashed) lines indicate the currently allowed $1(2)\,\sigma$ intervals of the experimental uncertainty.

whereas other parameters enter into the loop corrections. We employ the Feynman-diagrammatic method [196, 197] for the theoretical prediction of M_h, using the code `FeynHiggs` [198, 199, 200, 46], which includes all numerically relevant known higher-order corrections. The status of these results can be summarized as follows. For the one-loop part, the complete result within the MSSM is known [201, 196, 202]. Computation of the two-loop effects is quite advanced: see Ref. [200] and references therein. These include the strong corrections at $\mathcal{O}(\alpha_t\alpha_s)$ and Yukawa corrections at $\mathcal{O}(\alpha_t^2)$ to the dominant one-loop $\mathcal{O}(\alpha_t)$ term, and the strong corrections from the bottom/sbottom sector at $\mathcal{O}(\alpha_b\alpha_s)$, where $\alpha_b = y_b^2/(4\pi)$ in terms of the coupling of the Higgs to the bottom quark. In the case of the $b/\tilde{b}$ sector corrections, an all-order resummation of the $\tan\beta$-enhanced terms, $\mathcal{O}(\alpha_b(\alpha_s\tan\beta)^n)$, is also known [203, 204]. More recently, the $\mathcal{O}(\alpha_t\alpha_b)$ and $\mathcal{O}(\alpha_b^2)$ corrections have been derived [205] [5]. The current and future intrinsic error of M_h due to unknown higher-order corrections has been estimated to be [200, 209, 133, 210]

$$\Delta M_h^{\text{intr,current}} = 3 \text{ GeV} , \quad \Delta M_h^{\text{intr,future}} = 0.5 \text{ GeV} . \tag{3.27}$$

The current uncertainty we interpret effectively as a ~ 95 % confidence level limit in the evaluation of the χ^2 contribution, see below.

The by far largest parametric uncertainty is induced by the error in m_t [135] (also slightly depending on the SUSY parameters) see Refs. [133, 211] for details,

$$\begin{aligned} \text{CMSSM} : \delta m_t^{\text{current}} &= 2.1\,(1.4) \text{ GeV} \;\Rightarrow\; \Delta M_h^{\text{para},m_t,\text{current}} = 1.4\,(0.9) \text{ GeV} , \\ \text{mGMSB} : \delta m_t^{\text{current}} &= 2.1\,(1.4) \text{ GeV} \;\Rightarrow\; \Delta M_h^{\text{para},m_t,\text{current}} = 1.5\,(1.0) \text{ GeV} , \\ \text{mAMSB} : \delta m_t^{\text{current}} &= 2.1\,(1.4) \text{ GeV} \;\Rightarrow\; \Delta M_h^{\text{para},m_t,\text{current}} = 1.2\,(0.8) \text{ GeV} . \end{aligned} \tag{3.28}$$

This is already substantially below the current intrinsic uncertainty. The numbers in brackets correspond to the latest m_t measurement [136] and are given for the sake of comparison.

It should be noted that, for the unconstrained MSSM with small values of M_A and values of $\tan\beta$ which are not too small, a significant suppression of the hZZ coupling can occur compared to the SM value, in which case the experimental lower bound on M_h may be more than 20 GeV below the SM value [212] (for the MSSM with real parameters). However, it had been checked that within the CMSSM, mGMSB and mAMSB the hZZ coupling is always very close to the SM value. Accordingly, the bounds from the SM Higgs search at LEP [213] can be taken over directly (see Refs. [214, 215]).

Concerning the χ^2 analysis, we use the complete likelihood information available from LEP. We evaluate the M_h contribution to the overall χ^2 function exactly as

---

[5] A two-loop effective potential calculation has been presented in Ref. [206], including now even the leading three-loop corrections [207], but no public code based on this result is currently available. Most recently another leading three-loop calculation, valid for certain SUSY mass combinations, became available [208].

outlined in Sect. 2.6 of Ref. [106]. This evaluation takes into account the intrinsic uncertainty given in eq. (3.27). The χ^2 contribution is then combined with the corresponding quantities for the other observables we consider, see eq. (3.7).

For the analysis of future sensitivities, see Sect. 3.5, we assume a measurement of the lightest MSSM Higgs boson mass with a precision of [216, 217, 218, 219]

$$\Delta M_h^{\rm exp,future} = 50 \text{ MeV} . \tag{3.29}$$

The future parametric uncertainties are expected to be

$$\delta m_t^{\rm future} = 0.1 \text{ GeV} \quad \Rightarrow \quad \Delta M_h^{{\rm para},m_t,{\rm future}} \approx 0.1 \text{ GeV}, \tag{3.30}$$

$$\delta \alpha_s^{\rm future} = 0.001 \quad \Rightarrow \quad \Delta M_h^{{\rm para},\alpha_s,{\rm future}} \approx 0.1 \text{ GeV}. \tag{3.31}$$

Thus, the intrinsic error, eq. (3.27), would be the dominant source of uncertainty in the future. The errors are added in quadrature, yielding σ_{M_h}, and we use for the analysis of the future sensitivities $\chi^2_{M_h} = ((M_h^{\rm exp} - M_h^{\rm theo})/\sigma_{M_h})^2$.

The predictions for M_h in the three scenarios are compared with each other in Fig. 3.4 (for $\mu > 0$, see Sect. 3.3.3), where the lightest CP-even Higgs boson mass is shown as a function of the lighter scalar top quark mass, $m_{\tilde{t}_1}$ (truncated at $m_{\tilde{t}_1} = 3$ TeV). The SM limit of 114.4 GeV obtained at LEP is indicated with a dashed (blue) line. In each scenario the SM bound from Higgs searches at LEP of $M_h > 114.4$ GeV results in important constraints. On the other hand, the bound is still fulfilled for large parts of the parameter space. No preference for any $m_{\tilde{t}_1}$ can be found.

3.3.5 The Decay $b \to s\gamma$

Since this decay occurs at the loop level in the SM, the MSSM contribution might *a priori* be of similar magnitude. A recent theoretical estimate of the SM contribution to the branching ratio at the NNLO QCD level is [220]

$$\text{BR}(b \to s\gamma) = (3.15 \pm 0.23) \times 10^{-4} . \tag{3.32}$$

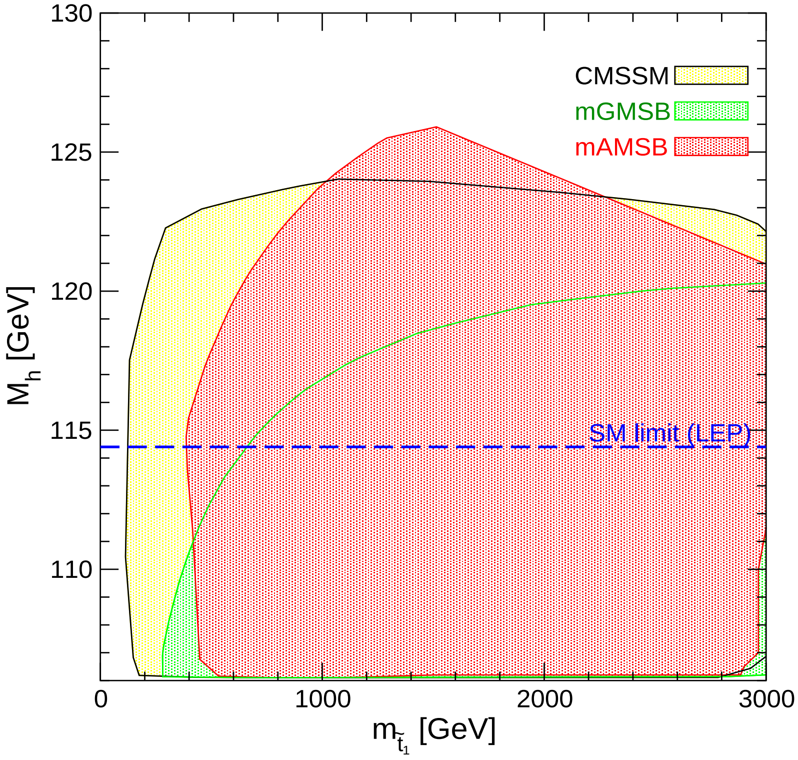

Figure 3.4: The predictions for M_h as obtained from the parameter scan are shown as a function of $m_{\tilde{t}_1}$ for the three soft SUSY-breaking scenarios for $\mu > 0$. The top quark mass has been fixed to $m_t = 171.4$ GeV. The SM lower limit of 114.4 GeV obtained at LEP is indicated with a dashed (blue) line.

We record that the error estimate for BR($b \to s\gamma$) is still under debate [221], and that other SM contributions to $b \to s\gamma$ have been calculated [222]. These corrections are small compared with the theoretical uncertainty quoted in eq. (3.32).

For comparison, the present experimental value estimated by the Heavy Flavour Averaging Group (HFAG) is [223, 96]

$$\mathrm{BR}(b \to s\gamma) = (3.55 \pm 0.24\, {}^{+0.09}_{-0.10} \pm 0.03) \times 10^{-4}, \tag{3.33}$$

where the first error is the combined statistical and uncorrelated systematic uncertainty, and the other two errors are correlated systematic theoretical uncertainties and corrections, respectively.

Our numerical results have been derived with the BR($b \to s\gamma$) evaluation provided in Refs. [224, 225, 226], incorporating also the latest SM corrections provided

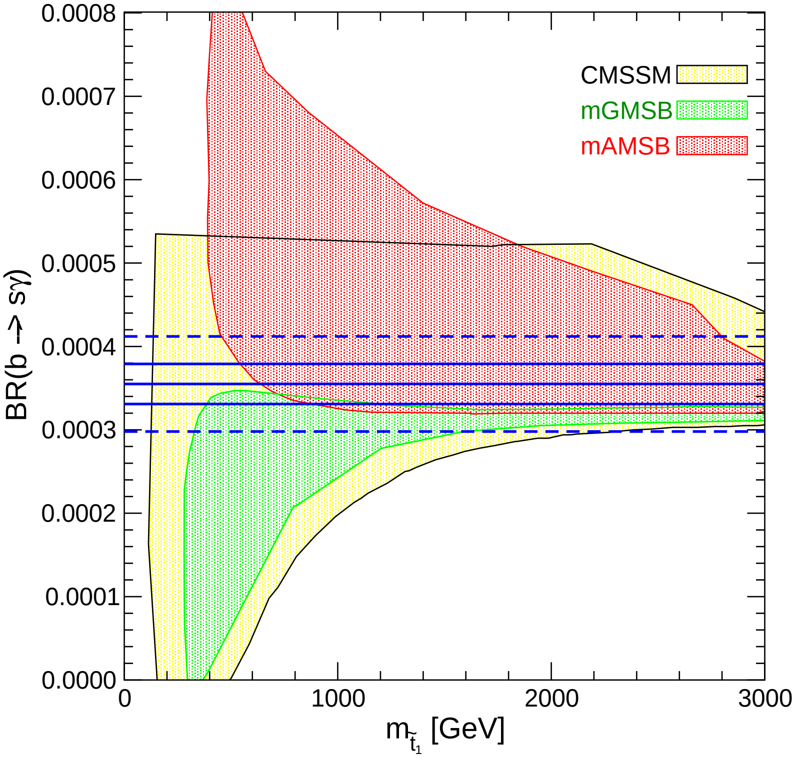

Figure 3.5: The predictions for BR($b \to s\gamma$) as obtained from the parameter scan are shown as a function of $m_{\tilde{t}_1}$ for the three soft SUSY-breaking scenarios for $\mu > 0$. The top quark mass has been fixed to $m_t = 171.4$ GeV. The solid (dashed) lines indicate the currently allowed $1\,\sigma$ interval from the experimental uncertainty (including also theoretical uncertainties, which are added linearly).

in Ref. [220]. The calculation has been checked against other codes [227, 228, 229]. For the evaluation of the BR($b \to s\gamma$), we assume minimal flavor violation (MFV) at the electroweak scale and neglect NMFV effects that can be induced by RGE running from the high scale, see e.g. Ref. [121], that may amount to $\sim 10\%$ of the SUSY corrections.

Concerning the total error in a conservative approach we add linearly the errors of eqs. (3.32) and (3.33) as well an intrinsic SUSY error of 0.15×10^{-4} [106], except the statistical error that is then added in quadrature. For the analysis of the future sensitivities in Sect. 3.5 we assume that the total error will be reduced by a factor of 3.

The predictions for BR($b \to s\gamma$) in the three scenarios are compared with each other in Fig. 3.5 (for $\mu > 0$, see Sect. 3.3.3), where the branching ratio is shown as a function of the lighter scalar top quark mass, $m_{\tilde{t}_1}$ (truncated at $m_{\tilde{t}_1} = 3$ TeV). The solid (dashed) lines indicate the currently allowed $1\,\sigma$ interval from the experimental uncertainty (including also theoretical uncertainties, which are added linearly, see above). In all three scenarios large parts of the parameter space lie within the $1\,\sigma$ interval. However, for small mass scales BR($b \to s\gamma$) provides important constraints on the three models. While the CMSSM and mGMSB can have very small values of BR($b \to s\gamma$) for small $m_{\tilde{t}_1}$[6], mAMSB has typically large values of the BR. The reason can be traced back to the fact that the sign of the stop mixing angle $\theta_{\tilde{t}}$ comes out with a positive sign in mAMSB, whereas it is negative in the CMSSM and mGMSB (as output and in the conventions of `SoftSUSY`). This different sign, in combination with a positive μ, results in a positive SUSY contribution to BR($b \to s\gamma$) within mAMSB and (for most values of the other parameters) a negative contribution in the CMSSM and mGMSB, see also the discussion in the beginning of Sect. 3.4.

3.3.6 The Branching Ratio for $B_s \to \mu^+\mu^-$

The SM prediction for this branching ratio is $(3.4 \pm 0.5) \times 10^{-9}$ [230], and the experimental upper limit from the Fermilab Tevatron collider is 5.8×10^{-8} at the 95% C.L. [231], still providing room for the MSSM to dominate the SM contribution. [7] This Tevatron sensitivity is based on an integrated luminosity of about 2 fb^{-1} collected at CDF. For the χ^2 contribution, in order to incorporate the Tevatron bound, we use a smoothed step function, penalizing data points with BR($B_s \to \mu^+\mu^-$) $> 5.8 \times 10^{-8}$ and preferring lower BRs. [8]

---

[6] Where the BR($b \to s\gamma$) becomes close to zero the calculation of the SUSY corrections is not reliable anymore. However, these parts of the parameter space anyhow result in an experimentally excluded value for BR($b \to s\gamma$).

[7] The upper limit has been improved since when this investigation was finished. See Ref. [232] for the latest update at CDF with an integrated luminosity of 7 fb^{-1}.

[8] In Ref. [232], an experimental error is also reported, which could be used to improve the χ^2 calculation, as oppose to our treatment when this error was not available.

The Tevatron sensitivity is expected to improve significantly in the future. The limit that could be reached at the end of Run II is $\sim 2 \times 10^{-8}$ assuming 8 fb^{-1} collected with each detector [233]. A sensitivity even down to the SM value can be expected at the LHC. Assuming the SM value, i.e. $\text{BR}(B_s \to \mu^+\mu^-) \approx 3.4 \times 10^{-9}$, it has been estimated [234] that LHCb can observe 33 signal events over 10 background events within 3 years of low-luminosity running. Therefore this process offers good prospects for probing the MSSM.

For the theoretical prediction we use results from Ref. [235], which are in good agreement with Ref. [236]. This calculation includes the full one-loop evaluation and the leading two-loop QCD corrections. As in Sect. 3.3.5, we neglect any NMFV effects from RGE running. We do not include $\text{BR}(B_s \to \mu^+\mu^-)$ in our analysis of the future sensitivities (but still require agreement with the current bound), because its impact will strongly depend on the value realized in Nature.

The predictions for $\text{BR}(B_s \to \mu^+\mu^-)$ in the three scenarios are compared with each other in Fig. 3.6 (for $\mu > 0$, see Sect. 3.3.3), where the BR is shown as a function of the lighter scalar top quark mass, $m_{\tilde{t}_1}$ (truncated at $m_{\tilde{t}_1} = 3$ TeV). The current experimental limit of 5.8×10^{-8} is indicated by a dashed (blue) line. Each scenario has large parts of the parameter space with $\text{BR}(B_s \to \mu^+\mu^-) < 5.8 \times 10^{-8}$, where no limit on $m_{\tilde{t}_1}$ is provided by the upper limit on the BR. Within the mGMSB scenario, due to its generally larger M_A values (see below), hardly any points are ruled out by the current upper bound on the BR, while for the other two scenarios $\text{BR}(B_s \to \mu^+\mu^-)$ is already a strong constraint on the parameter space. We have checked that including the CDM constraint and restricting to values of $\tan\beta \leq 50$ the results for $\text{BR}(B_s \to \mu^+\mu^-)$ in Refs. [104, 105, 106] are reproduced.

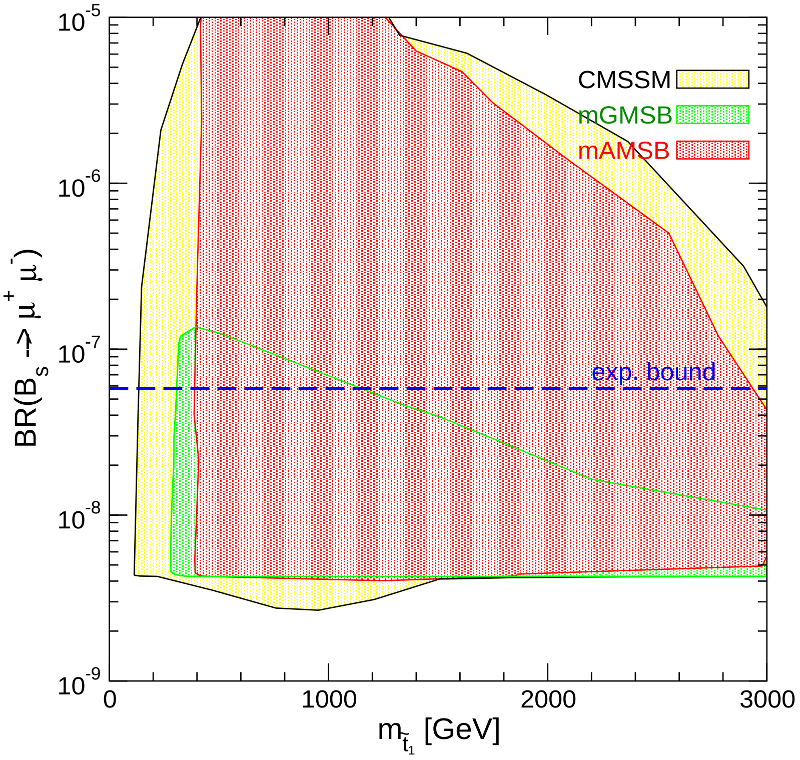

Figure 3.6: The predictions for $\mathrm{BR}(B_s \to \mu^+\mu^-)$ as obtained from the parameter scan are shown as a function of $m_{\tilde{t}_1}$ for the three soft SUSY-breaking scenarios for $\mu > 0$. The top quark mass has been fixed to $m_t = 171.4$ GeV. The current upper limit of 5.8×10^{-8} is indicated by a dashed (blue) line.

3.4 χ^2 Analysis of CMSSB, mGMSB, mAMSB

In this section we present our numerical analysis, based on the χ^2 evaluation as given in eq. (3.7). The best fit point is given by the lowest χ^2 value. The sensitivities are shown as $\Delta\chi^2 = 1, 4, 9$, referred to as Δ_1, Δ_4 and Δ_9, respectively. They give an indication of the precision that has been reached so far for the observables under investigation. Sometimes we refer to the Δ_4 areas as 'preferred' regions. The lowest χ^2 values for the three scenarios are given in Tab. 3.1. Also shown are the individual contributions from the precision observables. $\mathrm{BR}(B_s \to \mu^+\mu^-)$ always gives a zero contribution, and we list the BR itself.

It is interesting to note that despite the fact that mAMSB has one less parameter, the minimum χ^2 value is lower by ~ 1.5–2 compared to the CMSSM and mGMSB.

The reason for the low χ^2 values is a combination of two effects. First, there is a good agreement of mAMSB with $(g-2)_\mu$ and $\mathrm{BR}(b \to s\gamma)$. The anomalous magnetic moment of the muon requires a positive μ (or more precisely a positive $\mu \cdot M_2$, where we use the convention of positive M_2 for the three scenarios, see the discussion above). $\mathrm{BR}(b \to s\gamma)$ on the other hand depends on the combinations of the stop masses, mixing angle and μ. The sign of the stop mixing angle $\theta_{\tilde{t}}$ comes out with a positive sign in mAMSB, whereas it is negative in the CMSSM and mGMSB (as output and in the convention of `SoftSUSY`). This different sign, in combination with a positive μ, results in a positive SUSY contribution to $\mathrm{BR}(b \to s\gamma)$ within mAMSB and a (usually) negative contribution in the CMSSM and mGMSB. In this way mAMSB can fulfill the $\mathrm{BR}(b \to s\gamma)$ constraint as well as the other two scenarios (but with a best-fit value *above* the experimental value). Second, due to the structure of the soft SUSY-breaking parameters in the chargino/neutralino sector relatively light charginos are present in mAMSB (where the lightest one is nearly mass degenerate with the lightest neutralino). Thus a large contribution to $(g-2)_\mu$ and also to M_W [147] can be obtained for a relatively heavier spectrum otherwise, resulting in an M_h value above $\sim$ 116 GeV. The overall effect of this interplay is a total minimum χ^2 value of 2.9.

In the analysis presented below, in the first step we show the three soft SUSY-breaking scenarios separately in terms of their high-scale parameters. In a second step we compare their respective predictions in terms of the low-scale parameters M_A and $\tan\beta$ and other SUSY mass scales. In the final step in Sect. 3.5 we assume future precisions for the measurements and theory evaluations and compare the sensitivities the precision observables will offer in the three scenarios.

3.4.1 Analysis of High-scale Parameters

In the following subsections we analyze the CMSSM, mGMSB and mAMSB in terms of their respective high-energy parameters, see Sect. 3.2.

	CMSSM	mGMSB	mAMSB
$\chi^2_{\rm min}$	4.6	5.1	2.9
M_W	1.7	2.1	0.6
$\sin^2\theta_{\rm eff}$	0.1	0.0	0.8
$(g-2)_\mu$	0.6	0.9	0.0
$\mathrm{BR}(b \to s\gamma)$	1.1	2.0	1.5
M_h	1.1	0.1	0.0
$\mathrm{BR}(B_s \to \mu^+\mu^-)$	4.5×10^{-8}	3.2×10^{-8}	0.4×10^{-8}
M_A [GeV] (best-fit)	394	547	616
$\tan\beta$ (best-fit)	54	55	9

Table 3.1: Minimum χ^2 values for the three soft SUSY-breaking scenarios using today's accuracies for the experimental and theoretical precisions. We also show the individual contributions for M_W, $\sin^2\theta_{\rm eff}$, $(g-2)_\mu$, $\mathrm{BR}(b \to s\gamma)$ and M_h, as well as the value of $\mathrm{BR}(B_s \to \mu^+\mu^-)$. Shown in the last two rows are the best-fit values for the low-energy parameters, M_A and $\tan\beta$, as analyzed in Sect. 3.4.2.

CMSSM

In Fig. 3.7 we show the results for the $\Delta_{1,4,9}$ areas in terms of the high-energy parameters, using the current experimental and theoretical precisions as described in Sect. 3.3. The Δ_1 area is medium shaded (green), the Δ_4 are is dark shaded (red), and the Δ_9 area is light shaded (yellow). The rest of the scanned parameter space is given in black shading. The best-fit point is marked with a circle. Because of the contribution to $(g-2)_\mu$ only very few points with $\mu < 0$ have $\Delta\chi^2 < 9$, and we concentrate here on the data with $\mu > 0$. For this sign of μ the Δ_9 area nearly covers the whole parameter space (in agreement with the results presented in Ref. [106]). In terms of $m_{1/2}$ relatively low values are favored around $m_{1/2} =$ 500 GeV, with the Δ_4 region extending up to $m_{1/2} = 1000$ GeV. For m_0, on the other hand, hardly any bound is obtained, and values up to 2000 GeV are possible. Only at the Δ_1 level a preference of the allowed values for a light m_0 can be found. For A_0 a slight preference for positive values can be observed (note the different

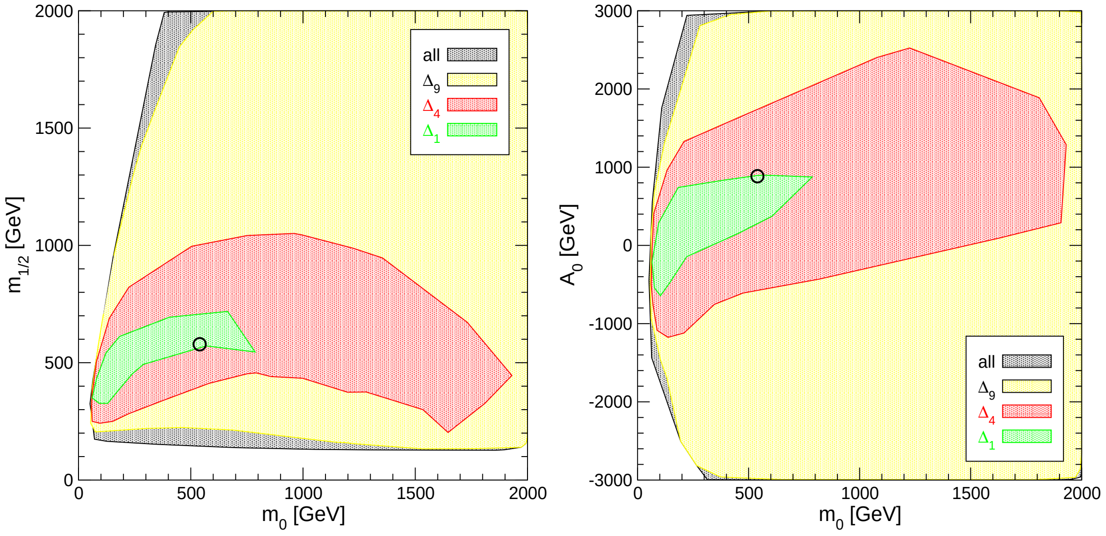

Figure 3.7: The $\Delta_{1,4,9}$ regions in the m_0–$m_{1/2}$ plane (left) and in the m_0–A_0 plane (right) in the CMSSM for $\mu > 0$. The Δ_1 area is medium shaded (green), the Δ_4 area is dark shaded (red), and the Δ_9 area is light shaded (yellow). The rest of the scanned parameter space is given in black shading. The best-fit point is marked with a circle.

sign convention here in comparison with Refs. [104, 105, 106, 107, 108]), and the Δ_4 region extends from -1000 GeV to about $+2500$ GeV. The apparent differences to existing analyses [104, 105, 111] are due to the fact that the CDM constraint has not been applied here, see the discussion below.

mGMSB

In Figs. 3.8, 3.9 we show the results for the $\Delta_{1,4,9}$ areas in terms of the high-energy parameters, using the current experimental and theoretical precisions as described in Sect. 3.3. The color coding is as in Fig. 3.7. As in the CMSSM, because of the contribution to $(g-2)_\mu$ only very few points with $\mu < 0$ have $\Delta\chi^2 < 9$, and we concentrate here on the data with $\mu > 0$.

The plots in Fig. 3.8 show the Λ–$M_{\rm mess}$ plane for $N_{\rm mess} = 1 \ldots 8$ separately. The $\Delta\chi^2$ values are obtained with respect to the overall best fit point, which is reached for $N_{\rm mess} = 8$ (marked with a circle). The 'preferred' Λ values depend on the choice of $N_{\rm mess}$, going from $\sim 10^5$ GeV at low $N_{\rm mess}$ down to $\sim 2 \times 10^4$ GeV for

N_{mess}	1	2	3	4	5	6	7	8
$\chi^2_{\mathrm{min},N_{\mathrm{mess}}}$	6.17	5.53	5.45	5.25	5.25	5.20	5.16	5.13

Table 3.2: Minimum χ^2 values reached for each N_{mess} in mGMSB.

large N_{mess}. However, the Δ_9 region extend over large parts of the whole parameter space. Furthermore no bound on M_{mess} can be set. Similar results are found in Fig. 3.9, where we show the N_{mess}–Λ plane. The lower N_{mess}, the higher are the possible values for Λ.

In order to analyze the compatibility of the various N_{mess} values with the precision data, we show in Tab. 3.2 the lowest $\chi^2_{\mathrm{min},N_{\mathrm{mess}}}$ values reached for each N_{mess}. It can be seen that $\chi^2_{\mathrm{min},N_{\mathrm{mess}}}$ increases monotonically with decreasing N_{mess}. In agreement with Figs. 3.8 and 3.9 the difference in the minimum χ^2 between $N_{\mathrm{mess}} = 8$ and $N_{\mathrm{mess}} > 1$ is smaller than one, and only for $N_{\mathrm{mess}} = 1$ the difference exceeds one by ~ 0.04. Consequently no Δ_1 region appears in the $N_{\mathrm{mess}} = 1$ plots.

mAMSB

In Fig. 3.10 we show the only high-energy parameter plane in the mAMSB, m_{aux} vs. m_0 for $\mu > 0$. While nearly the whole parameter space is covered by the Δ_9 area, the Δ_4 and Δ_1 regions are located at a relatively thin strip at the lowest possible m_0 values with a width $\lesssim 300$ GeV. The precision observables clearly show a preference for a relatively small scalar soft SUSY-breaking parameter m_0. This can be traced back to the χ^2 contribution to $(g-2)_\mu$ that requires relatively light sleptons of the second generation. Since m_0 is needed to prevent the tachyon problem within mAMSB, it controls to a large extent the slepton masses. The strong bound from $(g-2)_\mu$ then translates into a relatively strong bound on m_0. On the other hand, m_{aux} is only mildly restricted. The lower absolute bound on m_{aux} is mainly due to the lower experimental bound on the lightest chargino of ~ 70 GeV [124].

3.4.2 Low-energy Analysis

We now turn to the comparison of the three soft SUSY-breaking scenarios. In Fig. 3.11 we show the M_A–$\tan\beta$ plane for the CMSSM (top), mGMSB (middle) and mAMSB (bottom) with the same color coding as in Fig. 3.7. As in Sect. 3.4.1 we restrict ourselves to $\mu > 0$. The allowed M_A–$\tan\beta$ parameter space is somewhat different in the three scenarios. While in mAMSB the parameters are restricted to $M_A \lesssim 4$ TeV and $\tan\beta \lesssim 50$, this extends to $M_A \lesssim 4$ TeV and $\tan\beta \lesssim 60$ (where we stopped our $\tan\beta$ scan) in the CMSSM, and within mGMSB M_A values up to 6 TeV are possible (not shown in the plot). The qualitative features of the $\Delta_{9,4,1}$ areas are very similar for the three scenarios. The Δ_9 area extends over large parts of the whole parameter space. On the other hand, within all three scenarios, the Δ_4 and even more the Δ_1 areas are located at relatively low M_A, extending up to $M_A \lesssim 1000$ GeV at the Δ_4 level in all three scenarios. The 'preferred' $\tan\beta$ regions, on the other hand, nearly span the full possible range in the CMSSM and mGMSB, whereas in the mAMSB scenario the χ^2 'preferred' areas are located at lower $\tan\beta$ values, reaching up to $\tan\beta \lesssim 35$. The low value of $\mathrm{BR}(B_s \to \mu^+\mu^-)$ at the best-fit point in mAMSB is due to the relatively low $\tan\beta$ value. However, in view of these ranges, the actual values of the best-fit points for $\tan\beta$ are not very significant, in accordance with earlier analyses [104, 105, 106, 107, 109]. In conclusion a preference for not too large M_A values is clearly visible as a common feature in all three scenarios. Depending on the actual combination of M_A and $\tan\beta$, the LHC can cover a large part of the 'preferred' parameter space by searches for the heavy Higgs bosons [237, 238, 239, 240, 241, 242].

We now turn to the analysis of various mass values in the three soft SUSY-breaking scenarios. We start with the mass of the lightest CP-even Higgs boson, see Sect. 3.3.4, presented in Fig. 3.12. M_h is shown in the CMSSM (top), mGMSB (middle) and mAMSB (bottom) scenarios for $\mu > 0$ with the corresponding χ^2, where the χ^2 contribution of M_h itself has been left out. In this way the plot shows the indirect predictions for M_h without imposing the bounds from the Higgs boson searches at LEP. In the CMSSM and in mGMSB the impact of dropping the χ^2 contribution from M_h leads to a drastically lower total χ^2 as compared to the case when the M_h bound is included, see Tab. 3.1. In these two scenarios the best-fit point changes to new points with substantially lower M_h values (as discussed below). These new best-fit points can also accomodate the other precision observables better, thus leading to a reduction of $\chi^2_{\rm min}$ by more than ~ 3 in the CMSSM and mGMSB. In the mAMSB scenario, on the other hand, the effect is small, and the best-fit point changes only slightly. The color coding is as in Fig. 3.7.

In all three scenarios a shallow minimum can be observed. The Δ_1 regions are in the intervals of $M_h = 98 \ldots 111$ GeV (CMSSM), $97 \ldots 112$ GeV (mGMSB) and $104 \ldots 122$ GeV (mAMSB). In all three scenarios the Δ_4 regions extend beyond the LEP limit of $M_h > 114.4$ GeV at the 95% C.L. shown as dashed (blue) line in Fig. 3.12 (which is valid for the three soft SUSY-breaking scenarios, see Refs. [214, 215]). The analysis for the CMSSM can be compared with Refs. [106, 111], where (among other contributions) also the cold dark matter constraint had been included in the analysis. In Refs. [106, 111] best fit values of $M_h = 110 \ldots 115$ GeV (depending on $\tan\beta$) had been observed, which is at the border of the Δ_1 region here. These results are well compatible with each other. The inclusion of the CDM constraint yields the effect of cutting out a (thin) band in the M_h–$\chi^2_{\rm tot}$ plane. In conclusion all three scenarios have a significant part of the parameter space with a relatively low total χ^2 that is in agreement with the bounds from Higgs-boson searches at LEP. Especially within the mAMSB scenario the Δ_1 region extends beyond the LEP bound of 114.4 GeV.

Next we turn to the prediction of the masses of various SUSY particles, starting with $m_{\tilde\chi^0_1}$ (left) and $m_{\tilde\chi^0_2}$ (right) in Fig. 3.13. The masses are shown in the CMSSM (top), mGMSB (middle) and mAMSB (bottom) scenarios for $\mu > 0$ with their respective total χ^2, i.e. including the χ^2 contribution of M_h. The color coding is as in Fig. 3.7. The mGMSB shows for all masses (see below) a local minimum at a lower value and an absolute minimum at a somewhat higher mass value. The effect of having a minimum in the χ^2 plot can in general be understood by investigating the χ^2 contribution of M_h and of $(g-2)_\mu$. While the former penalizes strongly a light spectrum (especially for the stops), the latter penalizes a heavy spectrum (especially sleptons and charginos/neutralinos). The appearance of the second local minimum at lower mass values is a result from the interplay of several observables, especially M_W and M_h. Going to a lighter spectrum improves $\chi^2(M_W)$ more than it worsens $\chi^2(M_h)$, while a very light spectrum results in a very large χ^2 contribution from M_h, yielding the local minimum in between.

In the three scenarios limited ranges can be observed for the Δ_1 and Δ_4 regions, whereas the Δ_9 regions extend to the highest possible mass values. For the CMSSM and mAMSB the truncation of the parameter space at high $m_{1/2}$, $m_{\rm aux}$ and m_0 is clearly visible for some particle masses, e.g. in the left column of Fig. 3.13. The mass of the lightest neutralino (the LSP) has 'preferred' values, $\Delta\chi^2 < 4$, ranging from about 100 GeV to values up to 500 GeV, depending on the scenario. Within the CMSSM and mAMSB the lightest neutralino, being stable, cannot be observed via a decay to other particles, so that its detection has to rely on a 'missing energy' signature. In mGMSB the LSP is the gravitino, $\tilde{G}$, leading to distinctive decay patterns of the $\tilde{\chi}_1^0$ if it decays within the detector. The decay BRs depend largely on the mass pattern of the $\tilde{\chi}_1^0$, $\tilde{\tau}_1$ and $\tilde{G}$. The 'preferred' mass values thus offer good prospects for the detection at the LHC and excellent prospects for the ILC(1000) (i.e. with $\sqrt{s}$ up to 1 TeV) in the case where the decay happens in the detector. At the ILC also the process $e^+e^- \to \tilde{\chi}_1^0\tilde{\chi}_1^0\gamma$ can in principle be observed, permitting in this case the observation of the $\tilde{\chi}_1^0$ in all the three scenarios in the 'preferred' mass ranges.

The second lightest neutralino, see the right column of Fig. 3.13, can in principle be observed via its decay to a SM particle and the LSP (or another SUSY particle if it is lighter than the $\tilde{\chi}_2^0$, as e.g. the $\tilde{\chi}_1^\pm$ in the case of the mAMSB). The best fit values vary around 300 GeV to values above 550 GeV, depending on the scenario. With these mass ranges the observation at the LHC will be very challenging for the direct production, but might be better (depending on SUSY mass patterns) for the production in cascades. At the ILC(1000) one could search for the associated production of $e^+e^- \to \tilde{\chi}_1^0\tilde{\chi}_2^0$. The three soft SUSY-breaking scenarios show similar prospects for the discovery, although mGMSB results in overall somewhat higher mass scales.

The predictions of the lightest chargino mass, $m_{\tilde{\chi}_1^\pm}$ (left), and the gluino mass, $m_{\tilde{g}}$ (right), are shown in Fig. 3.14. As before, the masses are shown in the CMSSM (top), mGMSB (middle) and mAMSB (bottom) scenarios for $\mu > 0$ with their respective total χ^2. The color coding is as in Fig. 3.7. In the three scenarios limited ranges can be observed for the Δ_1 and Δ_4 regions, whereas the Δ_9 regions extend to the highest possible mass values. Within the CMSSM and mGMSB the light chargino mass ranges from about 100 GeV up to ~ 900 GeV in the Δ_4 area, whereas somewhat higher masses are reached in mGMSB. Consequently only a part of the 'preferred' parameter space can be accessed at the LHC or the ILC(1000). Within the CMSSM and mGMSB the $\tilde{\chi}_1^\pm$ and the $\tilde{\chi}_2^0$ are nearly mass degenerate, resulting in very similar results for the two particles as can be seen in Figs. 3.13 and 3.14. The situation concerning the observation of the $\tilde{\chi}_1^\pm$ is much more favorable in mAMSB, where much lighter masses, only up to about 300 GeV are preferred. This offers very good perspectives for its production at the LHC and the ILC. However, it should be kept in mind that in the mAMSB scenario the lightest chargino is only a few hundred MeV heavier than the LSP, which poses certain problems for its detection [243].

The 'preferred' gluino masses, as shown in the right column of Fig. 3.14, range from a few hundred GeV up to about 3 TeV in mGMSB, exhausting the accessible range at the LHC. In the other two scenarios the Δ_4 regions end at ~ 2 TeV (mAMSB) and ~ 2.5 TeV (CMSSM), making them more easily accessible at the LHC than in the mGMSB scenario.

We now turn to the scalar fermion sector. The predictions for the two scalar tau masses, $m_{\tilde{\tau}_1}$ (left) and $m_{\tilde{\tau}_2}$ (right), are shown in Fig. 3.15. As before, the masses are shown in the CMSSM (top), mGMSB (middle) and mAMSB (bottom) scenarios for $\mu > 0$ with their respective total χ^2. The color coding is as in Fig. 3.7. The light $\tilde{\tau}$ has its best-fit values at very low masses, and even the Δ_4 regions hardly exceed ~ 500 GeV in mGMSB and mAMSB. Therefore in these scenarios there are good prospects for the ILC(1000). Also the LHC can be expected to cover large parts of the Δ_4 mass intervals. In the CMSSM scenario, on the other hand, the Δ_4 region exceeds ~ 1 TeV such that only parts can be probed at the ILC(1000) and the LHC. The 'preferred' $m_{\tilde{\tau}_2}$ values, by construction larger than $m_{\tilde{\tau}_1}$, stay mostly below 500, 1000, 1500 GeV for mAMSB, mGMSB and the CMSSM, respectively.

In Fig. 3.16 we show the predictions for the two scalar top masses, $m_{\tilde{t}_1}$ (left) and $m_{\tilde{t}_2}$ (right). As before, the masses are shown in the CMSSM (top), mGMSB (middle) and mAMSB (bottom) scenarios for $\mu > 0$ with their respective total χ^2. The color coding is as in Fig. 3.7. The 'preferred' mass ranges, i.e. $\Delta\chi^2 < 4$, range from about 300 GeV up to about 2300 GeV, depending somewhat on the scenario. Finally, the predictions for the sbottom masses are shown in Fig. 3.17. The sbottom masses follow the same pattern as the stop masses. Taking these values as representative scalar quark mass values, the LHC should have no problem to discover the SUSY partners of the quarks, whereas for the ILC(1000) only the lower part of the 'preferred' values could be in the kinematic reach. However, it should be kept in mind that the Δ_9 regions extend beyond ~ 3 TeV, which could exceed even the discovery reach of the SLHC [244].

Apart from the values of the various SUSY and Higgs particle masses, also the 'preferred' values of $|\mu|$ and of B (with $\mu\, B$ being the prefactor of the Higgs mixing term in the potential) are of interest. In Tab. 3.3 we list the current best fit points and the $\Delta_{1,4}$ ranges for μ (with $\mu > 0$, see Sect. 3.3.3) and B. The 'preferred' values for μ range between 130 GeV and 1420 GeV in the mAMSB and somewhat smaller intervals within in the two other scenarios. The 'preferred' values of B are bounded from above by ~ 540 GeV in mAMSB, where also negative values down to -275 GeV are reached in the Δ_4 area. In the other two scenarios the intervals are substantially smaller, and only in the CMSSM negative values down to -75 GeV are reached.

The results for the SUSY masses in the CMSSM can be compared with previous analyses taking into account the CDM constraint [104, 105, 106, 109, 111]. We focus here on Refs. [104, 105, 106], since similar sets of precision observables and

	CMSSM	mGMSB	mAMSB
μ (best fit)	588	810	604
μ in Δ_1	510 – 730	460 – 995	560 – 980
μ in Δ_4	160 – 1100	390 – 1400	130 – 1420
B (best fit)	94	151	28
B in Δ_1	65 – 155	75 – 210	-105 – 50
B in Δ_4	-75 – 250	65 – 330	-275 – 540

Table 3.3: 'Preferred' values of μ and B (with $\mu\, B$ being the prefactor of the Higgs mixing term in the potential). Shown are the best-fit points as well as the intervals covered for $\Delta\chi^2 < 1, 4$. All values are in GeV.

very similar χ^2 analyses had been used. Qualitative agreement can be found in the observed 'preferred' mass values. In our analysis the lower mass values in the Δ_1 and Δ_4 regions are obtained for low $\tan\beta$, where these masses are similar to to the ones in Refs. [104, 105, 106] obtained for $\tan\beta = 10$. Higher mass values in the Δ_1 and Δ_4 regions, on the other hand, are obtained for large $\tan\beta$, where these masses are similar to the ones in Refs. [104, 105, 106] obtained for $\tan\beta = 50$. On the other hand, the following difference can be observed: while the fit results obtained for the particle masses in Refs. [104, 105, 106] are 'parabola shaped', whereas the mass plots presented in Figs. 3.13 – 3.17 show 'full' areas. This can easily be understood as an effect of taking the CDM constraint into account in Refs. [104, 105, 106], while at the same time $\tan\beta$ had been restricted to the two discrete values $\tan\beta = 10$ and 50. The CDM constraint cuts out thin strips, for instance, in the m_0–$m_{1/2}$ plane (for fixed A_0 and $\tan\beta$) [245, 246]. This yields naturally strips in the mass vs. $\chi^2_{\rm tot}$ plots. Incorporating all $\tan\beta$ values by scanning over all allowed values simultaneously in our analysis (where low (high) $\tan\beta$ values yield lower (higher) best-fit masses), broadens and fills automatically the Δ_1 and Δ_4 regions. Another difference in our analysis compared to the ones in Refs. [104, 105, 106] is the lower value of m_t that has been used here. Lowering the experimental value of m_t in the χ^2 analysis yields an increase in the minimum total χ^2, as has been analyzed for $\tan\beta = 10$

in Ref. [105]. The minimum χ^2 values reached in Refs. [104, 105, 106] and in our analysis roughly follow the results presented in Ref. [105]. However, it should be kept in mind that the latest value of m_t that has been published recently [136] has moved upwards to $m_t^{\mathrm{exp}} = 172.6 \pm 1.4$ GeV.

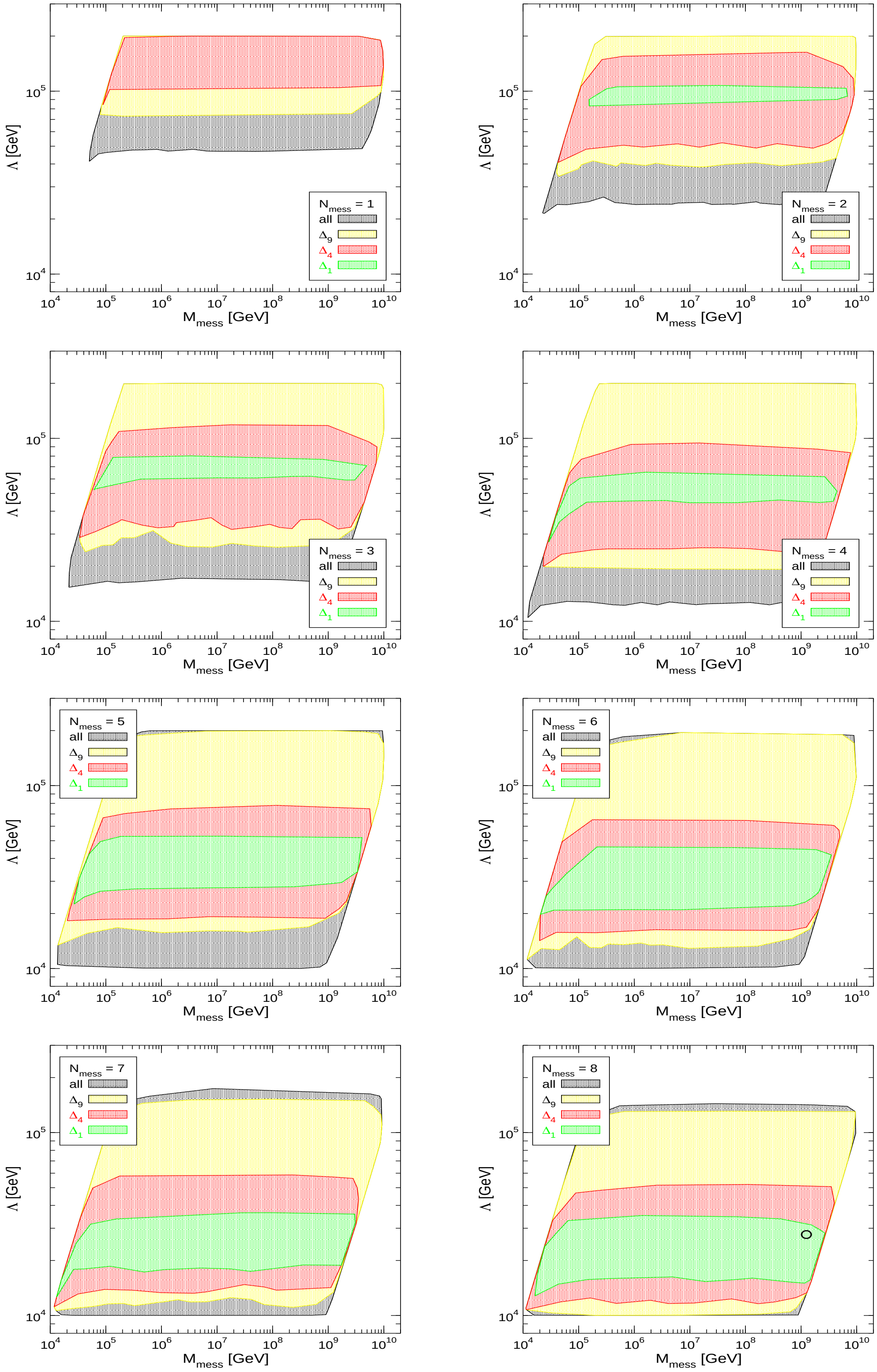

Figure 3.8: The $\Delta_{1,4,9}$ regions in the $M_{\rm mess}$–Λ plane for $N = 1 \ldots 8$ in the mGMSB for $\mu > 0$. The color coding is as in Fig. 3.7. The best fit point is realized for $N_{\rm mess} = 8$ and marked with a circle.

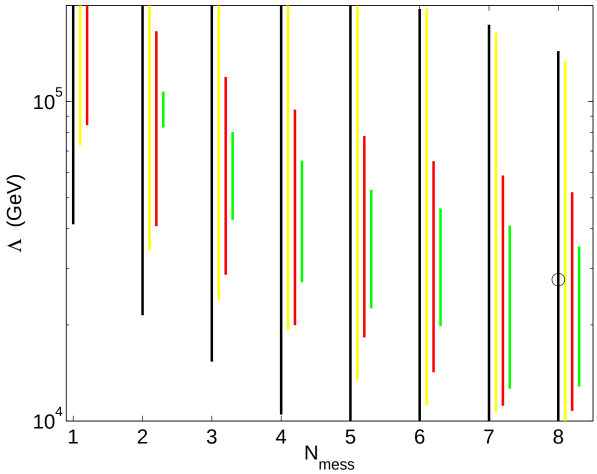

Figure 3.9: The $\Delta_{1,4,9}$ regions in the N_{mess}–Λ plane in the mGMSB for $\mu > 0$. The color coding is as in Fig. 3.7. Marked with a circle is the current best-fit point.

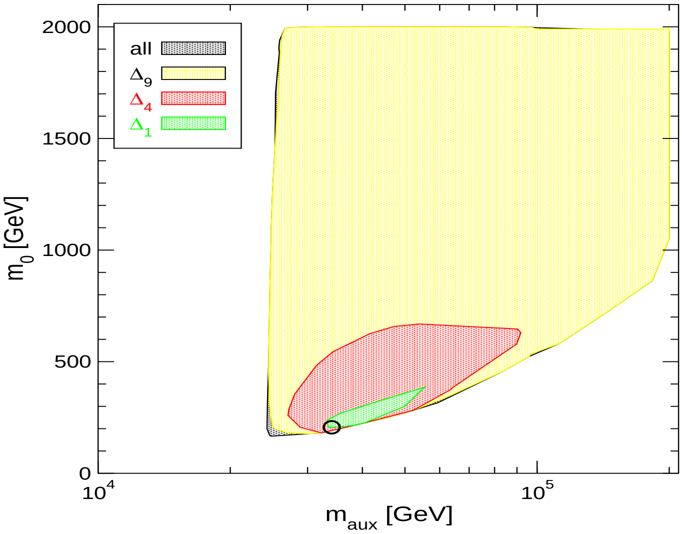

Figure 3.10: The $\Delta_{1,4,9}$ regions in the m_{aux}–m_0 plane in the mAMSB for $\mu > 0$. The color coding is as in Fig. 3.7. The best-fit point is marked with a circle.

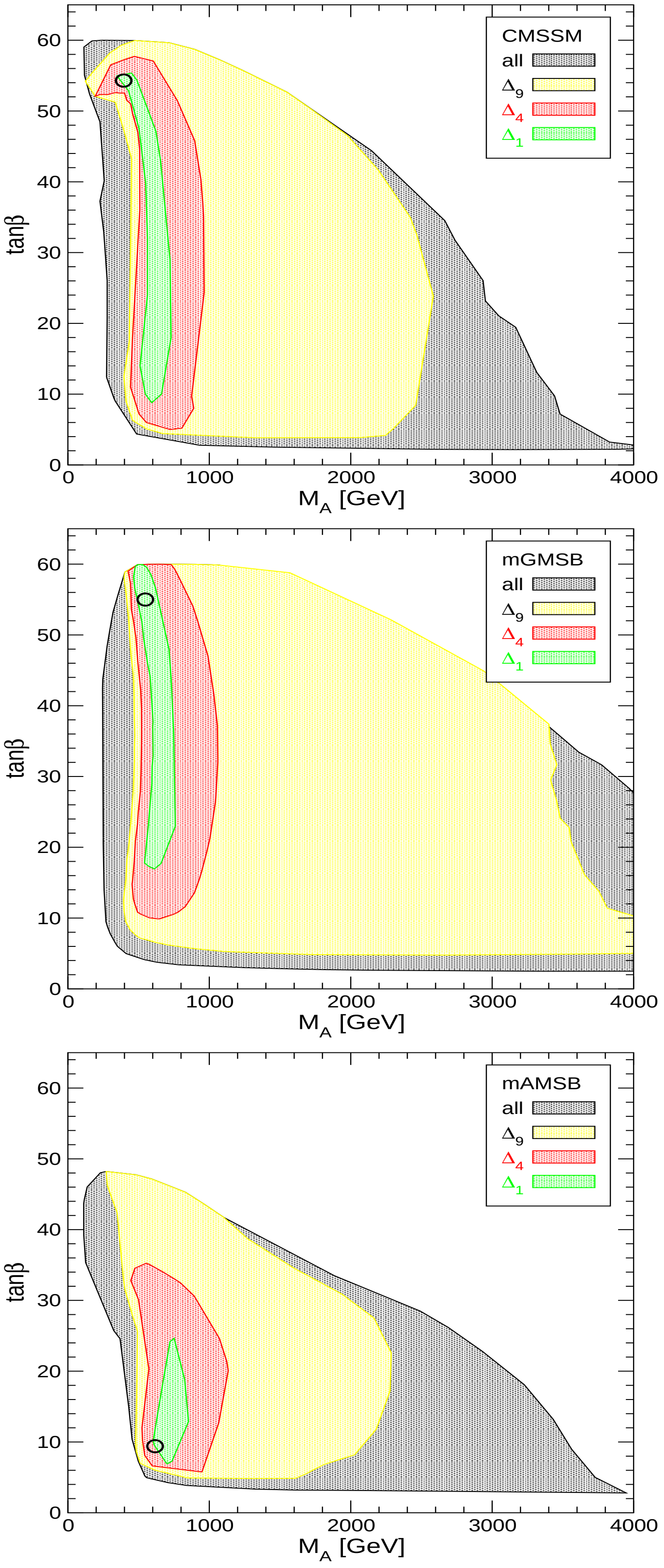

Figure 3.11: The $\Delta_{1,4,9}$ regions in the M_A–$\tan\beta$ planes in the CMSSM (top), mGMSB (middle) and mAMSB (bottom) for $\mu > 0$. The color coding is as in Fig. 3.7. In each plot the best-fit point is marked with a circle.

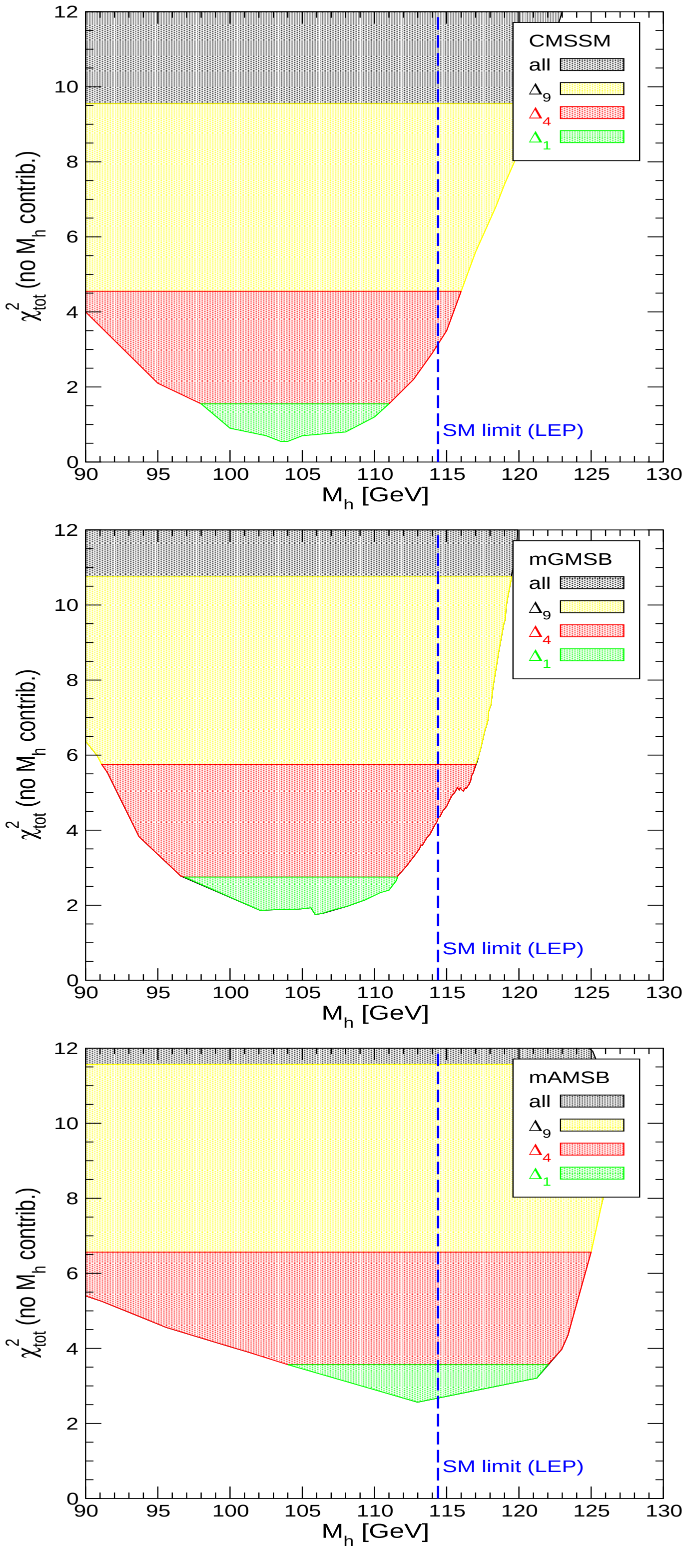

Figure 3.12: The M_h values in the CMSSM (top), mGMSB (middle) and mAMSB (bottom) scenarios for $\mu > 0$ with their respective χ^2, where the χ^2 contribution of the M_h itself has been left out. The color coding is as in Fig. 3.7. The SM limit of 114.4 GeV obtained at LEP is indicated with a dashed (blue) line.

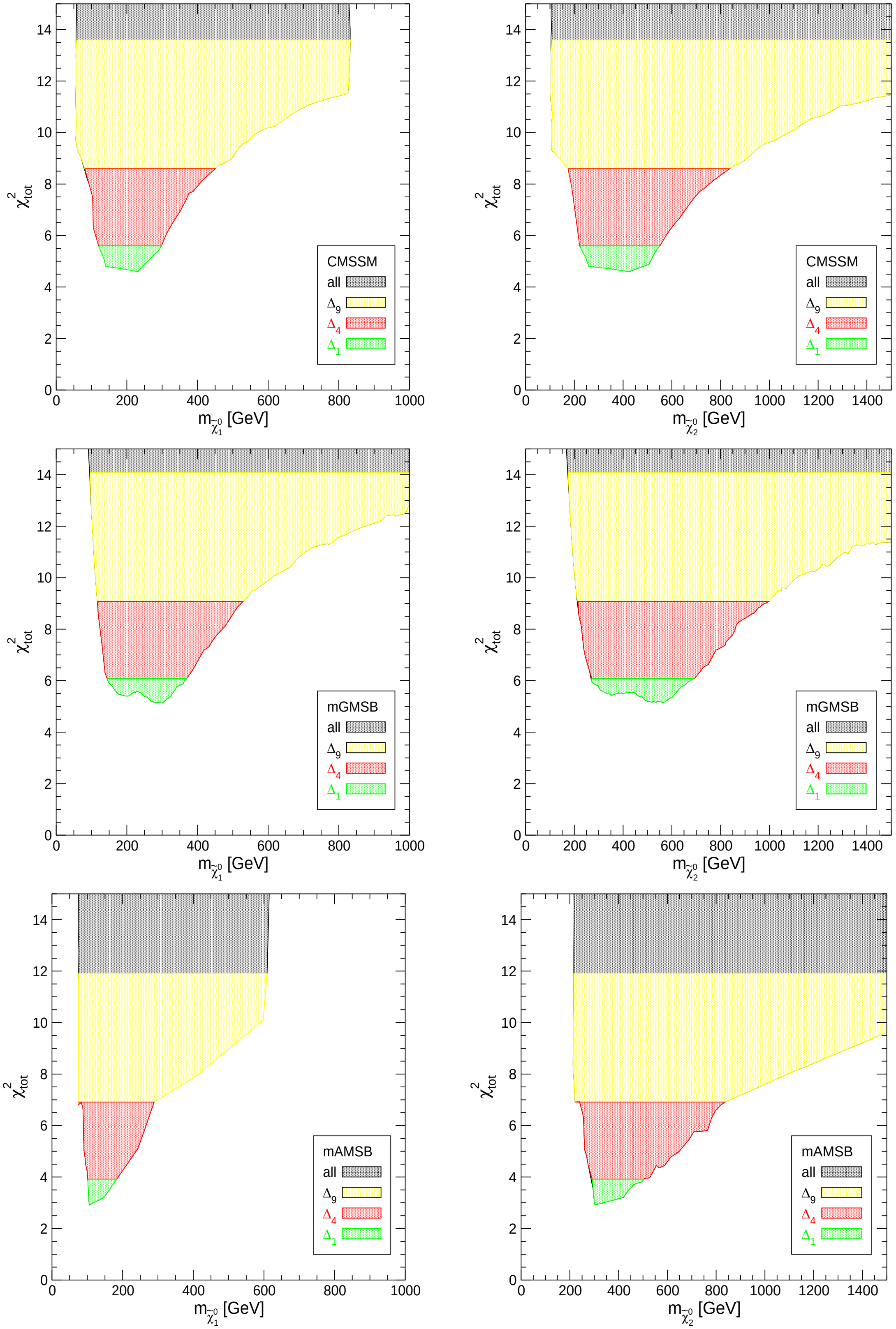

Figure 3.13: $m_{\tilde{\chi}^0_1}$ (left) and $m_{\tilde{\chi}^0_2}$ (right) are shown in the CMSSM (top), mGMSB (middle) and mAMSB (bottom) scenarios for $\mu > 0$ with their respective total χ^2, i.e. including the χ^2 contribution of M_h. The color coding is as in Fig. 3.7.

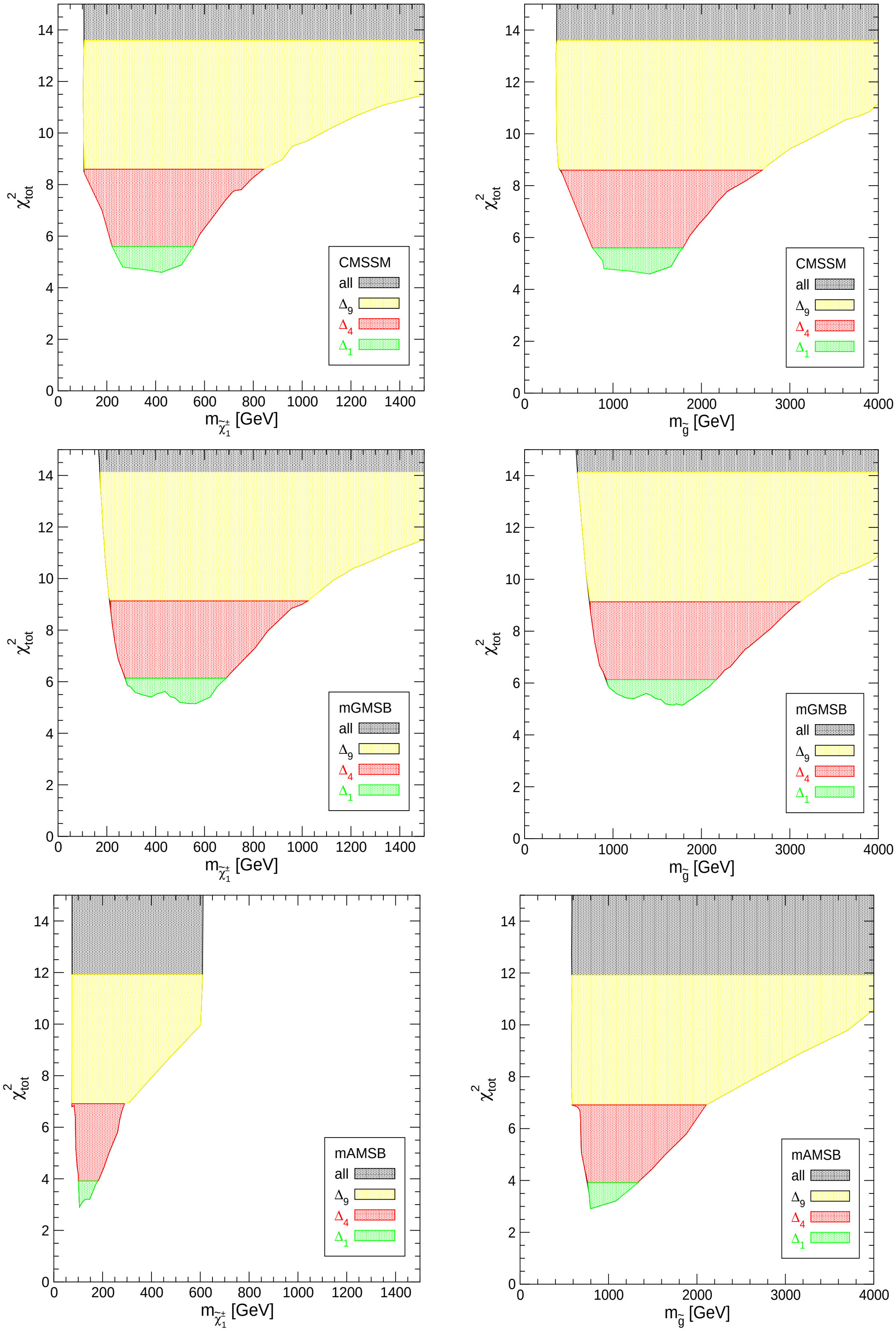

Figure 3.14: $m_{\tilde{\chi}_1^\pm}$ (left) and $m_{\tilde{g}}$ (right) are shown in the CMSSM (top), mGMSB (middle) and mAMSB (bottom) scenarios for $\mu > 0$ with their respective total χ^2. The color coding is as in Fig. 3.7.

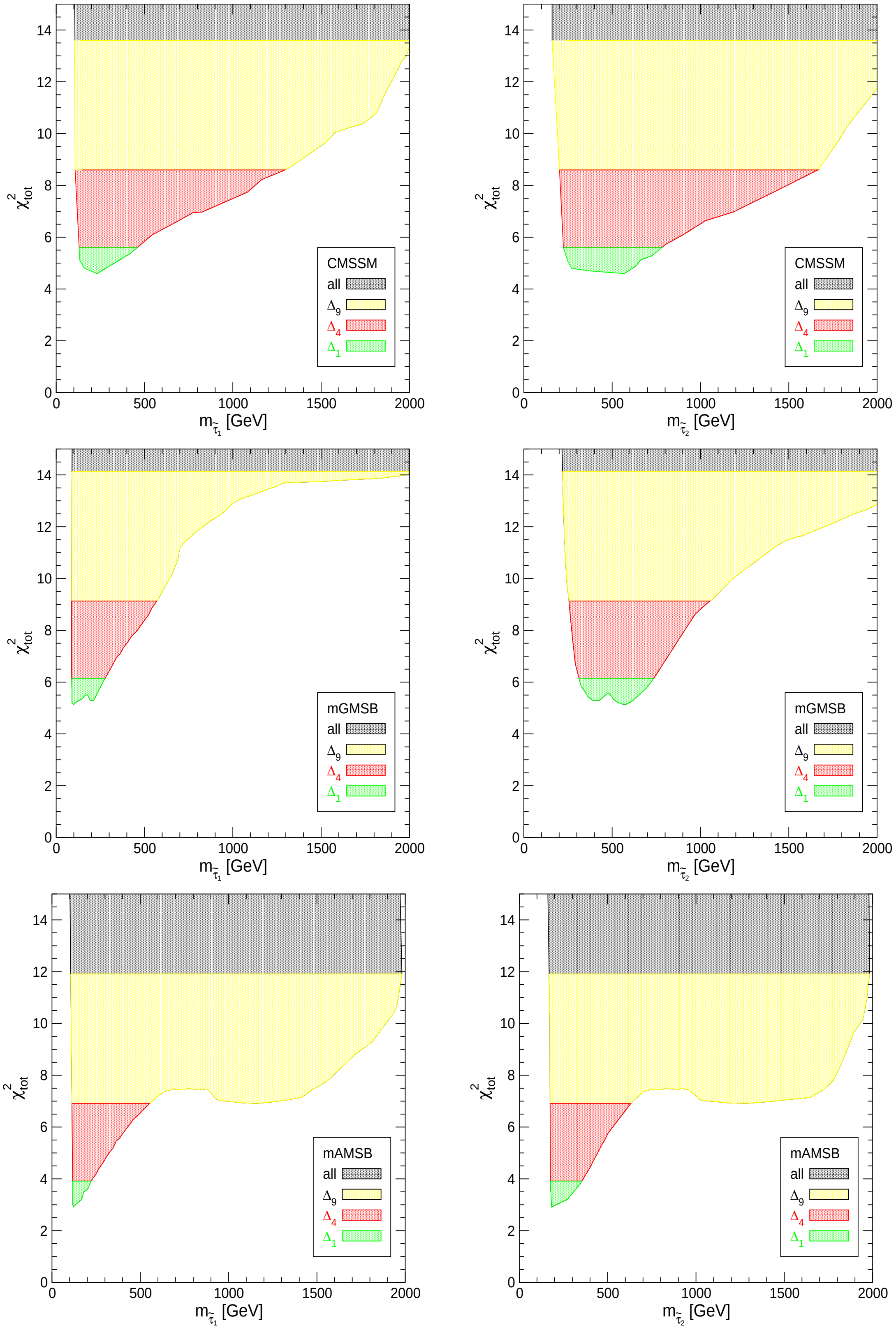

Figure 3.15: $m_{\tilde{\tau}_1}$ (left) and $m_{\tilde{\tau}_2}$ (right) are shown in the CMSSM (top), mGMSB (middle) and mAMSB (bottom) scenarios for $\mu > 0$ with their respective total χ^2. The color coding is as in Fig. 3.7.

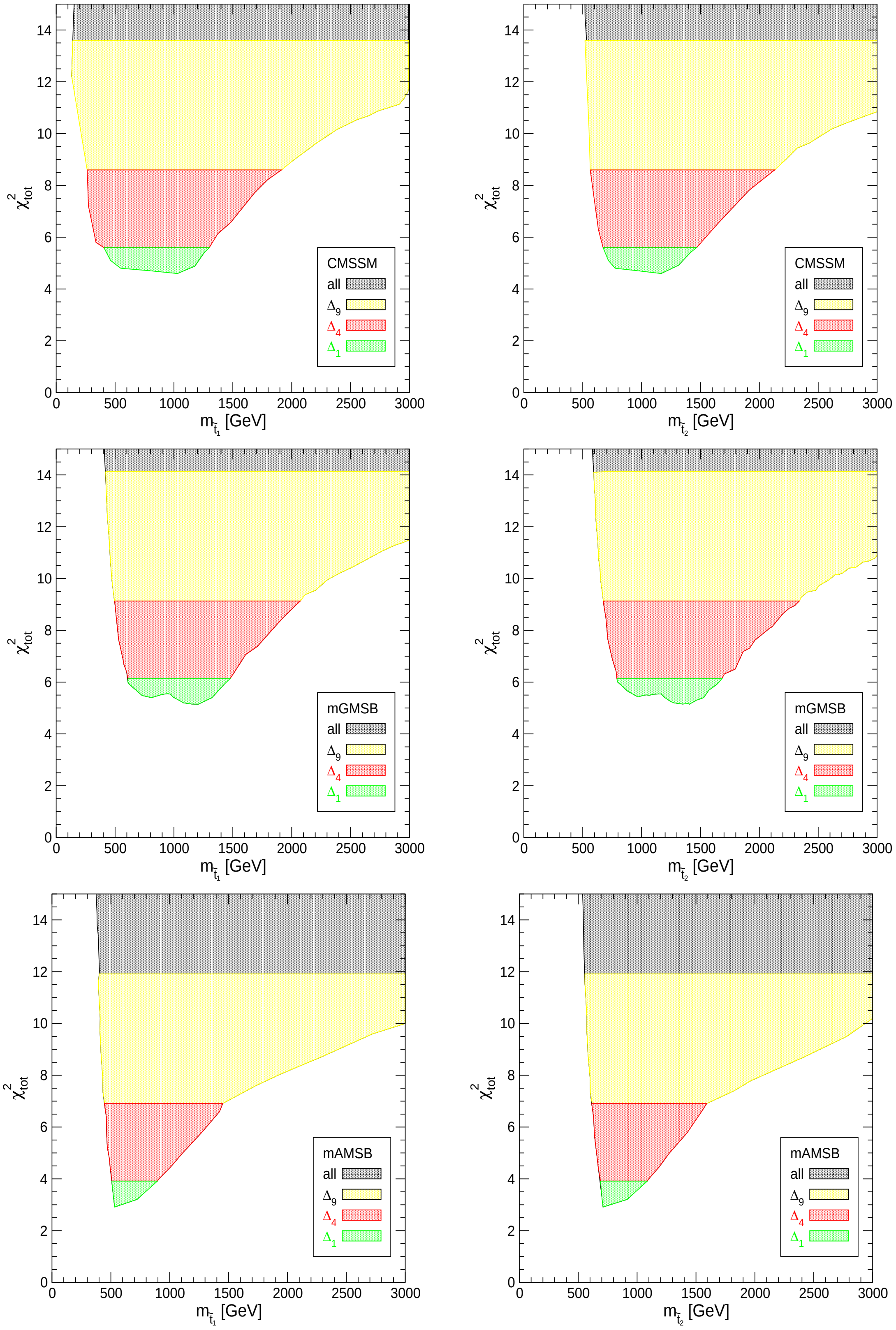

Figure 3.16: $m_{\tilde{t}_1}$ (left) and $m_{\tilde{t}_2}$ (right) are shown in the CMSSM (top), mGMSB (middle) and mAMSB (bottom) scenarios for $\mu > 0$ with their respective total χ^2. The color coding is as in Fig. 3.7.

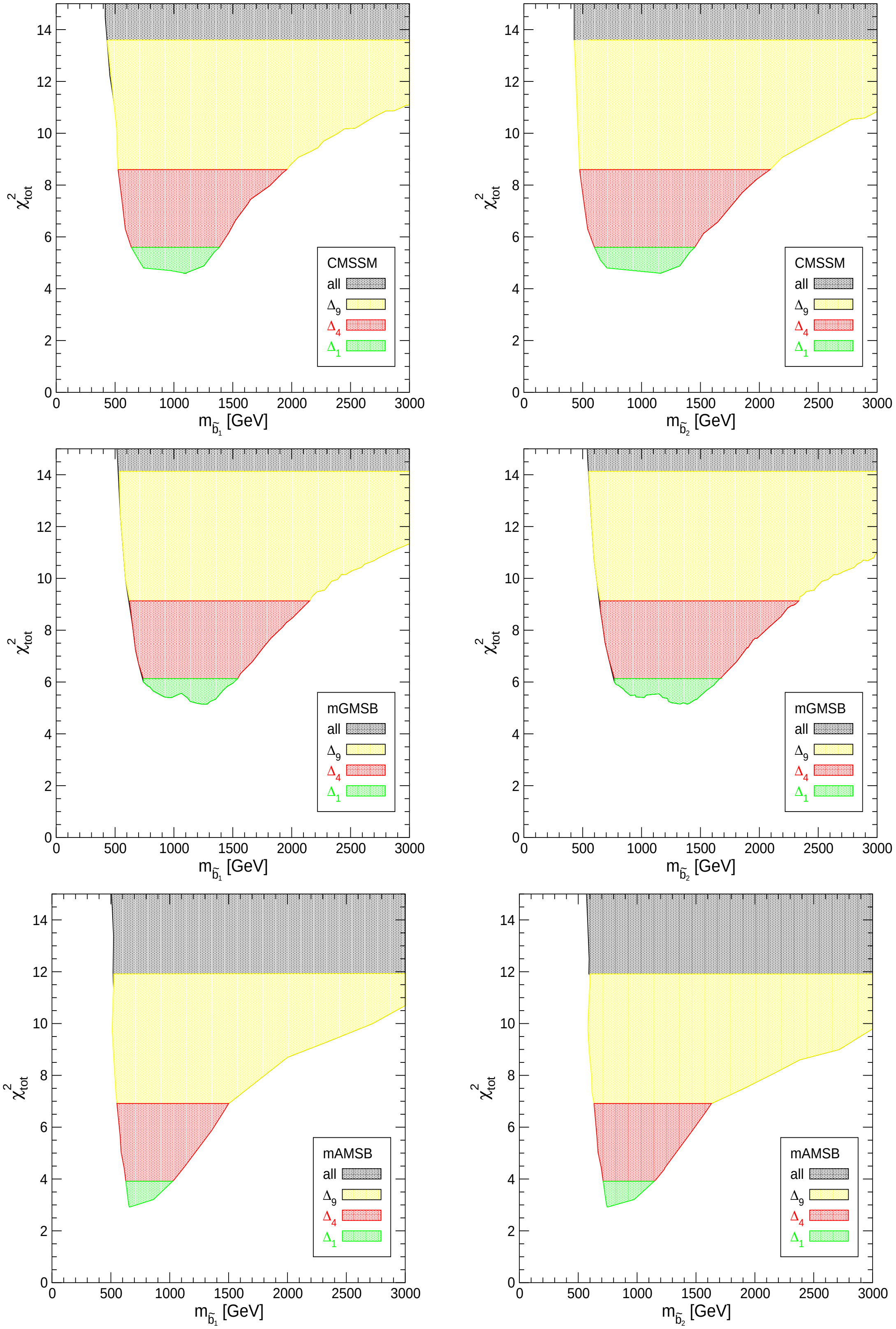

Figure 3.17: $m_{\tilde{b}_1}$ (left) and $m_{\tilde{b}_2}$ (right) are shown in the CMSSM (top), mGMSB (middle) and mAMSB (bottom) scenarios for $\mu > 0$ with their respective total χ^2. The color coding is as in Fig. 3.7.

3.5 Future Sensitivities

We now turn to the analysis of the future sensitivities. In a first step we take the current best-fit point in each scenario and assume that the future measurements exactly agree with this point. The experimental and theory uncertainties are set to their 'future' values as discussed in Sect. 3.3. Also for M_h we assume that its value is measured and include it into the χ^2 fit with the future uncertainties given in Sect. 3.3.4. In a second step, in order to compare the sensitivities in the three scenarios, we have chosen one hypothetical best-fit point in each scenario, where the low-energy spectrum is "similar" in all three scenarios. In more detail, we have demanded that

$$M_A \approx 800 \text{ GeV}, \quad \tan\beta \approx 40, \quad m_{\tilde{t}_1} \approx 1225 \text{ GeV}, \quad m_{\tilde{t}_2} \approx 1400 \text{ GeV}, \quad \mu > 0 \ . \tag{3.34}$$

These masses are somewhat higher than the current best-fit values and thus illustrate a future scenario that is somewhat more in the decoupling regime (i.e. where SUSY masses are heavy and loop corrections are correspondingly smaller) than what is currently favored. Furthermore the combination of M_A and $\tan\beta$, according to current analyses [216, 217, 218, 219, 237, 238, 239, 240, 241, 242, 244], is not in the discovery reach of the LHC or the ILC. In such a scenario without experimental information on M_A and $\tan\beta$ from the observation of the heavy Higgs bosons any sensitivity to these parameters would constitute information *in addition* to the direct collider data. The three points are defined in terms of high-energy parameters as

$$\begin{aligned}\text{CMSSM}\ :\ & m_0 = 640\ \text{GeV} \\ & m_{1/2} = 720\ \text{GeV} \\ & A_0 = 500\ \text{GeV} \\ & \tan\beta = 41\end{aligned} \tag{3.35}$$

$$\begin{aligned}\text{mGMSB}\ :\ & \Lambda = 33200\ \text{GeV} \\ & M_{\text{mess}} = 580000\ \text{GeV} \\ & N_{\text{mess}} = 7 \\ & \tan\beta = 41\end{aligned} \tag{3.36}$$

$$\begin{aligned}\text{mAMSB}\ :\ & m_{\text{aux}} = 50500\ \text{GeV} \\ & m_0 = 1600\ \text{GeV} \\ & \tan\beta = 40\end{aligned} \tag{3.37}$$

The choices in eq. (3.34) ensure a “similar” behavior in the Higgs and in the scalar top sector and their contributions to the EWPO and BPO. This allows a comparison of the future sensitivities of the EWPO and BPO in the three scenarios. The values for the lightest Higgs boson mass at the three hypothecial best-fit points are 116.8 GeV (CMSSM), 117.5 GeV (mGMSB) and 119.1 GeV (mAMSB). The spread of ~ 2.3 GeV has only a minor direct impact on the predictions of the EWPO and BPO.

3.5.1 Analysis of High-scale Parameters

We start by analyzing the CMSSM, mGMSB and mAMSB in terms of their respective high-energy parameters, see Sect. 3.2.

CMSSM

In Fig. 3.18 we show the results for the $\Delta_{1,4,9}$ areas in terms of the high-energy parameters, using the χ^2 result based on the assumed future experimental and theoretical precisions as described in Sect. 3.3. As can been seen, the areas of the parameter space with $\Delta\chi^2 < 1, 4, 9$ shrink substantially in comparison with Fig. 3.7. At the $\Delta\chi^2 = 9$ level $m_{1/2}$ is determined up to ±200 GeV for the assumed best-fit point. For m_0, on the other hand, still values up to ~ 1500 GeV are permitted. The Δ_9 interval for A_0 shrinks to ±1000 GeV.

The reduction of the preferred parameter region with the assumed higher precision in the future is so substantial because the currently favored best-fit parameters are relatively small, where smaller SUSY mass scales lead to larger loop effects in the precision observables. This effect is less pronounced for larger GUT scale parameters. To illustrate this effect we have chosen a CMSSM point as defined in eq. (3.35). We assume that the future experimental values agree exactly with the low-energy parameters resulting from eq. (3.35). The reduction of the preferred parameter region as shown in Fig. 3.19 compared to the present situation is still visible, but much weaker than for the current best-fit point in Fig. 3.18. Similar results (including the CDM constraint) had been found in Ref. [104].

mGMSB

In Fig. 3.20 we show the results for the $\Delta_{1,4,9}$ areas in terms of the high-energy parameters, using the future experimental and theoretical precisions as described in Sect. 3.3. The color coding is as in Fig. 3.7. The plots in Fig. 3.20 show the Λ–$M_{\rm mess}$ plane for $N_{\rm mess} = 1 \ldots 8$. For each $N_{\rm mess}$ a small Λ interval is singled out, but hardly any limit on $M_{\rm mess}$ is obtained even with the future precisions.

The results look similar in Fig. 3.22, where we show the $N_{\rm mess}$–Λ plane. For each $N_{\rm mess}$ value a relatively small range of Λ is favored, even at the $\Delta\chi^2 = 9$ level. If $N_{\rm mess}$ could be determined in an independent way, the precision observables could give a relatively precise determination of Λ. On the other hand, if Λ could be determined, e.g. from the measurement of SUSY masses, the precision observables would give a preference for certain $N_{\rm mess}$ values.

As for the CMSSM scenario also in mGMSB we have chosen a hypothetical future best-fit point with higher mass scales, defined by eq. (3.36). As for the CMSSM,

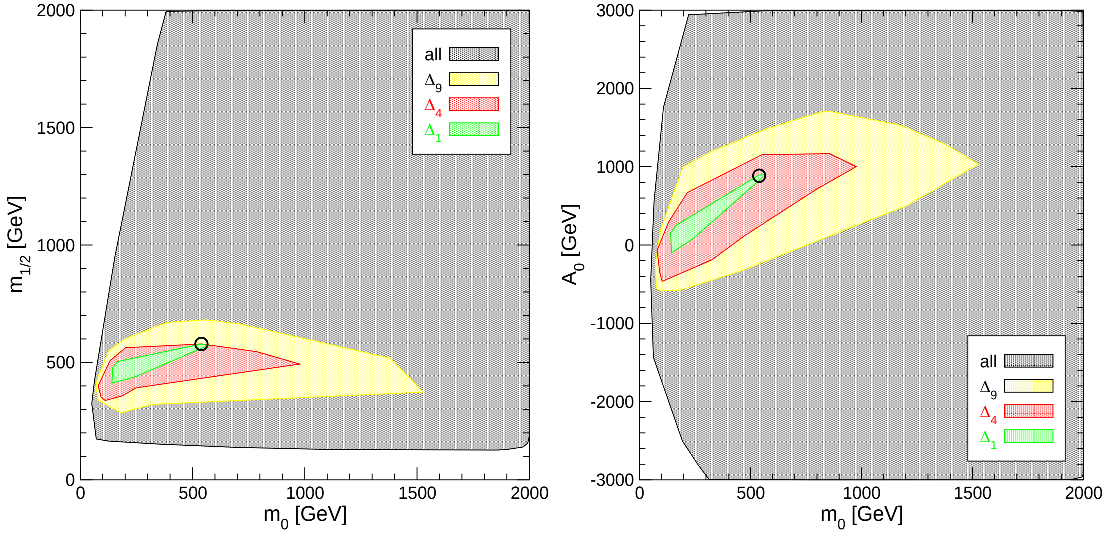

Figure 3.18: Future projection for the $\Delta_{1,4,9}$ regions in the m_0–$m_{1/2}$ plane (left) and in the m_0–A_0 plane (right) in the CMSSM assuming that the future experimental data agree exactly with the current best-fit point. The color code is as in Fig. 3.7.

we assume that the future experimental values agree exactly with the low-energy parameters corresponding to eq. (3.36). The reduction of the $\Delta_{1,4,9}$ regions can be observed in Fig. 3.21. It is at the same level as for the current best-fit point in Fig. 3.20. These results are also shown in the $N_{\rm mess}$–Λ plane in Fig. 3.23, where the same sensitivity is found as for the current best-fit point displayed in Fig. 3.22.

mAMSB

In Fig. 3.24 we show the only high-energy parameter plane in the mAMSB, $m_{\rm aux}$ vs. m_0, with the same color coding as in Fig. 3.7. Within this scenario the precision observables will allow an extremely precise determination of the high-energy parameters. For the case that the current best-fit point agrees exactly with the future measurements, at the $\Delta\chi^2 = 9$ level $m_{\rm aux}$ is determined to $\pm 3 \times 10^3$ GeV, i.e. to $\sim 10\%$. The absolute precision for m_0 is ± 100 GeV, whereas the relative precision

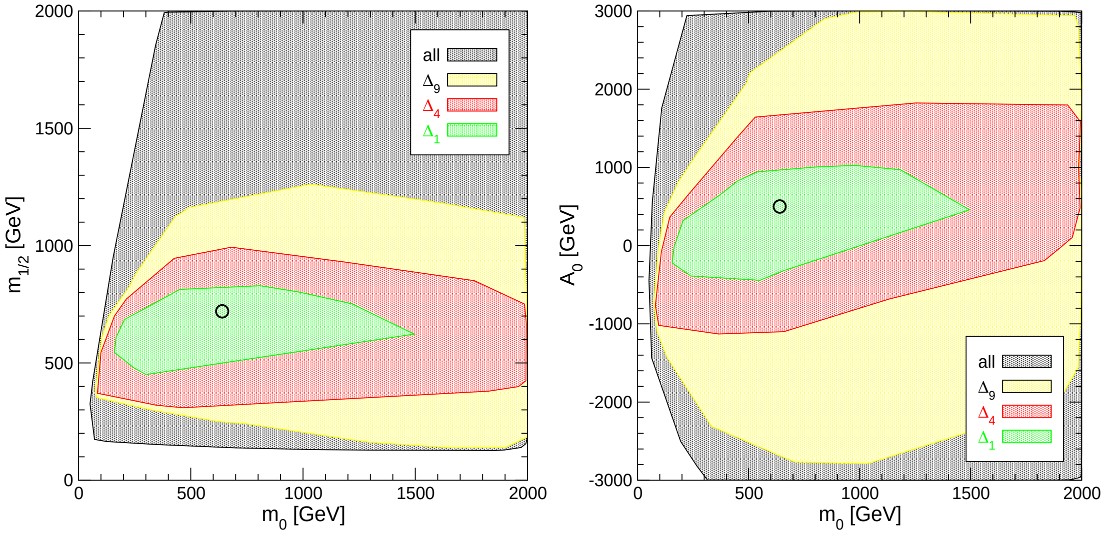

Figure 3.19: Future projection for the $\Delta_{1,4,9}$ regions in the m_0–$m_{1/2}$ plane (left) and in the m_0–A_0 plane (right) in the CMSSM assuming that the future experimental data agree exactly with a hypothetical best-fit point as specified in eq. (3.35). The color code is as in Fig. 3.7.

reaches only $\sim 30\%$. (The Δ_4 and Δ_1 regions are very small and nearly invisible inside (by definition) the Δ_9 region.) This result is to a large extent due to the fact that the $\tan\beta$ value for the current best-fit point is relatively low (see also the discussion of the hypothetical best-fit point below).

As for the other two scenarios, also in mAMSB we have chosen a hypothetical future best-fit point with higher mass scales, defined by eq. (3.37). It should be noted that for mAMSB the increase in M_A from the current best-fit point to the hypothetical best-fit point is a bit smaller than in the other two scenarios, while the shift in $\tan\beta$ is substantially larger. Again we assume that the future experimental values agree exactly with the low-energy parameters corresponding to eq. (3.37). We show the preferred parameter space for this hypothetical point in Fig. 3.25. The reduction in the size of the $\Delta_{1,4,9}$ regions compared to the present situation is much weaker than for the current best-fit point in Fig. 3.24. At the Δ_9 level no limit on m_0 can be set. This shows that the very high precision obtainable with the current best-fit point is not generally valid in the mAMSB scenario.

3.5.2 Low-energy Analysis

We now turn to the comparison of the three soft SUSY-breaking scenarios in terms of M_A and $\tan\beta$, assuming the future experimental and theory precisions as discussed in Sect. 3.3. In Fig. 3.26 we show the M_A–$\tan\beta$ plane for the CMSSM (top), mGMSB (middle) and mAMSB (bottom) with the same color coding as in Fig. 3.7. In each scenario we assume that the future measurements will agree exactly with the current best-fit point.

A drastic improvement compared to the present situation can be observed in all three scenarios. However, also for the low-energy parameters the quality of the improvement going to the future sensitivities depends on the fact that currently relatively low mass scales are favored, see below. The results look quite different in mAMSB as compared to the CMSSM and mGMSB. Within the latter two the Δ_9 region is confined to $M_A \lesssim 1000$ GeV with a width of 300(400) GeV for the CMSSM (mGMSB), whereas $\tan\beta$ is only weakly restricted, $10(20) \lesssim \tan\beta \lesssim 60$. Within mAMSB, as for the high-energy parameters, a very precise indirect determination of M_A and $\tan\beta$ can be performed. At the $\Delta\chi^2 = 9$ level M_A is confined to ± 50 GeV, i.e. to about 6%. $\tan\beta$ is determined to ± 3, corresponding to a precision of $\sim 8\%$. However, as discussed in Sect. 3.5.1, this is largely due to the relatively small value of $\tan\beta$ within the mAMSB scenario at the current best-fit point.

We finally investigate the future sensitivity of the three soft SUSY-breaking scenarios for the hypothetical best-fit point. In Fig. 3.27 we show the results for the hypothetical best-fit points as defined in eqs. (3.35), (3.36), (3.37) for the CMSSM, mGMSB and mAMSB, respectively. By definition, see eq. (3.34), the hypothetical best-fit values for M_A and $\tan\beta$ are very similar in the three scenarios, $M_A \approx 800$ GeV and $\tan\beta \approx 40$. These M_A values are somewhat larger than the current best-fit values, see Tab. 3.1. In combination with $\tan\beta \approx 40$ such heavy MSSM Higgs bosons could not be detected at the LHC [237, 238, 239, 240, 241, 242, 244] or the ILC [216, 217, 218, 219]. Despite the fact that these values are already in the decoupling regime (i.e. where SUSY masses are large and loop effects are correspondingly small), the precision observables are still able to provide upper (and lower) limits on M_A and $\tan\beta$ with similar results in the three soft SUSY-breaking scenarios. The upper limit at the $\Delta\chi^2 = 9$ level on M_A varies between $\sim$ 2000 GeV in the CMSSM and $\sim$ 1400 GeV in mGMSB. This means that the limits obtainable for M_A and $\tan\beta$ depend only to a small extent on the details of the underlying physics scenario and can thus be viewed as a more general result for scenarios resulting from a high-scale theory. In conclusion, the precision observables could allow one to set an indirect bound on M_A (and mildly also on $\tan\beta$) beyond the direct collider reach. This sensitivity would improve even more if the future collider data (SUSY masses, etc.) would be included (see e.g. Ref. [247]). Such an analysis, however, would at the present state be highly speculative and is beyond the scope of our study.

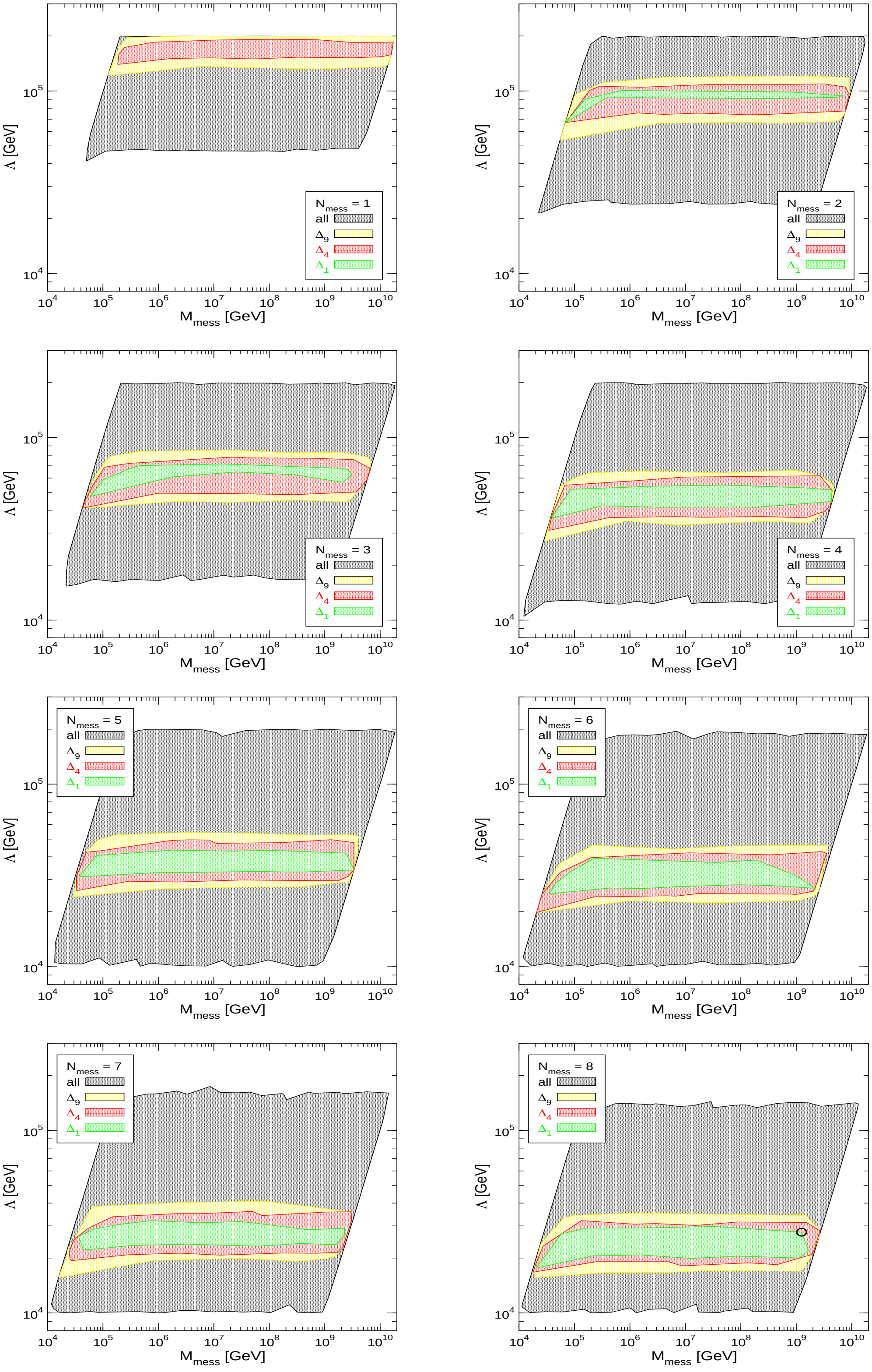

Figure 3.20: Future projection for the $\Delta_{1,4,9}$ regions in the Λ–$M_{\rm mess}$ plane for the $N_{\rm mess} = 1\ldots8$ in the mGMSB assuming that the future experimental data agree exactly with the current best-fit point (marked by a circle). The color coding is as in Fig. 3.7.

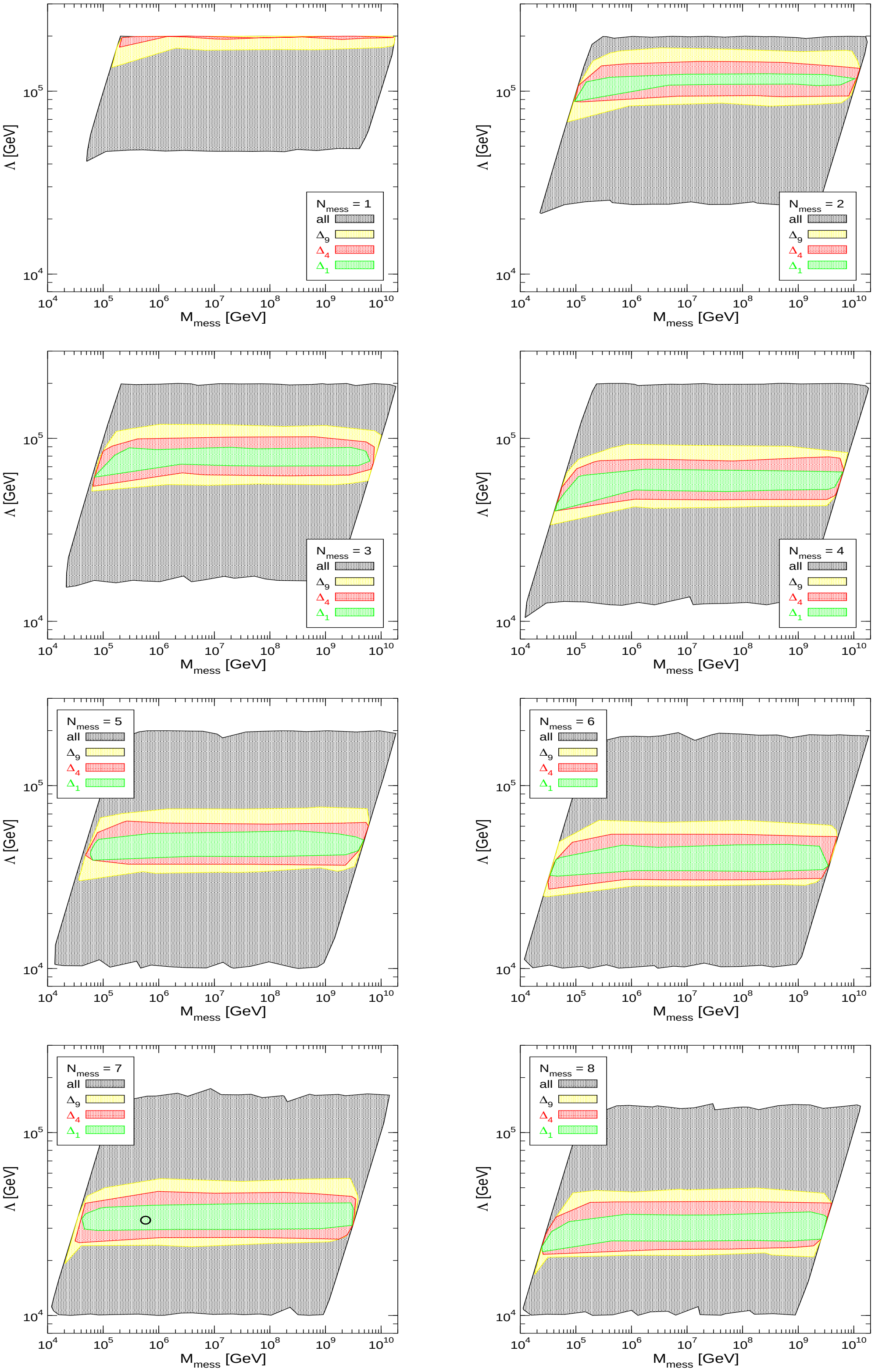

Figure 3.21: Future projection for the $\Delta_{1,4,9}$ regions in the Λ–$M_{\rm mess}$ plane for the $N_{\rm mess} = 1 \ldots 8$ in the mGMSB assuming that the future experimental data agree exactly with the hypothetical best-fit point as defined in eq. (3.36) (marked by a circle). The color coding is as in Fig. 3.7.

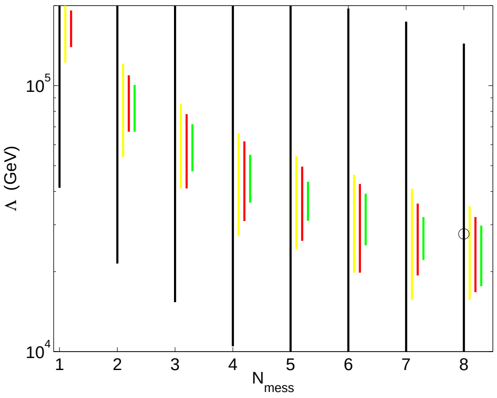

Figure 3.22: Future projection for the $\Delta_{1,4,9}$ regions in the N_{mess}–Λ plane in the mGMSB assuming that the future experimental data agree exactly with the current best-fit point (marked by a circle). The color coding is as in Fig. 3.7.

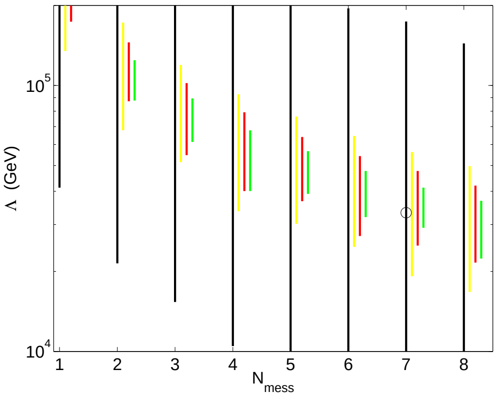

Figure 3.23: Future projection for the $\Delta_{1,4,9}$ regions in the N_{mess}–Λ plane in the mGMSB assuming that the future experimental data agree exactly with the hypothetical best-fit point as defined in eq. (3.36) (marked by a circle). The color coding is as in Fig. 3.7.

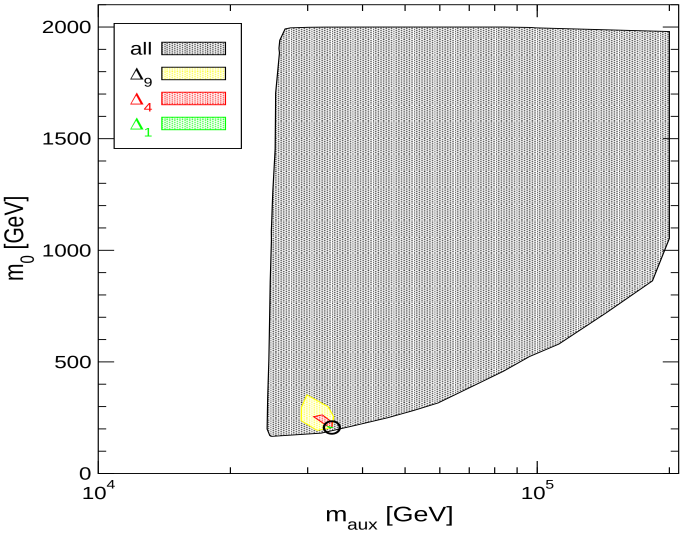

Figure 3.24: Future projection for the $\Delta_{1,4,9}$ regions in the $m_{\rm aux}$–m_0 plane in the mAMSB assuming that the future experimental data agree exactly with the current best-fit point. The color coding is as in Fig. 3.7.

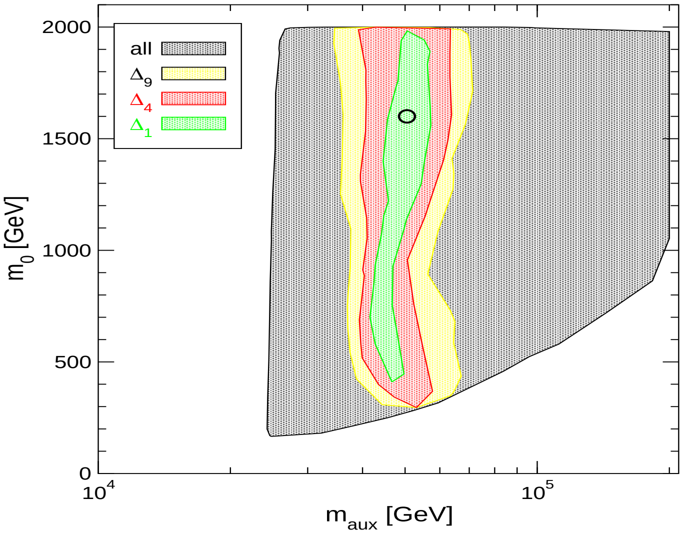

Figure 3.25: Future projection for the $\Delta_{1,4,9}$ regions in the $m_{\rm aux}$–m_0 plane in the mAMSB assuming that the future experimental data agree exactly with the hypothetical best-fit point as defined in eq. (3.37) The color coding is as in Fig. 3.7.

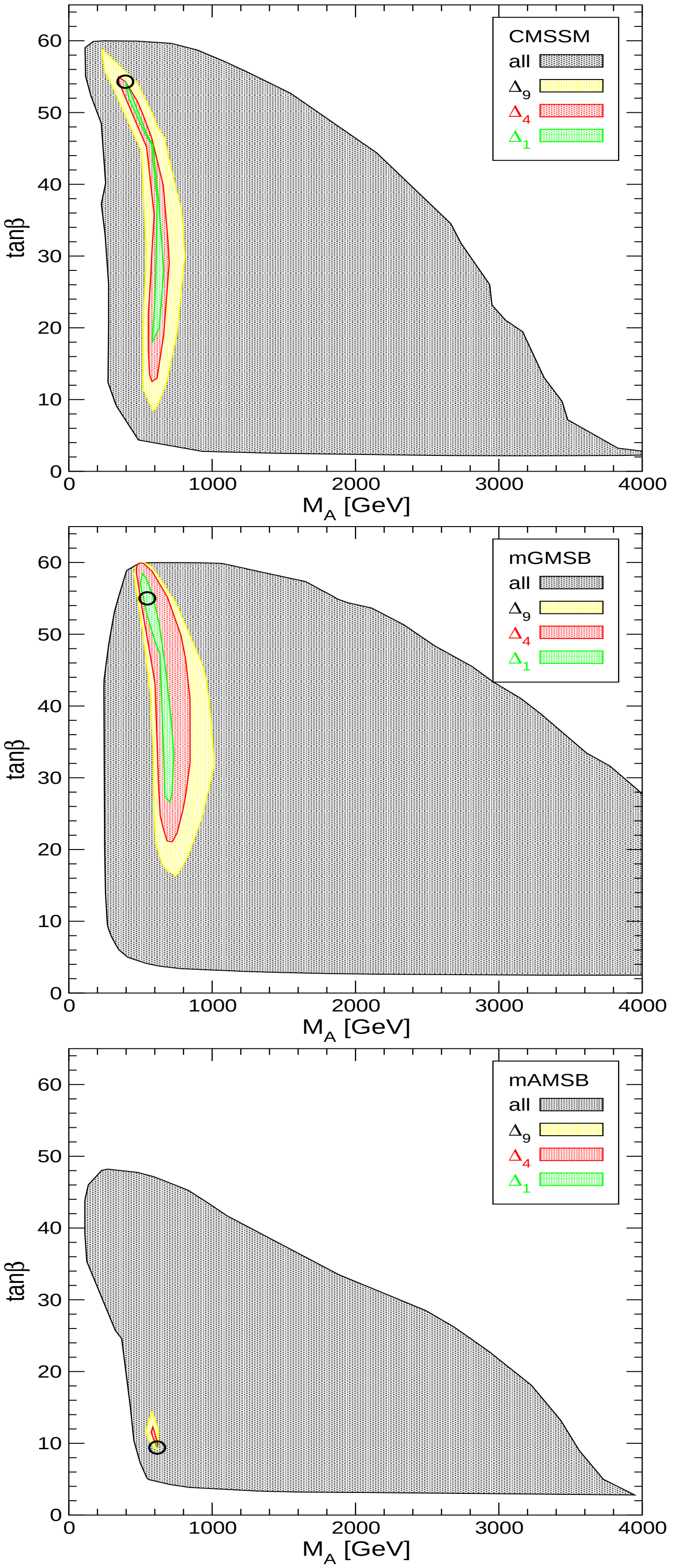

Figure 3.26: Future projection for the $\Delta_{1,4,9}$ regions in the M_A–$\tan\beta$ planes in the CMSSM (top), mGMSB (middle) and mAMSB (bottom) assuming that the future measurements will agree exactly with the current best-fit point. The color coding is as in Fig. 3.7.

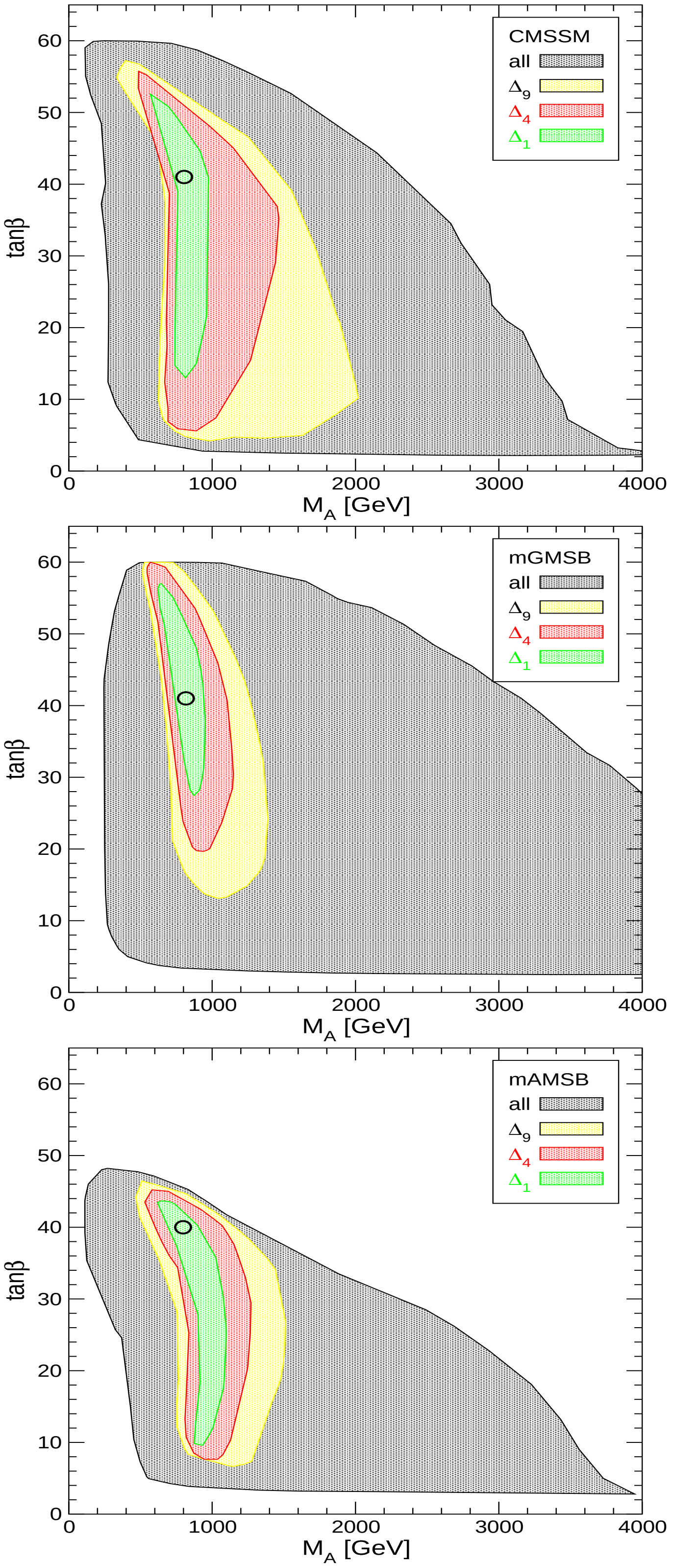

Figure 3.27: Future projection for the $\Delta_{1,4,9}$ regions in the M_A–$\tan\beta$ planes in the CMSSM (top), mGMSB (middle) and mAMSB (bottom) assuming the hypothetical future best fit points defined eqs. (3.35), (3.36), (3.37) for the CMSSM, mGMSB and mAMSB, respectively. The color coding is as in Fig. 3.7.

3.6 Conclusions

We investigated the constraints arising from electroweak precision observables (EWPO) and B-physics observables (BPO) providing a comparison of the CMSSM, the mGMSB and the mAMSB. We performed a χ^2 analysis based on the mass of the W boson, M_W, the effective weak leptonic mixing angle, $\sin^2\theta_{\mathrm{eff}}$, the anomalous magnetic moment of the muon $(g-2)_\mu$, the mass of the lightest CP-even MSSM Higgs boson, M_h, as well as on $\mathrm{BR}(b \to s\gamma)$ and $\mathrm{BR}(B_s \to \mu^+\mu^-)$. Our analysis should be viewed as an exploratory study for the comparison of the scenarios, providing a starting point for a more refined investigation using more precision data and an elaborate χ^2 analysis [111].

Our results are analyzed separately in terms of the high-scale parameters of the respective model as well as in terms of low-energy parameters such as M_A, $\tan\beta$ and SUSY particle masses. Using todays measurements, uncertainties and exclusion bounds, we find that relatively low mass scales in all three scenarios are favored at the level of $\Delta\chi^2 < 1$ or 4. However, the current data of EWPO and BPO can hardly set any upper bound on the SUSY mass scales at the level of $\Delta\chi^2 = 9$. The best fit-values for M_A range from ~ 400 GeV in the CMSSM up to ~ 600 GeV in mAMSB, whereas the $\tan\beta$ values are only weakly constrained. Remarkably the mAMSB scenario, despite having one free GUT scale parameter less than the other two scenarios, has a somewhat lower total minimum χ^2. This can be traced back to a better agreement with the combination of the $\mathrm{BR}(b \to s\gamma)$ and $(g-2)_\mu$ measurements (with some help from M_W) for a heavier scalar quark spectrum and a corresponding slightly larger value of M_h.

We presented predictions for the lightest CP-even Higgs boson mass, based on the current χ^2 data, but without imposing the current LEP bound from Higgs boson searches and its corresponding χ^2 contribution. Best-fit values of $M_h \sim 105$ GeV are found for the CMSSM and mGMSB, and $M_h \sim 113$ GeV for mAMSB. In all three scenarios a relatively good compatibility with the direct bounds from the Higgs searches at LEP is found. Within mAMSB the $\Delta\chi^2 < 1$ region extends up to

$M_h \lesssim 122$ GeV.

We also presented the predictions for the masses of various SUSY particles such as $m_{\tilde{t}_1}$, $m_{\tilde{t}_2}$, $m_{\tilde{b}_1}$, $m_{\tilde{b}_2}$, $m_{\tilde{\tau}_1}$, $m_{\tilde{\tau}_2}$, $m_{\tilde{\chi}_1^0}$, $m_{\tilde{\chi}_2^0}$, $m_{\tilde{\chi}_1^\pm}$ and $m_{\tilde{g}}$ in the three soft SUSY-breaking scenarios. As a general feature lowest masses are found in the mAMSB and heaviest in mGMSB. All three scenarios offer good prospects for the discovery of some color-neutral particles at the ILC (with a center-of-mass energy up to $\sqrt{s} = 1$ TeV) and for colored particles at the LHC. There are also good prospects for the discovery of uncolored particles such as charginos, neutralinos and light sleptons, especially if they are produced in cascade decays. Some part of the preferred parameter space in the three scenarios is currently probed at the Tevatron. Within the CMSSM qualitative agreement in the preferred mass ranges with previous analyses [104, 105, 106] has been found.

Finally, we explored the projection for the future sensitivities of the EWPO and BPO in the three soft SUSY-breaking scenarios. Here we also assumed a measurement of the lightest MSSM Higgs boson mass. In a first step we analyzed the future sensitivities assuming that the future measurements agree with the current best-fit results. We found a strong improvement with respect to the current sensitivity. Within the mAMSB scenario M_A and $\tan\beta$ can be determined indirectly with very high precision, largely due to the fact that the current best-fit point has a relatively low $\tan\beta$ value. On the other hand, in the CMSSM and mGMSB the $\tan\beta$ determination remains relatively weak, where the current best-fit points have very large $\tan\beta$ values. In a second step we assumed that the future measurements will agree in each scenario with a certain hypothetical point. These three points were defined for each scenario such that they result in a similar Higgs and SUSY spectrum with $M_A \approx 800$ GeV and $\tan\beta \approx 40$. In general the Higgs and SUSY mass scales are somewhat higher than for the current best-fit points, i.e. loop corrections are correspondingly somewhat smaller. These points would not permit a direct determination of the heavy Higgs-boson mass scale. We find that the EWPO and BPO exhibit a similar future sensitivity in the CMSSM, mGMSB and mAMSB giving rise to an upper limit on the high-scale parameters at the $\Delta\chi^2 = 9$ level. The future EWPO and BPO sensitivities depend only mildly on the underlying physics scenario. The precision observables could allow one to constrain the Higgs sector parameters even beyond the direct reach of the LHC or the ILC.

Once LHC (and ILC) data on SUSY masses will be available, the assumption about the underlying scenario itself will be investigated. While information from the direct production of SUSY particles will obviously be crucial for disentangling the underlying scenario of SUSY-breaking, also the EWPO and BPO will certainly play an important role in this context.

CHAPTER 4

CONCLUSIONS

In this work, we have presented studies on prospects of direct and indirect searches for new physics beyond the SM. We showed that with the help of the LHC, it is possible to uncover certain proposed extensions of the SM. Also, we demonstrated the use of precision observables in investigating new physics at much higher scales (SUSY-breaking mechanisms for example).

Extensions of the SM often postulate existence of new particles that are not present in the SM. Studies of the collider signatures of these new particles provide strong evidences in validating/vetoing the conjectured models. In Chapter 2, we concluded that an IDM signal in the dilepton channel with a significance of more than 3σ should be apparent at the LHC with less than 100 fb^{-1} of integrated luminosity. Moreover, the trilepton channel provides additional information about the IDM and we showed that it is possible, in certain range of the IDM parameter space, to resolve the trilepton signal with 300 fb^{-1} of integrated luminosity. We also carried out studies on the LRTH model and found that with a luminosity of 30 fb^{-1} at the early stage of the LHC operation, the LRTH heavy top T can be observed at a significance level above 5σ. Our investigations demonstrated the comprehensive and systematic approach that collider studies on new physics models should follow.

In Chapter 3, we investigated the constraints arising from electroweak precision observables (EWPO) and B-physics observables (BPO) and provided a comparison of the CMSSM, the mGMSB and the mAMSB. We presented predictions from a χ^2 analysis based on the mass of the W boson, M_W, the effective weak leptonic mixing angle, $\sin^2\theta_{\text{eff}}$, the anomalous magnetic moment of the muon $(g-2)_\mu$, the mass of the lightest *cp*-even MSSM Higgs boson, M_h, as well as on $\text{BR}(b \to s\gamma)$ and $\text{BR}(B_s \to \mu^+\mu^-)$. We also explored the projection for the future sensitivities of the EWPO and BPO in the three soft SUSY-breaking scenarios and found that within the mAMSB scenario M_A and $\tan\beta$ can be determined indirectly with very high precision. With improved EWPO and BPO, further information can be extracted on the three competing SUSY-breaking scenarios, using a similar framework to our study.

We are entering into an exciting era of great(er) experimental achievement, with the LHC currently running in the TeV territory and the precision observables advancing into another level. Armed with the approach and framework presented in this work, we anticipate further and deeper insight into new physics beyond the SM.

REFERENCES

[1] K.Nakamura et al. *J. Phys. G*, 37:075021, 2010.

[2] A.Salam and J.C.Ward. *Nuovo Cim*, 19:165, 1961.

[3] C.N.Yang and R.L.Mills. *Phys. Rev.*, 96:191, 1954.

[4] A.Salam and J.C.Ward. *Phys. Lett.*, 13:168, 1964.

[5] S.L.Glashow. *Nucl. Phys.*, 22:579, 1961.

[6] S.Weinberg. *Phys. Rev. Lett.*, 155:1554, 1967.

[7] Y.Nambu. *Phys. Rev.*, 117:648, 1960.

[8] Y.Nambu. *Phys. Rev. Lett.*, 4:380, 1960.

[9] J.Goldstone. *Nuovo Cim.*, 19:154, 1961.

[10] J.Goldstone, A.Salam, and S.Weinberg. *Phys. Rev.*, 127:965, 1962.

[11] P.W.Higgs. *Phys. Lett.*, 12:132, 1964.

[12] P.W.Higgs. *Phys. Rev.*, 145:1156, 1966.

[13] F.Abe et al. *Phys. Rev. Lett.*, 74:2626, 1995.

[14] M.Awramil, M.Czakon, et al. *Phys. Rev. D*, 69:053006, 2004.

[15] M.Martinez, R.Miquel, L.Rolandi, and R.Tenchini. *Rev. Mod. Phys.*, 71:575, 1999.

[16] A.Czarnecki and W.J.Marciano. *Phys. Rev. D*, 64:013014, 2001.

[17] S.P.Martin. “A SUSY Primer”. *in Kane, G.L. (ed.): Perspectives on supersymmetry II, arXiv:hep-ph/9709356.*

[18] K.R.Dienes, E.Dudas, and T.Gherghetta. *Nucl. Phys. B*, 537:47, 1999.

[19] N.Arkani-Hamed, S.Dimopoulos, and G.R.Dvali. *Phys. Lett. B*, 429:263, 1998.

[20] L.Randall and R.Sundrum. *Phys. Rev. Lett*, 83:3370, 1999.

[21] C.T.Hill and E.H.Simmons. *Phys. Rept.*, 381:235, 2003.

[22] S.Dawson. “Introduction to electroweak symmetry breaking”. *arXiv:hep-ph/9901280v1.*

[23] K.Wilson. *Phys. Rev. B*, 4:3184, 1971.

[24] K.Wilson and J.Kogut. *Phys. Rep.*, 12:75, 1974.

[25] M.E.Peskin and T.Takeuchi. *Phys. Rev. Lett.*, 65:964, 1991.

[26] R.Barbieri. *IVth Rencontres du Vietnam*, 2000.

[27] N.Arkani-Hamed, A.G.Cohen, and H.Georgi. *Phys. Lett. B*, 513:232, 2001.

[28] H.Georgi and A.Pais. *Phys. Rev. D*, 10:539, 1974.

[29] H.Georgi and A.Pais. *Phys. Rev. D*, 12:508, 1975.

[30] H.C.Cheng and I.Low. *JHEP*, 09:051, 2003.

[31] H.C.Cheng and I.Low. *JHEP*, 08:061, 2004.

[32] H.C.Cheng, I.Low, and L.T.Wang. *Phys. Rev. D*, 74:055001, 2006.

[33] Z.Chacko, H.S.Goh, and R.Harnik. *Phys. Rev. Lett.*, 96:231802, 2006.

[34] R.Barbieri, T.Gregoire, and L.J.Hall. *Report: CERN-PH-TH*, 2005.

[35] Z.Chacho, Y.Nomura, M.Rapucci, and G.Perez. *JHEP*, 126:0601, 2006.

[36] Z.Chacko, H.S.Goh, and R.Harnik. *JHEP*, 01:108, 2006.

[37] G.Bertone, D.Hooper, and J.Silk. *Phys. Rep.*, 405:279, 2005.

[38] E.Lundstrom, M.Gustafsson, and J.Edsjo. *Phys. Rev. D*, 79:035013, 2009.

[39] A.Mazumdar. "The origin of dark matter, matter-anti-matter asymmetry, and inflation". *to be published in Rev. Mod. Phys, arXiv:hep-ph/1106.5408.*

[40] E.Witten. *Nucl. Phys. B*, 188:513, 1981.

[41] M.Veltman. *Act. Phys. Polon. B*, 12:437, 1981.

[42] R.Kaul. *Phys. Lett. B*, 109:19, 1982.

[43] S.Dimopoulos and D.Sutter. *Nucl. Phys. B*, 452:496, 1995.

[44] P.Fayet and J.Iliopoulos. *Phys. Lett. B*, 51:461, 1974.

[45] L.O'Raifeartaigh. *Nucl. Phys. B*, 96:331, 1975.

[46] M.Frank, T.Hahn, S.Heinemeyer, W.Hollik, H.Rzehak, and G.Weiglein. *JHEP*, 0702:047, 2007.

[47] L.Randall and R.Sundrum. *Nucl. Phys. B*, 557:79, 1999.

[48] G.F.Giudice, M.A.Luty, H.Murayama, and R.Rattazi. *JHEP*, 9812:027, 1998.

[49] J.F.Gunion, R.Vega, and J.Wudka. *Phys. Rev. D*, 42:1673, 1990.

[50] E.Ma. *Phys. Rev. D*, 73:077301, 2006.

[51] T.Hambye and M.H.G.Tytgat. *Phys. Lett. B*, 659:651, 2008.

[52] R.Barbieri, L.J.Hall, and V.S.Rychkov. *Phys. Rev. D*, 74:015007, 2006.

[53] Q.H.Cao and E.Ma. *Phys. Rev. D*, 76:095011, 2007.

[54] Z.Charcko, H.S.Goh, and R.Harnik. *Phys. Rev. Lett.*, 96:231802, 2006.

[55] Z.Charcko, H.S.Goh, and R.Harnik. *JHEP*, 01:108, 2006.

[56] K.M.Cheung. *Phys. Lett. B*, 517:167, 2001.

[57] X.Miao, S.Su, E.Dolle, and B.Thomas. *Phys. Rev. D*, 82:035009, 2010.

[58] E.Dolle, X.Miao, S.Su, and B.Thomas. *Phys. Rev. D*, 81:035003, 2010.

[59] S.Heinemeyer, X.Miao, S.Su, and G.Weiglein. *JHEP*, 0808:087, 2008.

[60] N.G.Deshpande and E.Ma. *Phys. Rev. D*, 18:2574, 11978.

[61] M.E.Peskin and T.Takeuchi. *Phys. Rev. D*, 46:381, 1992.

[62] M.W.Grunewald. *J. Phys. Conf. Ser*, 110:042008, 2008.

[63] M.Lisanti and J.G.Wacker. *arXiv:0704.2816v2 [hep-ph]*.

[64] L.Lopez Honorez, E.Nezri, J.F.Oliver, and M.H.G.Tytgat. *JCAP*, 0702:028, 2007.

[65] E.M.Dolle and S.Su. *Phys. Rev. D*, 80:055012, 2009.

[66] P.Agrawal, E.M.Dolle, and C.A.Krenke. *Phys. Rev. D*, 79:015015, 2009.

[67] E.Nezri, M.H.G.Tytgat, and G.Vertongen. *JCAP*, 0904:014, 2009.

[68] M.Gustafsson, E.Lundstrom, L.Bergstrom, and J.Edsjo. *Phys. Rev. Lett.*, 99:041301, 2007.

[69] E.Dolle and S.Su. *Phys. Rev. D*, 77:075013, 2008.

[70] D.Majumdar and A.Ghosal. *Mod. Phys. Lett. A*, 23:2011, 2008.

[71] Q.H.Cao, E.Ma, and G.Rajasekaran. *Phys. Rev. D*, 76:095011, 2007.

[72] W.M.Yao et al. *J. Phys. G*, 33:1, 2006.

[73] [LEP Higgs Working for Higgs boson searches, ALEPH Collaboration, DELPHI Collaboration, CERN-L3 Collaboration, and OPAL Collaboration].

arXiv:hep-ex/0107032.

[74] [LEP Higgs Working Group for Higgs boson searches, ALEPH Collaboration, ALEPH Collaboration, DELPHI Collaboration, L3 Collaboration, and OPAL Collaboration]. *arXiv:hep-ex/0107031.*

[75] A.Abulencia et al. *Phys. Rev. Lett*, 96:042003, 2006.

[76] M.Acciarri et al. *Phys. Lett. B*, 472:420, 2000.

[77] [The LEP SUSY Working Group]. *http://lepsusy.web.cern.ch/lepsusy/, LEPSUSYWG/01-03.1.*

[78] A.Pierce and J.Thaler. *JHEP*, 0708:026, 2007.

[79] [ALEPH Collaboration, DELPHI Collaboration, L3 Collaboration, OPAL Collaboration, SLD Collaboration, LEP Electroweak Working Group, SLD Electroweak Group, and SLD Heavy Flavour Group]. *Phys. Rept.*, 427:257, 2006.

[80] D.N.Spergel et al. *Astrophys. J. Suppl.*, 148:175, 2003.

[81] R.Arnowitt and P.Nath. *Mod. Phys. Lett. A*, 2:3311, 1987.

[82] K.T.Matchev and D.M.Pierce. *Phys. Lett. B*, 467:225, 1999.

[83] J.Alwall et al. *JHEP*, 0709:028, 2007.

[84] T.Sjostrand, S.Mrenna, and P.Skands. *JHEP*, 0605:026, 2006.

[85] “PGS: Pretty Good Simulator”. *http://www.physics.ucdavis.edu/.*

[86] [ATLAS Collaboration]. *ATLAS-TDR-14*, 1999.

[87] G.L.Bayatian et al. *J. Phys. G*, 34:995, 2007.

[88] O.J.P.Eboli and D.Zeppenfeld. *Phys. Lett. B*, 495:147, 2000.

[89] Z.Sullivan and E.L.Berger. *Phys. Rev. D*, 78:034030, 2008.

[90] H.Baer, C.h.Chen, F.Paige, and X.Tata. *Phys. Rev. D*, 50:4508, 1994.

[91] H.C.Goh and S.Su. *Phys. Rev. D*, 75:075010, 2007.

[92] P.Meade and M.Reece. “BRIDGE: Branching Ratio Inquiry / Decay Generated Events”. *arXiv:hep-ph/0703031v2.*

[93] M.L.Mangano, M.Moretti, F.Piccinini, R.Pittau, and A.Polosa. *JHEP*, 0307:001, 2003.

[94] H.Nilles. *Phys. Rept.*, 110:1, 984.

[95] H.Haber and G.kane. *Phys. Rept.*, 17:85, 1985.

[96] [Heavy Flavor Analysis Group]. *http://www.slac.standanfor.edu/xorg/hfag.*

[97] J.Ellis, S.Kelley, and D.Nanopoulos. *Phys. Lett. B*, 260:131, 1991.

[98] M.Dine, W.Fischler, and M.Srednicki. *Nucl. Phys. B*, 189:575, 1981.

[99] M.Dine and A.Nelson. *Phys. Rev. D*, 48:1277, 1993.

[100] G.Giudice and R.Rattazzi. *Phys.Rept.*, 322:419, 1999.

[101] L.Randall and R.Sundrum. *Nucl. Phys. B*, 557:79, 1999.

[102] G.Giudice, M.Luty, H.Murayama, and R.Rattazzi. *JHEP*, 9812:027, 1998.

[103] T.Gherghetta, G.Giudice, and J.Wells. *Nucl. Phys. B*, 559:27, 1999.

[104] J.Ellis, S.Heinemeyer, K.Olive, and G.Weiglein. *JHEP*, 0502:013, 2005.

[105] J.Ellis, S.Heinemeyer, K.Olive, and G.Weiglein. *JHEP*, 0605:005, 2006.

[106] J.Ellis, S.Heinemeyer, K.Olive, A.M.Weber, and G.Weiglein. *JHEP*, 0708:083, 2007.

[107] J.Ellis, T.Hahn, S.Heinemeyer, K.Olive, and G.Weiglein. *JHEP*, 0710:092, 2007.

[108] J.Ellis, S.Heinemeyer, K.Olive, and G.Weiglein. *Phys. Lett. B*, 653:292, 2007.

[109] J.Ellis, K.Olive, Y.Santoso, and V.Spanos. *Phys. Rev. D*, 69:095004, 2004.

[110] G.Isidori, F.Mescia, P.Paradisi, and D.Temes. *Phys. Rev. D*, 75:115019, 2007.

[111] O.Buchmueller et al. *Phys. Lett. B*, 657:87, 2007.

[112] S.Heinemeyer, M.Mondrag'on, and G.Zoupanos. *JHEP*, 0135:007, 2008.

[113] F.Mahmoudi. *JHEP*, 0712:026, 2007.

[114] F.Domingo and U.Ellwanger. *JHEP*, 0712:090, 2007.

[115] J.Kasahara, K.Freese, and P.Gondolo. *Phys. Rev. D*, 79:045020, 2009.

[116] C.Bennett et al. *Astrophys. J. Suppl.*, 148:1, 2003.

[117] A.Arbey and F.Mahmoudi. *Phys. Lett. B*, 669:46, 2008.

[118] Herbi Dreiner. "an introduction to explicit r-parity violation"". *Pramana*, 51:123–133, 1998. 10.1007/BF02827485.

[119] D.Lyth and E.Stewart. *Phys. Rev. D*, 53:1784, 1996.

[120] G.Gelmini and P.Gondolo. *Phys. Rev. D*, 74:023510, 2006.

[121] G.Degrassi, P.Gambino, and P.Slavich. *Phys. Lett. B*, 635:335, 2006.

[122] H.Nilles. *Phys. Lett. B*, 115:193, 1982.

[123] A.Lahanas and D.Nanopoulos. *Phys. Rept.*, 145:1, 1987.

[124] W.Yao et al. *J. Phys. G*, 33:1, 2006.

[125] H.Murayama and Y.Nomura. *Phys. Rev. Lett.*, 98:151803, 2007.

[126] J.Jaeckel S.Abel, C.Durnford and V.V.Khoze. *JHEP*, 0802:074, 2008.

[127] P.Fayet. *Phys. Lett. B*, 70:461, 1977.

[128] A.Pomarol and R.Rattazzi. *JHEP*, 9905:013, 1999.

[129] Z.Chacko, M.Luty, and E.Ponton. *JHEP*, 0004:001, 2000.

[130] E.Katz, Y.Shadmi, and Y.Shirman. *JHEP*, 9908:015, 1999.

[131] I.Jack, D.Jones, and R.Wild. *Phys. Lett. B*, 193:2002, 535.

[132] B.Allanach. *Comput. Phys. Commun.*, 143:305, 2002.

[133] S.Heinemeyer, W.Hollik, and G.Weiglein. *Phys. Rept.*, 425:265, 2006.

[134] S.Heinemeyer, W.Hollik, A.M.Weber, and G.Weiglein. *JHEP*, 0804:039, 2008.

[135] E.Brubaker and others [Tevatron Electroweak Working Group]. *arXiv:hep-ex/0608032*.

[136] [Tevatron Electroweak Working Group]. *arXiv:hep-ex/0803.1683*.

[137] A.Sirlin. *Phys. Rev. D*, 22:971, 1980.

[138] P.Chankowski, A.Dabelstein, W.Hollik, W.Mosle, S.Pokorski, and J.Rosiek. *Nucl. Phys. B*, 417:101, 1994.

[139] D.Garcia and J.Solà. *Mod. Phys. Lett. A*, 9:211, 1994.

[140] A.Djouadi and C.Verzegnassi. *Phys. Lett. B*, 195:265, 1987.

[141] B.Kniehl. *Nucl. Phys. B*, 347:89, 1990.

[142] K.Chetyrkin, J.Kuhn, and M.Steinhauser. *Phys. Rev. Lett.*, 75:3394, 1995.

[143] K.Chetyrkin, J.Kuhn, and M.Steinhauser. *Nucl. Phys. B*, 482:213, 1996.

[144] A.Djouadi, P.Gambino, S.Heinemeyer, W.Hollik, C.Junger, and G.Weiglein. *Phys. Rev. Lett.*, 78:3826, 1997.

[145] J.Haestier, S.Heinemeyer, D.Stockinger, and G.Weiglein. *JHEP*, 0512:027, 2005.

[146] M.Veltman. *Nucl. Phys. B*, 123:89, 1977.

[147] S.Heinemeyer, W.Hollik, D.Stockinger, A.M.Weber, and G.Weiglein. *JHEP*, 0608:052, 2006.

[148] A.Hoang et al. *Eur. Phys. J. direct C*, 2:1, 2000.

[149] M.Martinez and R.Miquel. *Eur. Phys. J. C*, 27:49, 2003.

[150] F.Jegerlehner. *JHEP*, 09:075, 2003.

[151] S.Heinemeyer, S.Kraml, W.Porod, and G.Weiglein. *JHEP*, 0309:075, 2003.

[152] [The ALEPH, DELPHI, L3, OPAL, SLD Collaborations, the LEP Electroweak Working Group, the SLD Electroweak, and Heavy Flavour Groups]. *arXiv:hep-ex/050908*.

[153] [LEP Electroweak Working Group]. *http://lepewwg.web.cern.ch/LEPEWWG*.

[154] [Tevatron Electroweak Working Group]. *http://tevewwg.fnal.gov*.

[155] T.Aaltonen et al. *Phys. Rev. Lett.*, 99:151801, 2007.

[156] M.Grunewald. *private communication*.

[157] S.Brensing, S.Dittmaier, M.Kramer, and A.Muck. *Phys. Rev. D*, 77:073006, 2008.

[158] G.Wilson and LC-PHSM-2001-009. *http://www.desy.de/∼lcnotes/notes.html*.

[159] U.Baur, R.Clare, J.Erler, S.Heinemeyer, D.Wackeroth, G.Weiglein, and D.Wood. *WorkShop on the Future of Particle Physics, arXiv:hep-ph/0111314*.

[160] M.Awramik, M.Czakon, A.Freitas, and G.Weiglein. *Phys. Rev. Lett.*, 93:201805, 2004.

[161] R.Hawkings and K.Monig. *Eur. Phys. J. direct C*, 8:1, 1999.

[162] J.Erler, S.Heinemeyer, W.Hollik, G.Weiglein, and P.Zerwas. *Phys. Lett. B*, 486:125, 2000.

[163] A.Czarnecki and W.Marciano. *Phys. Rev. D*, 64:013014, 2001.

[164] M.Knecht. *Lect. Notes Phys.*, 629:37, 2004.

[165] D.Stockinger. *J. Phys. G*, 34:45, 2007.

[166] J.Miller, E.de Rafael, and B.Roberts. *Rept. Prog. Phys.*, 70:795, 2007.

[167] F.Jegerlehner. *Acta Phys. Polon. B*, 38:3021, 2007.

[168] M.Passera, W.Marciano, and A.Sirlin. *Phys. Rev. D*, 78:013009, 2008.

[169] T.Kinoshita and M.Nio. *Phys. Rev. D*, 70:113001, 2004.

[170] M.Passera. *Phys. Rev. D*, 75:013002, 2007.

[171] T.Aoyama, M.Hayakawa, T.Kinoshita, and M.Nio. *Phys. Rev. Lett.*, 99:110406, 2007.

[172] M.Davier, S.Eidelman, A.Hocker, and Z.Zhang. *Eur.Phys.J C*, 31:503, 2006.

[173] K.Hagiwara, A.Martin, D.Nomura, and T.Teubner. *Phys. Rev. D*, 69:093003, 2004.

[174] K.Hagiwara, A.Martin, D.Nomura, and T.Teubner. *Phys. Lett. B*, 649:173, 2007.

[175] S.Ghozzi and F.Jegerlehner. *Phys. Lett. B*, 583:222, 2004.

[176] J.de Troconiz and F.Yndurain. *Phys. Rev. D*, 71:073008, 2005.

[177] M.Davier. *Nucl. Phys. Proc. Suppl.*, 169:288, 2007.

[178] J.Bijnens and J.Prades. *Mod. Phys. Lett A*, 22:767, 2007.

[179] M.Knecht and A.Nyffeler. *Phys. Rev. D*, 65:073034, 2002.

[180] K.Melnikov and A.Vainshtein. *Phys. Rev. D*, 70:113006, 2004.

[181] M.Davier and W.Marciano. *Ann. Rev. Nucl. Part. Sci.*, 54:115, 2004.

[182] H.Hayashii [Belle Collaboration]. *PoS HEP2005*, 2006.

[183] M.Benayoun, P.David, L.DelBuono, O.Leitner, and H.O'Connell. *Eur. Phys. J. C*, 55:155, 2008.

[184] A.Aloisio and others [KLOE Collaboration]. *Phys. Lett.*, 606:12, 2005.

[185] R.Akhmetshin and others [CMD-2 Collaboration]. *Phys. Lett. B*, 578:285, 2004.

[186] M.Achasov et al. *J. Exp. Theor. Phys.*, 101:1053, 2005.

[187] S.Muller. "measurements of radiative processes at kloe". *http://agenda.hep.man.ac.uk/contribution.*

[188] G.Bennett et al. *Phys. Rev. Lett*, 92:161802, 2004.

[189] G.Bennett et al. *Phys. Rev. D*, 73:0702003, 2006.

[190] S.Eidelman. *talk given at the ICHEP06, Moscow, July 2006. http://ichep06.jinr.ru/reports/333_6s1_9p30_Eidelman.pdf.*

[191] T.Moroi. *Phys. Rev. D*, 53:6565, 1996.

[192] J.Lopez, D.Nanopoulos, and X.Wang. *Phys. Rev. D*, 49:366, 1994.

[193] G.Degrassi and G.Giudice. *Phys. Rev. D*, 58:053007, 1998.

[194] S.Heinemeyer, D.Stockinger, and G.Weiglein. *Nucl. Phys. B*, 690:62, 2004.

[195] S.Heinemeyer, D.Stockinger, and G.Weiglein. *Nucl. Phys. B*, 699:103, 2004.

[196] A.Dabelstein. *Nucl. Phys. B*, 456:25, 1995.

[197] S.Heinemeyer, W.Hollik, and G.Weiglein. *Phys. Rev. D*, 58:091701, 1998.

[198] S.Heinemeyer, W.Hollik, and G.Weiglein. *Comput. Phys. Commun.*, 124:76, 2000.

[199] S.Heinemeyer, W.Hollik, and G.Weiglein. *Eur. Phys. J. C*, 9:343, 1999.

[200] G.Degrassi, S.Heinemeyer, W.Hollik, P.Slavich, and G.Weiglein. *Eur. Phys. J. C*, 28:133, 2003.

[201] Y.Okada, M.Yamaguchi, and T.Yanagida. *Prog. Theor. Phys.*, 85:1, 1991.

[202] P.Chankowski, S.Pokorski, and J.Rosiek. *Phys. Lett. B*, 286:307, 1992.

[203] M.Carena, D.Garcia, U.Nierste, and C.Wagner. *Nucl. Phys. B*, 577:577, 2000.

[204] T.Banks. *Nucl. Phys. B*, 303:172, 1988.

[205] G.Degrassi, A.Dedes, and P.Slavich. *Nucl. Phys. B*, 672:144, 2003.

[206] S.Martin. *Phys. Rev. D*, 65:116003, 2002.

[207] S.Martin. *Phys. Rev. D*, 75:055005, 2007.

[208] R.Harlander, P.Kant, L.Mihaila, and M.Steinhauser. *Phys. Rev. Lett.*, 100:191062, 2008.

[209] S.Heinemeyer, W.Hollik, H.Rzehak, and G.Weiglein. *Eur. Phys. J. C*, 39:465, 2005.

[210] B.Allanach, A.Djouadi, J.Kneur, W.Porod, and P.Slavich. *JHEP*, 0409:044, 2004.

[211] S.Heinemeyer, W.Hollik, and G.Weiglein. *JHEP*, 0006:009, 2000.

[212] LEP Higgs working group. *Eur. Phys. J. C*, 47:547, 2006.

[213] LEP Higgs working group. *Phys. Lett. B*, 565:61, 2003.

[214] S.Ambrosanio, A.Dedes, S.Heinemeyer, S.Su, and G.Weiglein. *Nucl. Phys. B*, 624:3, 2001.

[215] J.Ellis, S.Heinemeyer, K.Olive, and G.Weiglein. *Phys. Lett. B*, 515:348, 2001.

[216] J.Aguilar-Saavedra et al. "The TESLA Technical Report". *arXiv:hep-ph/0106315.*

[217] T.Abe and others [American Linear Collider Working Group]. "Linear collider physics resource book for Snowmass 2001. 1: Introduction". *arXiv:hep-ex/0106055.*

[218] K.Abe and others [ACFA Linear Collider Working Group]. "Particle physics experiments at JLC". *arXiv:hep-ph/0109166.*

[219] S.Heinemeyer et al. "Toward high precision Higgs-boson measurements at the International Linear e+ e- Collider". *arXiv:hep-ph/0511332.*

[220] M.Misiak et al. *Phys. Rev. Lett.*, 98:022002, 2007.

[221] T.Hurth, E.Lunghi, and W.Porod. *Nucl. Phys. B*, 704:56, 2005.

[222] M.Neubert. *Eur. Phys. J. C*, 40:165, 2005.

[223] R.Barate et al. *Phys. Lett. B*, 429:169, 1998.

[224] P.Cho, M.Misiak, and D.Wyler. *Phys. Rev. D*, 54:3329, 1996.

[225] K.Adel and Y.Yao. *Phys. Rev. D*, 49:4945, 1994.

[226] K.Chetyrkin, M.Misiak, and M.Munz. *Phys. Lett. B*, 400:206, 1997.

[227] G.Belanger, F.Boudjema, A.Pukhov, and A.Semenov. *Comput. Phys. Commun.*, 149:103, 2002.

[228] C.Degrassi, P.Gambino, and G.Giudice. *JHEP*, 0012:009, 2000.

[229] P.Gambino and M.Misiak. *Nucl. Phys. B*, 611:338, 2001.

[230] G.Buchalla and A.Buras. *Nucl. Phys. B*, 400:225, 1993.

[231] [CDF Collaboration]. *Phys. Rev.Lett.*, 100:201801, 2008.

[232] T.Kuhr [CDF Collaboration]. "Updated Search for $B_S^0 \rightarrow \mu^+\mu^-$ at CDF". *arXiv:hep-ex/1111.2428.*

[233] [CDF Collaboration]. *http://www-cdf.fnal.gov/physics/projections/.*

[234] P.Ball et al. "B Decays at the LHC". *arXiv:hep-ph/0003238.*

[235] K.Babu and C.Kolda. *Phys. Rev. Lett.*, 84:228, 2000.

[236] J.Ellis, K.Olive, and V.Spanos. *Phys. Lett. B*, 624:47, 2005.

[237] [ATLAS Collaboration]. *http://atlasinfo.cern.ch/Atlas/GROUPS/PHYSICS/TDR/access.html*.

[238] [CMS Collaboration]. *http://cmsdoc.cern.ch/cms/cpt/tdr/*.

[239] V.Buscher and K.Jakobs. *Int. J. Mod. Phys. A*, 20:2523, 2005.

[240] M.Schumacher. *Czech. J. Phys.*, 54:103, 2004.

[241] S.Abdullin et al. *Eur. Phys. J. C*, 39:41, 2005.

[242] S.Gennai, S.Heinemeyer, A.Kalinowski, R.Kinnunen, A.Nikitenko S.Lehti, and G.Weiglein. *Eur. Phys. J. C*, 52:383, 2007.

[243] J.Feng, T.Moroi, L.Randall, M.Strassler, and S.Su. *Phys. Rev. Lett.*, 83:1731, 1999.

[244] F.Gianotti et al. *Eur. Phys. J. C*, 39:293, 2005.

[245] J.Ellis, K.Olive, Y.Santoso, and V.Spanos. *Phys. Lett. B*, 565:176, 2003.

[246] U.Chattopadhyay, A.Corsetti, and P.Nath. *Phys. Rev. D*, 68:035005, 2003.

[247] K.Desch, E.Gross, S.Heinemeyer, G.Weiglein, and L.Zivkovic. *JHEP*, 0409:062, 2004.